Statistical Analysis of Global Ocean Wave and Wind Parameters Retrieved with Empirical SAR Algorithms

(Dissertation zur Erlangung des Doktorgrades der Naturwissenschaften im Department Geowissenschaften der Universität Hamburg)

Vorgelegt von:

Guiting Song

aus Shandong, China

Hamburg 2008

Als Dissertation angenommen vom
Department Geowissenschaften der Universität Hamburg
Auf Grund der Gutachten von Prof. Hartmut Graßl
und Dr. Stephan Bakan

Hamburg, den Dezember, 2008
Professor Dr. Jürgen Oßenbrügge
(Leiter des Departments für Geowissenschaften)

STATISTICAL ANALYSIS OF GLOBAL OCEAN WAVE AND WIND PARAMETERS RETRIEVED WITH EMPIRICAL SAR ALGORITHMS

(*Vom Department Geowissenschaften der Universität Hamburg als Dissertation angenommene Arbeit*)

Guiting Song

116 pages with 64 figures and 15 tables

Abstract

A systematic validation and comparison of met-ocean parameters like significant wave height (H_s), wind speed (U_{10}) and mean wave period (T_m) obtained from ERS-2 wave mode imagettes using a new empirical algorithm (CWAVE), in situ and satellite observations, reanalysis and model results is presented for the global ocean.

The H_s and U_{10} values retrieved from SAR imagettes are validated by in situ observations from both the National Oceanic and Atmospheric Administration (NOAA) buoys and the Polarstern research vessel. The root mean square errors (RMSE) for all collocated CWAVE and NOAA buoy H_s and U_{10} are 0.61 m and 2.40 m/s, respectively, while they increase to 1.35 m and 3.19 m/s for validation with Polarstern data. The H_s observations from Polarstern, subjective visual inspections by trained observers, are less accurate than NOAA buoy values. Furthermore, the Polarstern vessel seldom observed during severe storms due to reasons of ship safety.

The CWAVE H_s is also assessed by comparison with satellite observations from the ERS-2 altimeter and for U_{10} from both the Hamburg Ocean Atmosphere Parameters and Fluxes from Satellite (HOAPS) and Scatterometer data sets. The RMSE for all collocated CWAVE and altimeter H_s values is 0.56 m, it is 1.77 m/s for U_{10} from the Scatterometer collocated pairs but rises to 2.87 m/s for HOAPS. CWAVE results retrieved from SAR imagettes show better agreement with H_s from the altimeter and U_{10} from the Scatterometer than for U_{10} from HOAPS because SAR, altimeter and Scatterometer operate on the same ERS-2 satellite leading to less time and also space differences for collocated pairs.

A comprehensive comparison between CWAVE H_s, U_{10}, T_m and ERA 40 reanalysis results was performed for the period September 1, 1998 to November 30, 2000 for the global ocean. The RMSE values between collocated pairs are 0.5 m for H_s, 2.21 m/s for U_{10} and 2.45 s for T_m. The frequency distribution of met-ocean parameters from CWAVE and ERA 40 show an overall agreement for low and medium sea state, however, an underestimation by CWAVE for high sea state.

A new classification of inhomogeneity of SAR imagettes was investigated to better select homogeneous ones and thereby improve the performance of CWAVE. The new classification parameter was applied to about 1 million SAR wave mode imagettes from nearly two years and compared with the parameter characterizing inhomogeneity of the earlier CWAVE algorithm. The new classification parameter stricter and better estimates inhomogeneous imagettes.

Finally, the CWAVE met-ocean parameter results were applied to retrieve a satellite-based wind wave growth relation, to detect a storm missed by ERA 40 and to investigate a Polar Low. The new wind wave growth relation is compared to the famous Toba 3/2 power law and other former studies and shows good agreement with Toba’s law. The study also indicates that a CWAVE modification using more validation data than earlier would be appropriate.

STATISTISCHE ANALYSE DER MIT EMPIRISCHEN SAR-ALGORITHMEN ABGELEITETEN WELLENPARAMETER UND DES WINDES ÜBER DEM GLOBALEN OZEAN

Zusammenfassung

Es wird eine systematische Validierung von signifikanter Wellenhöhe (H_s), Windgeschwindigkeit (U_{10}) und mittlerer Wellenperiode (T_m) für die mit dem empirischen Algorithmus CWAVE ausgewerteten SAR-Bilder des Satelliten ERS-2 im Wellenmodus durch Vergleich mit in-situ-Daten, anderen Satellitendaten, und Reanalysedaten durchgeführt.

Zunächst werden H_s und U_{10} aus den SAR-Bildern mit in-situ Daten von NOAA-Bojen und dem Forschungsschiff Polarstern validiert. Der mittlere quadratische Fehler für alle räumlich und zeitlich annähernd zusammenfallenden Messwerte von H_s und U_{10} erreichen 0,61 m bzw. 2,40 m/s für die Bojenmessungen, während sie auf 1,35 m bzw 3,79 m/s für die Polarsterndaten anwachsen. Die Augenbeobachtungen von Polarstern sind weniger genau als die Bojendaten und aus Gründen der Schiffsicherheit beobachtet Polarstern selten in starken Stürmen.

H_s wird auch mit Daten des ERS-2 Altimeters und U_{10} mit denen des ERS-2 Scatterometers und des HOAPS Datensatzes aus Hamburg bewertet. Der mittlere quadratische Fehler für H_s schrumpft dabei aud 0,56 m, der für U_{10} auf 1,77 m/s für die Scatterometerdaten aber bleibt mit 2,78 m/s hoch für HOAPS. Die verbesserte Übereinstimmung mit den Scatterometerdaten ist auch der Gleichzeitigkeit der Messungen geschuldet.

Ein umfassender Vergleich zwischen H_s, U_{10} und T_m aus CWAVE und der ERA-40 Reanalyse für die Periode vom 1. September 1998 bis 30. November 2000 für den gesamten Ozean liefert 0,50 m für H_s bzw.2,21 m/s für U_{10} und 2,45 s für T_m. Die Häufigkeitsverteilungen aller dieser Parameter zeigen eine gute Übereinstimmung für schwache und mittlere Windsee, aber eine Unterschätzung durch CWAVE bei stürmischer See.

Auch eine neue Klassifizierung der Inhomogenität der SAR-Bilder zur besseren Auswahl homogener Szenen ist eingeführt worden. Die neue Klassifizierung entdeckt die in etwa 1 Million SAR-Szenen steckenden inhomogenen eher.

Schließlich wurden die H_s-, U_{10}- und T_m-Werte aus SAR-Szenen verwendet um eine satelliten-basierte Wind-Wellenbeziehung zu finden, einen Sturm, der in den ERA-40-Daten nicht enthalten war, zu erkennen und das Windfeld eines polaren Tiefdruckgebietes darzustellen. Die neue Wind-Wellen-Beziehung ist nahe zur theoretischen. Die Untersuchungen zeigen aber auch insgesamt, dass noch mehr Validierungsdaten zur Verbesserung des CWAVE-Algorithmus notwendig sind.

Contents

List of Figures

List of Tables

Chapter 1

Introduction

It is well known that the oceans play a central role in the global climate system, thus much research was devoted to oceans in recent decades, including wind and wave retrieval from satellites giving global coverage, indentification of mesoscale features like eddies, and three-dimensional modelling of ocean parameters such as sea surface temperature, salinity and currents. The understanding, modelling and forecast of these parameters has taken a fast development with the help of supercomputers. Both the ERA 40 reanalysis from the European Centre for Medium-Range Weather Forecasts (ECMWF) and the reanalysis from the National Centers for Environmental Prediction (NCEP) are famous data sets for meteorology-ocean (met-ocean) parameters.

The validation and comparison of these numerical model results are also important aspects in ocean research. Many techniques have been developed to measure ocean parameters. First, the ocean parameter observations were estimated by mariners in the beginning stage by visual inspection. Such data were limited to coastal areas or ship routes and were also affected by the experience of the observer. Second, buoys equipped with different sensors either drifting buoys or moored and other platforms often on lighthouses at capes and beaches were collecting ocean parameters. These two observation methods obviously cannot obtain global coverage, however remote sensing from space provides a new possibility to observe all ocean basins frequently. Many different instruments have been installed on earth observation satellites. Among them the synthetic aperture radar (SAR) is the only instrument which up to now can provide high-resolution, two dimensional sea surface information on a global scale under all weather conditions.

Compared to other instruments like optical instruments including lasers or thermal infrared radiometers and passive microwave radiometry, the SAR instruments have three advantages. First is high horizontal resolution. Already the first spaceborne SAR aboard the SEASAT satellite, which was launched in 1978, provided a ground resolution of up to 25 m, similar to the current SAR systems with images of about 100 km × 100 km size, such as the European satellites ERS-2 and ENVISAT as well as the Canadian RadarSATs. The German TerraSAR which was launched on June 15, 2007 can even provide up to 1 m resolution images. Second, the SARs as active operate day and night, in contrast to optical or short-wave infrared sector that rely on sunlight reflection. Third, the SAR microwave signals can penetrate clouds.

The SAR images are a rich source of information both marine research and operational oceanography. The information content of SAR images is in general quite different from what solar and infrared radiation techniques reveal. The SAR technique opened up unexpected avenues of research into dynamical phenomena such as internal waves, surface slicks and of course ocean waves and hence near surface winds.

There are three kinds of SAR image modes in general on ERS-2 and ENVISAT: wave mode, image mode and scan mode. In this study, the wave mode image with small size (5 km × 10 km) socalled imagettes is used to retrieve met-ocean parameter like significant wave height (H_s), wind speed (U_{10}) and mean wave period (T_m) using a new empirical algorithm (CWAVE) which has been developed by Schulz-Stellenfleth et al. (2007). More than a decade of wave mode image acquisition over the open ocean, beginning with the European satellite ERS-1 and continuted by ERS-2, ENVISAT and TerraSAR, provide a new opportunity to study ocean climatology. In this study, more than two years of data with about 1 million ERS-2 wave mode images from September 1, 1998 to November 30, 2000 are analysed using the CWAVE algorithm. CWAVE offers a big advantage over the traditional SAR wave retrieval methods as it does not require additional information to resolve the directional ambiguity of wave propagation. Several inversion schemes (Krogstad et al., 1994; Hasselmann et al., 1996; Mastenbroek and de Valk, 2000) need a priori information from wave models or other sensors to retrieve wave height.

However, the CWAVE algorithm is to fit a quadratic model which relates a number of key parameters of SAR image like the normalized radar cross section (NRCS), the image variance and 20 parameters computed from the SAR image variance spectrum using a set of orthonormal functions. The main feature of CWAVE is that no explicit estimation of the two-dimensional ocean wave spectrum is needed as an intermediate step as in all other methods.

The scope of this work is:

- Two traditional wind retrieval algorithms from SAR image are compared for the high sea state and a new algorithm retrieved from ENVISAT dual polarization SAR image was developed.

- A statistical validation and comparison of met-ocean parameters like significant wave height (H_s), wind speed (U_{10}) and mean wave period (T_m) between CWAVE retrievals from SAR wave mode image and other data sets such as

— NOAA buoy in situ observations
— Polarstern in situ observations
— Altimeter
— ERA-40 reanalysis
— Scatterometers
— HOAPS

- SAR retrievals applications are investigated in the following aspect

— Retrieval of a satellite-based wind wave growth relation
— Storm missed by ERA 40 data
— Polar Low detection with the help of AVHRR image

Two year with CWAVE retrievals are available for the statistical evaluation, validation and comparison, which have not been attempted so far. The first major outcome of this study will be the validation and comparison of different existing products of met-ocean parameters for the period September 1, 1998 to November 30 2000 on a global ocean basis. The statistical analysis between CWAVE retrievals and other available data sets will be given as scatterplot comparisons, including statistical parameters such as bias, root mean square (RMS) error, correlation coefficient and scatter index, frequency distribution analysis and standard deviation error analysis (see Chapter 4).

Another attemp is the development of an algorithm to retrieve the wind field from dual polarization SAR images. Traditionally, a priori information, especially the wind direction coming from model results or buoy observations, is needed to eliminate the 180° ambiguity of the wind direction. In this study, the wind speed and wind direction will be directly retrieved from the dual polarization SAR image alone because the co-polarization and cross polarization SAR images contain different information about the sea surface, thus providing such a new possibility to obtain both the wind direction and wind speed from a dual polarization SAR image (see Chapter 3).

Finally, two applications of CWAVE retrievals will be presented: A new wind wave growth relation based on H_s, U_{10} and T_m retrievals from CWAVE will be developed by least square regression analysis. This is also an attempt to compare with traditional wind wave growth studies that were based on experiments, theoretical analysis or only regional observations. The other application is the detection of a storm missed by ERA 40 data and of a Polar Low verified with the help of AVHRR image. The CWAVE retrievals provide a new possibility to detect polar low by setting a standard threshold of wind speed and significant wave height and the variation of wind direction of different imagettes along the satellite track if the satellite orbit passes through the polar low (see Chapter 5).

The thesis is structured as follows: The different met-ocean parmater data sets are introduced in Chapter 2. First the ERS-2 satellite and its SAR data are described. The second part of this chapter is devoted to a new inhomogeneity classification method. Thirdly the in-situ observations from NOAA buoys and the Polarstern research vessel are presented. Four data sets from other satellite instruments used for comparisons are also portrayed briefly. Finally the reanalysis model data set ERA-40 is presented.

In Chapter 3 two wind field models are compared in a case study for high sea state in the first part. Then, a new algorithm for retrieving the wind field from a dual polarization ENVISAT ASAR image is developed. In Chapter 4 the CWAVE retrievals are validated by in-situ observations and are also statistically compared to other satellite data sets and ERA 40 model results. In Chapter 5 three applications of CWAVE retrievals are given including the development of a new wind wave growth relation, the detection of a storm missed by ERA 40 and of a polar low. Finally in Chapter 6 together with a summary and conclusions, an outlook to some future tasks in this area of research is presented.

Chapter 2

Data Sets

2.1 Introduction

This chapter introduces several data sets for significant wave height (H_s), near surface wind speed over the ocean (U_{10}) and wave period (T). Firstly, the mentioned parameters H_s, U_{10} and mean wave period (T_m) are retrieved with a new empirical algorithm (CWAVE) which has been developed by Schulz-Stellenfleth et al. (2007) using SAR wave mode images from the ERS-2 sensor. Secondly, in situ sea surface parameters observed from buoys and a research vessel are used to validate retrievals using SAR image. The National Data Buoy Center (NDBC) offers recent and historical observations such as wind speed, and wave directional spectral information collected by the National Oceanic and Atmospheric Administration (NOAA). The German Ice-breaker Polarstern (a research and supply vessel) also does provide wave height and wind speed information along the ship track as another in situ data source. Thirdly, satellite data from scatterometer, altimeters, and passive microwave sensors (Hamburg Ocean Atmosphere and Fluxes from Satellite (HOAPS)) are used to compare with SAR retrievals. Finally, ERA-40 model reanalysis data are also compared to CWAVE results in this study.

Significant wave height (H_s) is obtained from the following sources for our statistical analysis:

- empirical SAR algorithm (CWAVE)
- NOAA buoy in situ observations
- Polarstern in situ observations
- Altimeter
- ERA-40 reanalysis

Wind speed (U_{10}) is usually measured at a height of 10 m or, if measured at another height, is usually converted to 10 m, especially in this wind speed comparison study. The following sources of wind speed are used:

- CWAVE
- NOAA buoy in situ observations
- Polarstern in situ observations
- Scatterometers
- HOAPS
- ERA-40 reanalysis

The wave period is only compared between CWAVE and ERA-40.

Table 2.1: Description of the different marine parameter data sets: The spatial and temporal resolutions and the periods for which the data were available are listed

Data Type	Spatial Resolution	Temporal Resolution	Availability
CWAVE	200 km along subsatellite track	inst.	Sep. 1998-Nov. 2000
NOAA Buoy	Point measurement	1h	1976-present
Polarstern Vessel	Point measurement	3h	1994-present
Altimeter	600 m to 6 km	inst.	1986-present
Scatterometer	50 km	inst.	Mar. 1996-Jan. 2001
HOAPS	0.25º	12h	1987-2005
ERA-40	2.5º	6h	1957-2002

The marine parameters contained in the different products vary strongly in spatial and temporal resolution as listed in Table 2.1. The European Remote Sensing Satellite ERS-2 acquires one wave mode image every 200 km (30 seconds) along orbit nearly instantaneously, so the spatial resolution of CWAVE is given as 200 km, the results are retrieved from images which cover only 10 km×5 km.This is a bit similar to Polarstern measurements because the crew on Polarstern usually observes once every hour along the vessel’s track. However, the NOAA buoy results are point measurements every hour. So the colocation numbers between CWAVE results and in-situ observation are small due to the spatial and temporal gaps. In order to make a rather comprehensive comparison and validation, other datasets which have much more collocation points with CWAVE results like from altimeter and scatterometer were also used in this study. These three instruments are installed on the same satellite ERS-2, so the temporal gap between them is almost zero. All three instruments measure backscattered microwave radiation almost instantaneously. An overview of satellites carrying these instruments as well as of some experimental missions flown on the Space Shuttle can be found in Henderson and Lewis (1998). More detail will be given later. Furthermore, HOAPS data which can provide many sea surface and atmospheric parameters were used in this study to statistically compare the wind speed results with CWAVE. As only ERA-40 allows to find a collocation pair for each CWAVE results, it was used in this study to make a complete statistical comparison to SAR retrievals.

The different data sets will be described in detail hereafter.

2.2 ERS-2 Satellite and its SAR Data

Firstly, a short overview of the ERS-2 mission is given followed by an introduction to the active ERS-2 instruments in the microwave range. Secondly the main emphasis is on SAR wave mode data.

The European remote sensing satellites ERS-1 and ERS-2 were launched in July 1991 and April 1995 respectively. ERS-1 finished data acquisition in March 2000 due to a failure in the on-board attitude control system. Both satellites are flying in a sun-synchronous polar orbit with an inclination of 98.5° at 785 km height. Due to the inclination, data can be acquired up to 82° N/S latitude. On board of both satellites is a set of active microwave sensors and additional complementary instruments which include the SAR imaging system, a wind scatterometer, and a radar altimeter (RA), as well as the along-track scanning radiometer (ATSR-2). The characteristics of ERS-1/2 are summarised in Table 2.2.

Table 2.2: Parameters for the ERS-1 and ERS-2 satellites.

	ERS-1	ERS-2
Launch	1991	1995
Orbit height	785 km	785 km
Antenna size	10 m×1 m	10 m×1 m
Band	C	C
Frequency	5.3 GHz	5.3 GHz
Bandwidth	15.55±0.01MHz	15.55±0.01MHz
Pulse Repetition Frequency	1640-1720 Hz	1640-1720 Hz
Polarization	VV	VV
Distance to the sub-satellite track	275 km	341 km
Platform velocity	7455 m/s	7455 m/s
Ratio of slant range to platform velocity	112 s	112 s
Orbit period	~100 min	~100 min
Orbit per day	14.3	14.3
Look direction	Right-looking	Right-looking
Foot print size in range	100 km	100 km
Geometric ground resolution of SAR	30 m×30 m	30 m×30 m

The ERS programme has been designed to serve a large variety of users with a comprehensive range of products and services. The prime use of ERS data in this study of marine parameters is statistical analysis. Data has been evaluated for the first time on a routine basis over the global oceans by the Marine Remote Sensing group at German Aerospace Center (DLR) in Oberpfaffenhofen.

In this work data of the active microwave instrument (AMI) as well as the radar altimeter (RA) were used. Features of both intruments are described briefly below. A global set of high-resolution, single-look complex (SLC) imagettes was processed from ERS-2 SAR wave mode raw data at the DLR and used as input for the algorithm CWAVE which retrieves the mentioned three marine parameters.

Table 2.3: Technical parameters for the ERS-2 SAR image and wave mode.

Pixel size in azimuth (wave mode)	4 m
pixel size in slant range (wave mode)	8 m
pixel size (image mode)	30 m
image size (image mode)	100 km × 100 km
imagette size (wave mode)	10 km × 5 km
Distance between 2 imagettes	200 km (30 s)
Daily coverage	~ 1100 imagettes
incidence angle (centre of imagette)	23.5 °
Digitization	4-bit ADC

Besides imaging, active microwave sensors like scatterometers and radar altimeters also allow the measurement of wind and wave characteristics. Scatterometers measure the backscattered energy (specific cross section) at different incidence angles. Wind direction and wind speed are retrieved by adapted algorithms on a coarse grid. Vertically-downward-looking (nadir) radar altimeters obtain information on the sea surface from the travel time, intensity and shape of the return pulse of very short emitted short pulses, reflected through specular reflection at the sea surface. From altimeters wind speed and significant wave height can be retrieved in medium resolution along track (600 m to 6 km) and lower resolution across track. Significant wave height from altimeters and wind speed from scatterometers are used in this study for comparison with CWAVE results.

Next, SAR data, especially wave mode SAR data are introduced. The ERS-2 satellite carries an active microwave instrument (AMI) operating in C-band (5.3 GHz, with a wavelength of 5.656 cm). SAR image data (amplitude and phase of the backscattered signal) are available from this instrument at different coverage and resolution. Two SAR data modes are used in this study: the image mode and the wave mode. Image mode data have to be downloaded to the receiving station at the ground during the satellite overflight, since the large amount of raw data can not be stored on board. So the image mode data only can be acquired for a maximum of 12 minutes per orbit. In contrast to image mode, the wave mode of an imagette consists 5 km×10 km scale for which raw data every 200 km along the satellite track can be stored on global ocean. The data are stored on-board temporarily, and then downloaded when the satellite approaches a receiving station. The geometry of the ERS-2 wave mode image is illustrated in Figure 2.1.

It is important to note that the wave mode data provided as a standard product by the European Space Agency (ESA) are only coarsely gridded image power spectra and can not be used immediately as an input for CWAVE. They must be reprocessed by the SAR processor BSAR developed at DLR/DFD to complex SAR image data. These are usually called imagettes because of their small size. Such imagettes are the main data used in this study to retrieve met-ocean parameters. The general information about such wave mode imagette as well as image mode SAR data was summarized in Table 2.3.

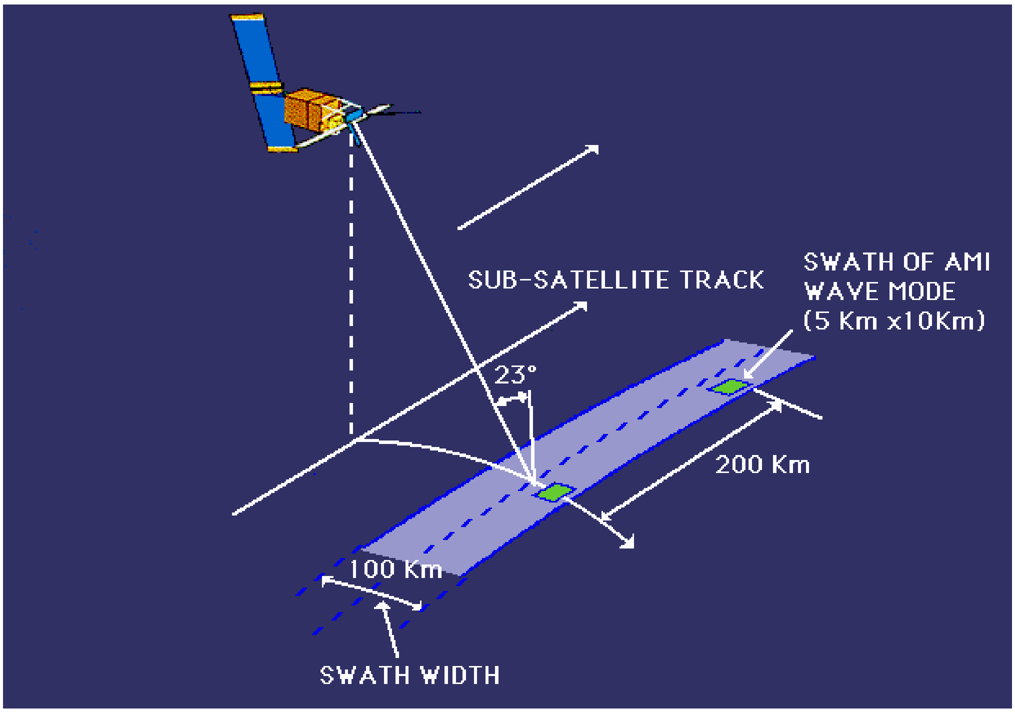

Figure 2.1:Geometry of the ERS-2 wave mode image

About 1 million imagettes are available now at DLR, covering the globlal ocean from 1 September 1998 to 30 November 2000, thus allowing the global statistical analysis of the met-ocean parameters retrieved by the CWAVE algorithm for the first time. Met-ocean parameters were directly retrieved from SAR image without a priori information (Lehner et al., 2000; Schulz-Stellenfleth et al., 2007).

2.3 Investigation of Inhomogeneity in ERS-2 Wave Mode Images

It has been demonstrated that SAR imagettes (a wave mode image hereafter is called imagette) can be used to derive the following sea wave parameters: significant wave height H_s, wind speed U_{10} and mean wave period T_m (Schulz-Stellenfleth et al., 2007). An empirical approach (CWAVE) was developed in the German Aerospace Centre (DLR) to retrieve the mentioned ocean wave parameters from SAR. The imagette is the only input for CWAVE. Because strong inhomogeneity within a single imagette leads to large errors in CWAVE retrievals, many studies have analyzed this feature of SAR images (Schulz-Stellenfleth et al., 2004; Alpers W. et al., 1994; Hasselmann et al., 1985; Horstmann et al., 2003). Several factors such as sea ice, rain or biogenic surface films, oil slicks, or ship wakes can make an imagette inhomogeneous, such inhomogeneous imagettes should not be applied to retrieve wave parameters. A homogeneity test has been used by Schulz-Stellenfleth et al. (2007) based on the standard spectral estimation theory. Every imagette has been divided into 32 subimagettes of about 1×1 km size, which were used to estimate the mean and the variance of the periodograms. The expectation value of the homogeneity parameter θ is defined as

$$\theta = \frac{\sum_k \frac{\overline{\mathrm{var}}(P_k)}{\overline{mean}(P_k)}}{\sum_k \overline{mean}(P_k)} \tag{2.1}$$

Where $\overline{mean}$ and $\overline{\mathrm{var}}$ are standard estimators for the mean and variances. P_k is the k-th subimage's periodogram. For a perfectly homogeneous imagette, the homogeneity parameter θ should be 1. In most cases, this procedure is allowed to classify the imagettes into homogenous and inhomogeneous ones, but some cases have been incorrectly classified even over the open ocean. Thus a new classification scheme parameter has been developed here to better detect homogeneous imagettes.

2.3.1 New Inhomogeneity Classification

1535 test imagettes classified by eye including four types of imagette inhomogeneity: water, slick, sea ice and undefined inhomogeneous imagettes, were applied to develop new classification parameters, illustrated in Fig. 2.2. The newly-developed parameters are validated by nearly 1 million ERS-2 wave mode imagettes from September 1998 to November 2000.

In order to analyse the inhomogeneity of the imagettes they need to be divided into subimagettes first. The scheme for the sub-division of imagettes is as follows: In every wave mode imagette, there are 512 pixels in the range direction with 20 m horizontal resolution and 1024 pixels in the azimuth direction with a resolution of 4 m. In this scheme, 5 pixels are selected in the range direction and 25 in the azimuth direction in every subimagette. Thus the size of a subimagette is about 100 m ×100 m, leading to 4080 subimagettes in one full imagette.

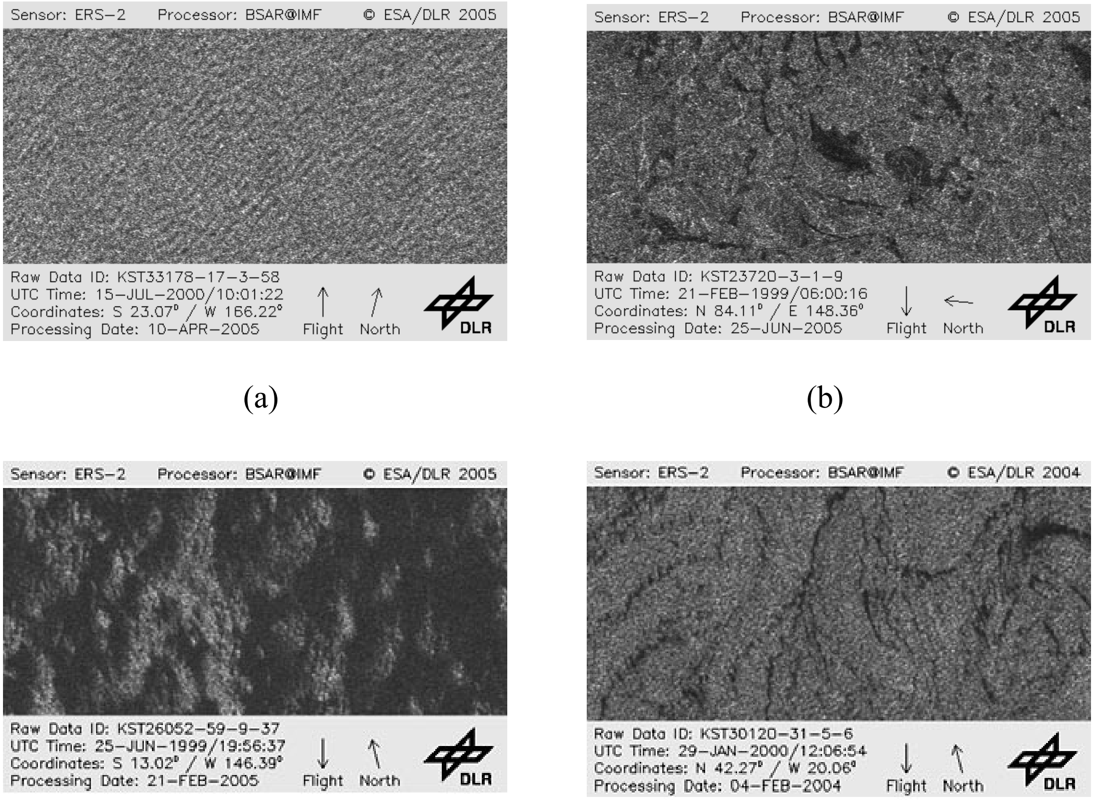

(a) (b)

(c) (d)

Figure 2.2: Four types of ERS-2 SAR imagettes: (a) water (b) ice (c) undefined (d) slick

Several new classification parameters were investigated in this study. Their definitions are as follows:

1. Inhomo: the definition is presented in Eq. 2.1
2. CoVar: the variance of the intensity of every subimagette divided by the mean value of intensity
3. Min: The Minimum normalized radar cross section (NRCS) of subimagette compared to the mean NRCS of the whole imagette
4. Max: The Maximum NRCS of subimagette compared to the mean NRCS of the whole imagette
5. PC (Percentile): Fig. 2.3 shows a sketch of the definition of this inhomogeneity measure PC. The calculation process for PC is presented in Eqs. 2.2-2.5. Firstly,

the standard deviation δ is calculated from the intensity of every imagette's pixel following Eq. 2.2. Eq. 2.3 shows the mean intensity of the whole imagette ($\bar{I}$). η is the mean plus two standard deviations, n is the number of pixel with an intensity higher than η. N is the whole pixel number of the imagette. So the definition of PC is the percentage of pixel for which the intensity is larger than η.

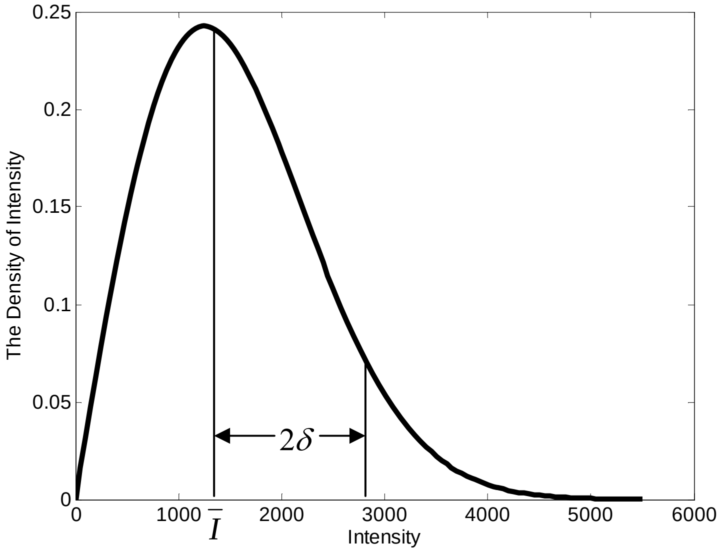

Figure 2.3: Sketch for the definition of the Percentile inhomogeneity measure.

$$\delta = std(I) \tag{2.2}$$

$$\bar{I} = < I > \tag{2.3}$$

$$\eta = \bar{I} + 2\delta \tag{2.4}$$

$$n = where(I > \eta) \tag{2.5}$$

$$PC = \frac{n}{N} * 100\% \tag{2.6}$$

2.3.2 Different Inhomogeneity Thresholds

Fig. 2.4 shows the results when the 1535 test imagettes were applied to different definitions of the inhomogeneity parameter. It can be seen that Min performs best because it clearly separates water imagettes from inhomogeneous imagettes. After linear fitting, the separation function: $y = -1.376x - 24.9$ can be obtained with y as the minimum NRCS of subimagettes and x as the mean NRCS of the whole imagette. This separation function has been applied to all imagettes of the entire period to separate the homogeneous imagettes from inhomogeneous ones.

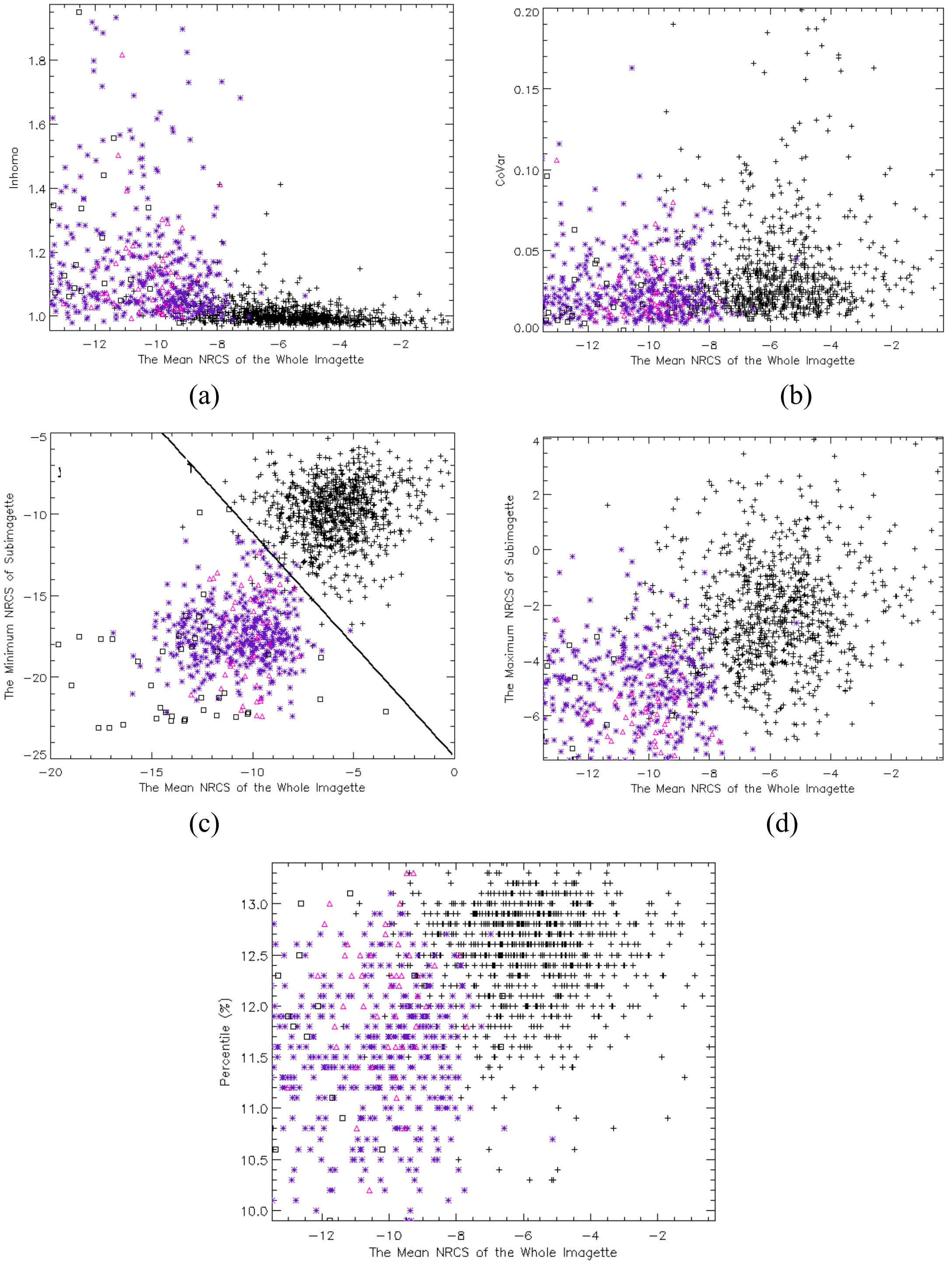

(a) (b)

(c) (d)

(e)

Figure 2.4: Test of different inhomogeneity parameters. (a) Inhomo, (b) CoVar, (c) Min, (d) Max, (e) PC. The symbol definition is as follows: + water, * ice, △ slick, and □ is undefined inhomogeneity.

2.3.3 Discussion

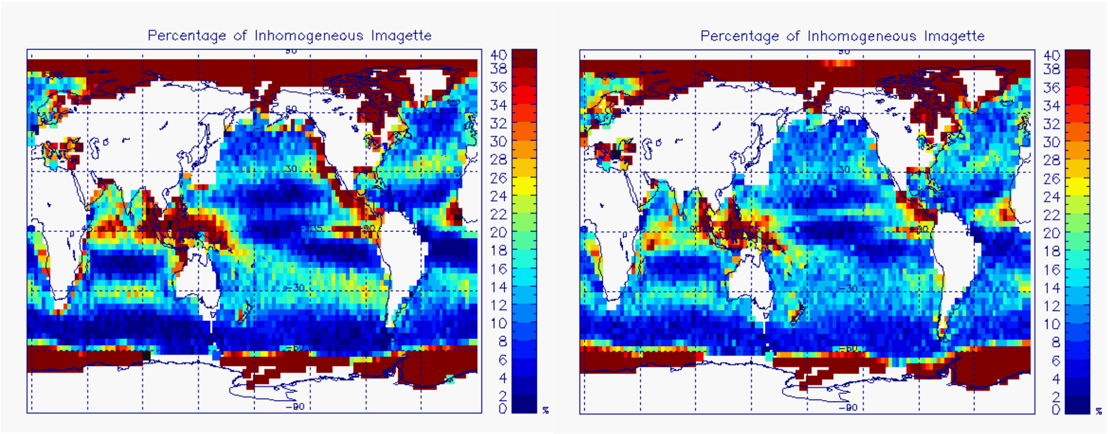

(a) (b)

Figure 2.5: The global distribution of the percentage of inhomogeneous imagettes within 3° × 3° longitude/latitude boxes, (a) new classification parameter, (b) Inhomo parameter

The new classification parameter was applied to about 1 million SAR wave mode imagettes from two years. All of the imagettes are located in the ocean area. 3° ×3° longitude/latitude boxes over the ocean are selected to investigate the global distribution of the inhomogeneous imagettes. The inhomogeneous imagettes' global distributions of both the new classification scheme and Inhomo are shown in Fig. 2.5. The largest inhomogeneous area except for the polar ice area is close to the equator in the West Pacific Ocean (90°E-150°E, 20°S-20°N), the west of Central America (135°W-90°W, 0°-30°N), the Southern Indian Ocean (46°E-80°E, 3°S-10°N) and close to the West African coast (20°W-10°W, 3°N-15°N). The main reason of the strong inhomogeneity proportion in these areas is most probably low wind speed, as can be seen from Fig. 2.6. The high percentage of low wind speeds in the HOAPS data set corresponds clearly to the strong inhomogeneity proportion of Fig. 2.5, except the polar regions.

If the percentage of inhomogeneous imagettes in Fig. 2.5 is larger than 40%, it is set to be 40%. Fig. 2.7 displays the percentage of inhomogeneous imagettes larger than or equal to 40%. The percentage of inhomogeneous imagettes for the new classification parameter shows to be much higher in the Arctic area than for Inhomo. This points to the new classification being more rigorous. For a further investigation, SSM/I sea ice concentration data in the Arctic area are used. Fig. 2.8 shows the percentage of inhomogeneous imagettes in the north polar region for the new classification parameter and Inhomo together with the mean SSM/I concentration. It can be seen that the results of the new classification parameter fit better with the SSM/I concentration data than for Inhomo. The high mean SSM/I sea ice concentration corresponds well to the high inhomogeneous imagette proportion.

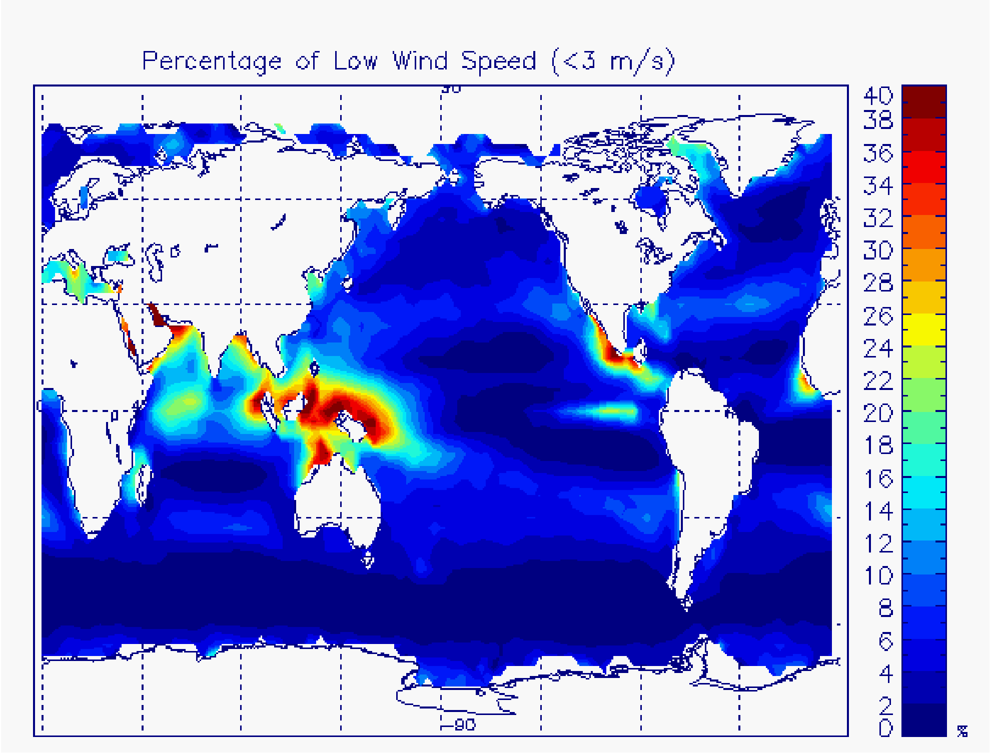

Figure 2.6: The global distribution of low wind speed (U_{10}<3 m/s) within 3° × 3° longitude/latitude boxes from HOAPS.

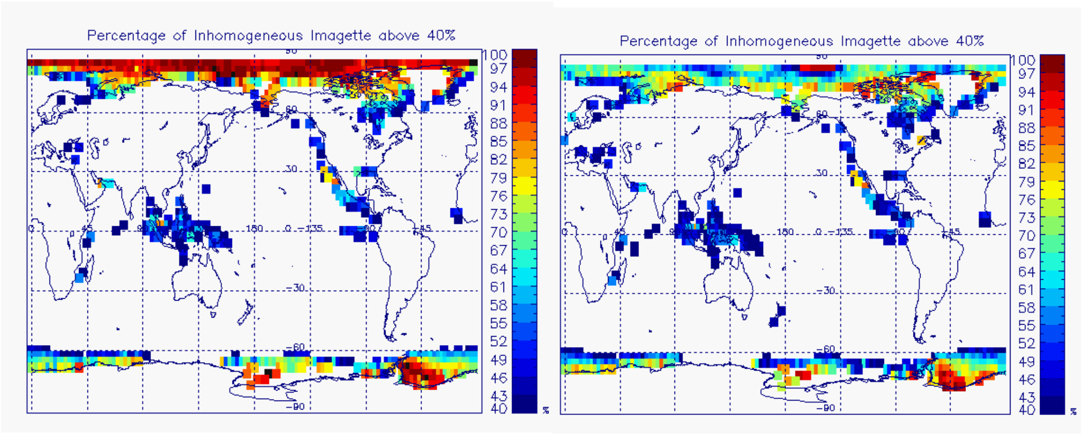

(a) (b)

Figure 2.7: The global distribution of inhomogeneous imagettes within 3° × 3° longitude/latitude boxes; (a) new classification parameter, (b) Inhomo parameter.

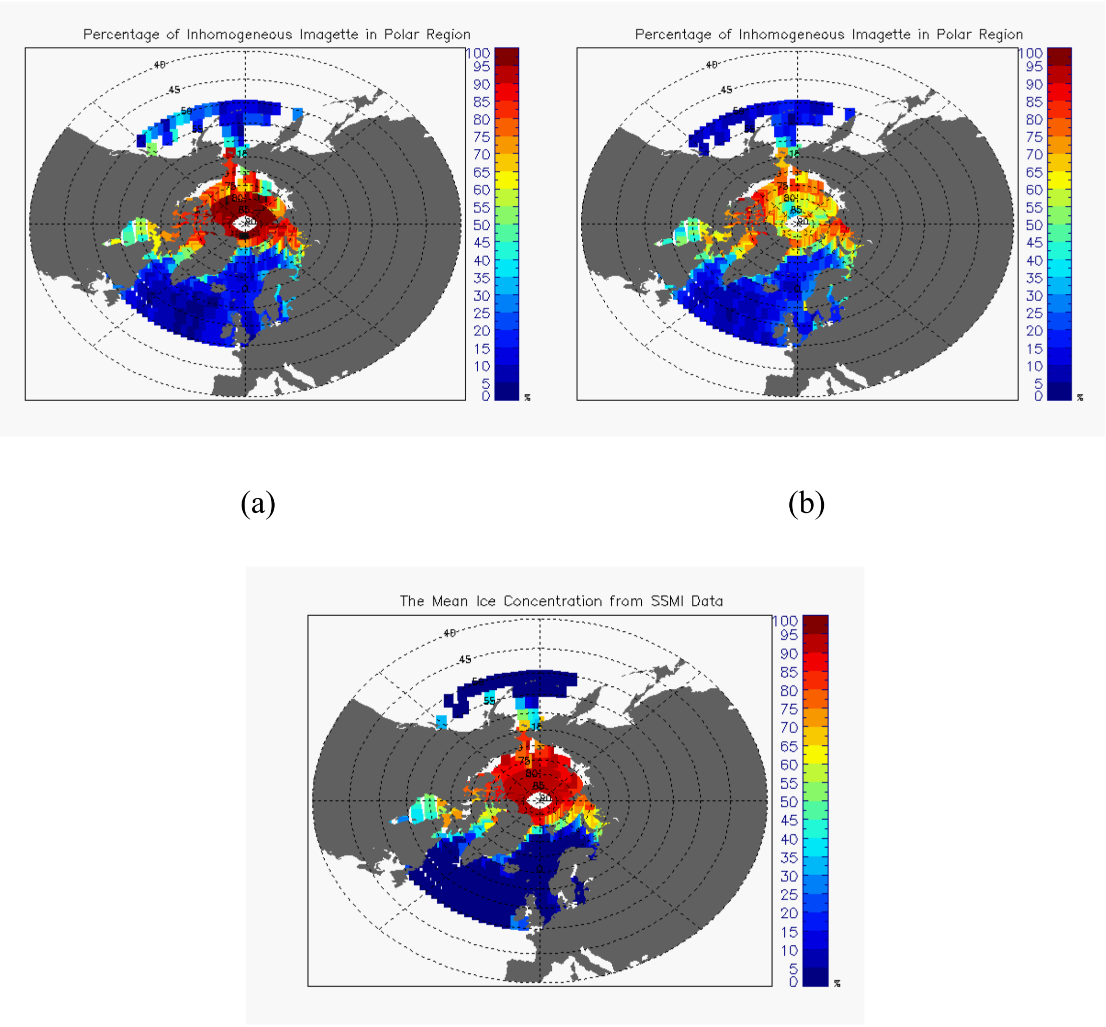

(a) (b)

(c)

Figure 2.8: Percentage of inhomogeneous imagettes in the north polar region for (a) new classification parameter, (b) Inhomo parameter (c) SSM/I sea ice concentration from National Snow and Ice Data Center (http://nsidc.org/).

2.4 In Situ Observations

The in situ observations used in this study include NOAA buoy data and ship-borne data from Polarstern. They can be regarded as a close approximation to the "*truth*", although the observations by them also contain systematic and other kinds of errors. These two kinds of data will be introduced in this section.

2.4.1 NOAA Buoy Data

Buoy data from the National Oceanic and Atmospheric Administration (NOAA) can be obtained from the website: http://www.ndbc.noaa.gov. Here all available buoy reports were collected for the period from 1 September 1998 to 30 November 2000. Over the period of this study, NOAA operated about 75 moored buoys and 60 C-Man stations, which have been installed on lighthouses, at capes and beaches, on near shore islands, and on offshore platforms, located in the Northeast Pacific, the Gulf of Mexico, the North West Atlantic, near Hawaii, and the Equatorial Pacific. Of these sites, we selected 96 stations whose water-depths are larger than 100 m. The locations and water depth of each buoy are depicted in Figure 2.9.

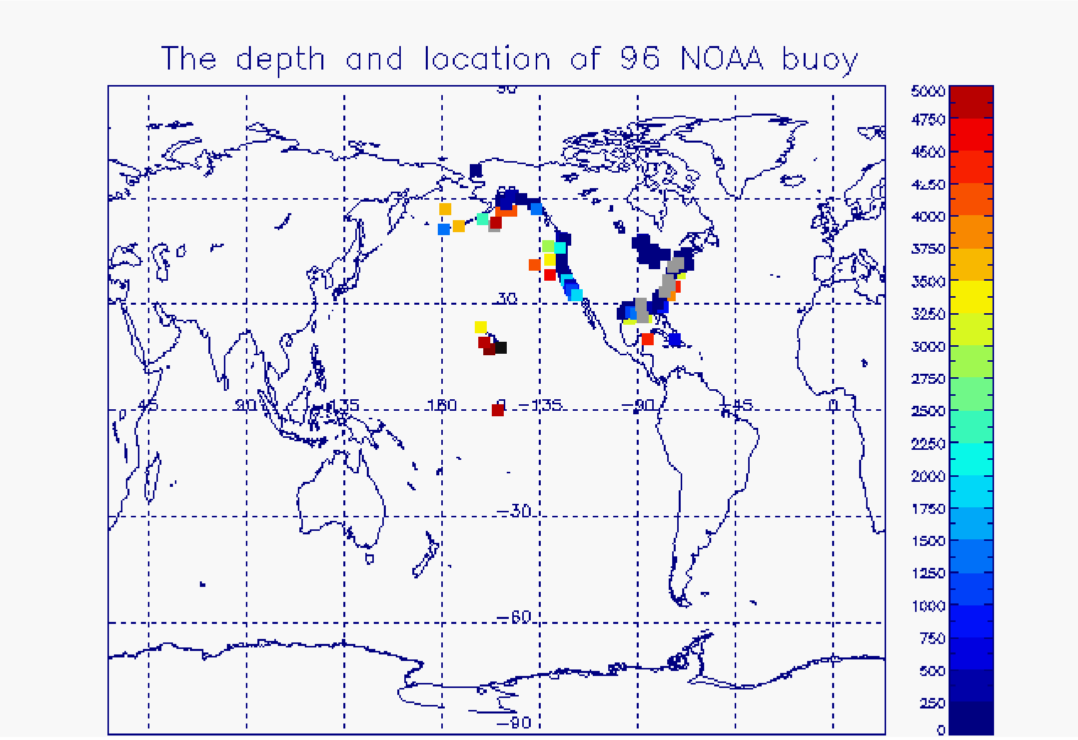

Figure 2.9: Location and water depth of NOAA buoys used in this study.

NDBC-reported wave measurements are not directly measured by sensors on board the buoys. Instead, the accelerometers or inclinometers on board the buoys measure the heave acceleration or the vertical displacement of the buoy hull during the wave acquisition time. A Fast Fourier Transform (FFT) is applied to the data by the processor on board the buoy to transform the data from the temporal domain into the frequency domain. Note that the raw acceleration or displacement measurements are not transmitted shore-side. Response amplitude operator (RAO) processing is then performed on the transformed data to account for both hull and electronic noise. It is from this transformation that non-directional spectral wave measurements (i.e., wave energies with their associated frequencies) are derived. Along with the spectral energies, measurements such as significant wave height, average wave period, and dominant period are also derived from the transformation.

The NOAA uses a variety of buoy types with anemometers mounted either 5 m or 10 m above the ocean surface. Wind speed and direction are measured for a period of 8 minutes each hour and a scalar average of wind speed and direction is reported. The stated accuracy of wind speed is ±1 m/s with a resolution of 0.1 m/s and the stated accuracy of the wind direction is ±10 degrees with a resolution of 1.0 degree (Gilhousen, 1987). A few C-Man land based stations have also been included in our "buoy" data set, provided they were mounted on very small islands or reefs. These stations measure wind speed at a variety of heights depending on the nature of the station, and only average the data for 2 minutes each hour.

2.4.2 Research Vessel Polarstern Data

The German research icebreaker Polarstern was commissioned on the 9th December 1982. Polarstern was built by the Howaldtswerke-Deutsche Werft at Kiel and the Nobiskrug at Rendsburg. The ship has a length of 118 metres (387 feet). Polarstern is a double-hulled icebreaker. It is operational at temperatures as low as -50°C. Polarstern can break through ice 1.5 metres thick at a speed of 5 knots. Thicker ice also can be broken by ramming. More detailed parameters are listed in Table 2.4. Polarstern is mainly used to support the German Antarctic station which result in regular cruise between Europe and the Antarctic, cutting through a very different ocean conditions.

Table 2.4: General information of Polarstern Research Icebreaker

Displacement	17,300 t
Region	Arctic and Antarctica
Length	117.91 m
Beam	25.07m
Draught	11.21m
Speed	15.5 kn (28.7 km/h)
Propulsion	4 engines, 14,000 kw
Complement	44 at most
Home Port	Bremerhaven, Germany

Wind, wave height and other met-ocean parameters are extracted from the website: http://www.awi.de/en/infrastructure/ships/polarstern/meteorological_observatory/synoptic_observations/. Only data since 1994 are available from this website. For this study The vessel data set used in this study only covered the period September 1998 to November 2000 The wind speed measurements are 10-minute averages at the given time in UTC every three hours along the vessel track. However, wave height observations are visual results by weather observer in the vessel, so there are no observations during night. All these synoptic data are generally coded according the definitions of the Word Meteorological Organization WMO (FM12/13).

According to communicating with Gert König-Langlo, Cup anemometer (SK 565, Thies, Germany) and wind vanes (SK 566, Thies, Germany) at a height of 39 m above the waterline are used to measure the relative wind direction and wind speed. The true wind was calculated from the relative wind data using the ship speed measured relative to the water (ATLAS, DOLOG 22). From October 15, 1998, GPS came into use, and the true wind is calculated with respect to the ships movement over ground. Since October 2007, sonic-anemometers are in use.

2.5 Satellite Data

Met-ocean parameters from three kinds of satellite data sets are used in this study: wind speed (U_{10}) from ERS-2 Scatterometer, significant wave height (H_s) from Radar Altimeter (RA) and wind speed (U_{10}) from the Hamburg Ocean Atmosphere Parameters and Fluxes from Satellite (HOAPS). HOAPS's wind speed is based on measurements with several Special Sensor Microwave/Imagers (SSM/I). Furthermore, all of these three data sets retrieve the met-ocean parameters by measuring the sea surface roughness, either directly (Scatterometer and RA) or indirectly (HOAPS), so the basic principles and methodologies behind these conversions are descibed in the next section.

Generally, H_s and U_{10} from satellite are transformations of electromagnetic radiation signals detected by sensors onboard a satellite. The electromagnetic radiation received at the antenna has three principal sources: black body radiation emitted from the earth surface, reflected solar radiation and energy pulses emitted by satellite radars. Planck's equation gives the spectral radiance L_v emitted by a black body as following

$$L_v(v,T) = \frac{2hv^3}{c^2} \times \frac{1}{\exp(hv/k_B T) - 1} \tag{2.7}$$

Where v is frequency, T is the absolute temperature, c is the speed of light, h and k_B are the Planck and Boltzmann constants, respectively. Three important quantities can be derived from Planck's equation.

First, the total emitted radiance increase with T^4, known as Stefan-Boltzmann Law.

Second, by setting the first derivation of Planck's equation to zero, Wien's displacement law can be derived. Thus, $\lambda_{\max}$ and $v_{\max}$, the wavelength and frequency of maximum radiance can be determined for any black body with the following value,

$$\lambda_{\max} = 2879[\mu m\ K]/T \tag{2.8}$$

$$v_{\max} = 5.87 \times 10^{10}[HzK^{-1}]T \tag{2.9}$$

Thus, the maximum black body radiance of the earth with $T = 300K$ is therefore emitted at wavelengths around 10 μm which is in the thermal infrared.

Third, for long wavelengths λ satisfying the inequality $hc/\lambda K_B T \langle\langle 1$, which is the case for microwaves emitted from the earth, the spectral radiance L_v is a linear function of temperature and Rayleigh-Jeans approximation holds:

$$L_v = \frac{2v^2 k_B}{c^2} \bullet T \tag{2.10}$$

The Rayleigh-Jeans approximation enables the radiative transfer equation to be written in form of brightness temperatures instead of radiances.

Remote sensing is conducted in certain bands in the visible (VIS), infrared (IR), and microwave (MW) wavelength range due to reflection and absorption within the atmosphere. The satellite data used in this study is only obtained within the microwave bands, where microwaves occupy the part of the electromagnetic spectrum between 1-90 GHz in frequency, or approximately 200 μm up to a few mm in wavelength.

The microwave instruments installed on satellites have two main advantages. First, microwave remote sensing is independent of sun light, therefore measurements are made day and night. Second, microwave radiation emitted by the instruments or from the surface penetrates clouds. This permits sea surface roughness to be evaluated under all weather conditions.

Microwave instruments are classified as active and passive instruments. Passive instruments, such as the Special Sensor Microwave/Imager (SSM/I), observe either reflected solar radiation or the naturally emitted blackbody radiation. In contrast, radars are active measurement system that transmit pulses of energy towards the ocean surface, and then receive the backscatter, thus providing its own illumination.

Active microwave instruments include imaging synthetic aperture radars (SAR), directed, pulsed vertical beams (altimeter), several pulsed fan beams or rotating pulsed beam (scatterometer). Both altimeter and scatterometer will be introduced in detail in the following.

2.5.1 Scatterometer

The ERS Scatterometer is a real aperture pulse radar which is carried by both ERS-1 (since 1991) and ERS-2 (since 1994), working at 5.3 GHz (C-band) designed to acquire the backscattered signal from the Earth's surface. The measurements at C band are independent of cloud coverage and illumination by the sun. The Scatterometer has three antennae looking 45° forward, sideways and 45° backward, with respect to the satellite's flight direction It illuminates a 500km wide swath as the satellite moves along the orbit (see Figure 2.10). The incidence angle across the swath varies from a minimum of about 18° to a maximum of about 56°.

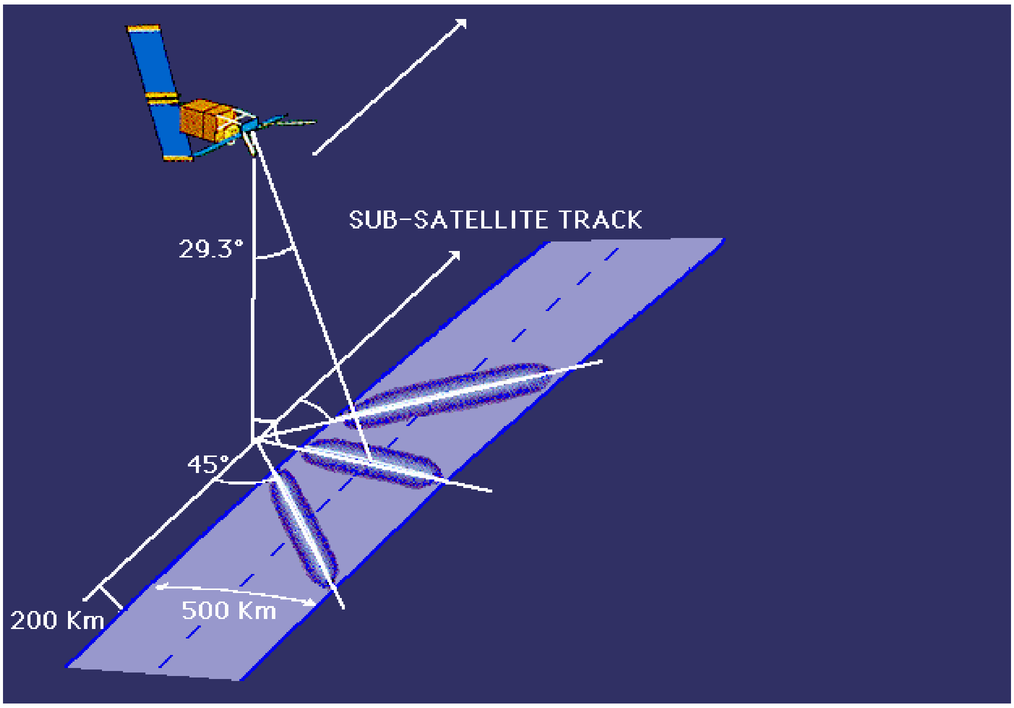

Figure 2.10: Geometry of the ERS wind scatterometer (adapted from Giovanna et al. 2007, Fig. 1) The three wind scatterometer antennae generate radar beams 45^{o} forward, sideways and 45^{o} backwards across a 500 km wide swath, 200 km to the right of the sub-satellite track.

The scatterometer can derive information on the wind (speed and direction) by measuring the radar return signal due to ocean surface roughness, this signal is usually called normalised radar cross section σ_0 (NRCS). The scatterometer is sensitive to the sea surface roughness which in fact is directly related to the wind characteristics. A typical empirical scatterometer geophysical model function has been developed by Stoffelen and Anderson (1997). Various validations and comparisons have been carried out with ERS scatterometer wind speed data. The standard deviation of wind speed and wind direction is 2 m/s and 20º, the bias is only 0.3 m/s for wind speed and 0.8º for wind direction (Lecomte, 1998). There is evidence that the scatterometer wind speeds are less accurate at low incidence angles, especially at low wind speeds (Stoffelen and Anderson, 1992)

It is important to note that the C-band scatterometer carried by ERS-2 operates simultaneously with the SAR wave mode. This indicates that the SAR wave mode imagettes are interlaced to the scatterometer swath, and a precisely collocated scatterometer wind vector can be fitted to each SAR imagette.

The scatterometer wind speed data used in this study is from the Centre for Satellite Exploitation and Research (CERSAT) of the French Institute of Research for the Exploitation of the Sea (IFREMER, http://cersat.ifremer.fr/). The IFREMER scatterometer wind products are computed with the Cmod-Ifr2 model developed by the department of Oceanography from Space at IFREMER. The time series of IFREMER is geolocated into 50km × 50km resolution cells. The product size is 500km × 500km. Backscattering cross sections are sampled every 25 km for the usual resolution products. Each product contains a header and 361 data records. It corresponds to 19 lines in the along track direction, each line containing 19 pixels. A data file contains the data from one satellite over-pass. The maximum number of products per pass is 88. Each data record includes the position, azimuth, incidence angle and Kp value, which is computed to give an estimate of the measurement uncertainty of the backscatter, for the 3 beams, speed and direction for the four first alias winds and for the interpolated meteorological wind, and the rank of the dealiased wind vector. A more detailed introduction into this wind field characteristics can be found in Bentamy et al. (1996).

2.5.2 Altimeter

Satellite altimetry has already been developed in the 1960s, and since then many satellites were launched such as Seasat (1978), Geosat (1985-1989), ERS (1991 to the present), TOPEX/POSEIDON (1992 to the present) and Jason (2001 to the present). The radar altimeter can measure the topography of the sea surface globally and frequently by measuring the range from the satellite to the sea surface. Such measurements have a wide range of applications in oceanography, geodesy, and geophysics, especially the marine wind and wave fields derived from the altimeter echo

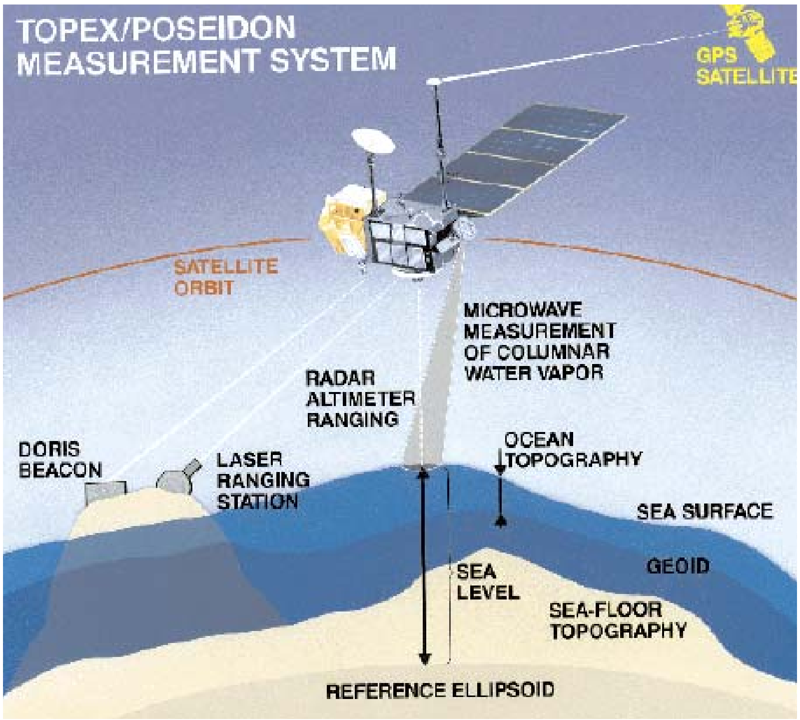

Figure 2.11: Schematic diagram of a satellite radar altimeter system. (Adapted from R. Cheney 2001 Fig. 1)

The measurement principle of an altimeter is described in Fig 2.11. The altimeter transmits a short pulse of microwave radiation with known power towards the sea surface. The pulse interacts with the rough sea surface and a very small part of the incident radiation is reflected back to the altimeter. Two basic geometric measurements are involved during this process. First, the distance between the satellite and the sea surface is determined from the travel time of the microwave pulses emitted downward by the satellite's radar to the sea surface and reflected back to the satellite. For the second measurement, independent tracking systems are used to compute the satellite's three-dimensional position relative to a fixed earth coordinate system. Combining these two measurements yields profiles of sea surface topography, or sea level.

In addition to sea surface topography, altimetry provides indirect measurements of ocean wave height and wind speed. This is made possible by the analysis of the shape and intensity of the reflected radar signal: a calm sea sends the signal back almost perfectly, like a flat mirror, whereas a rough sea scatters and deforms it. Wave height measurements are accurate to about 0.5m or 10% of the significant wave height. Wind speed can be measured with an accuracy of about 2 m/s (Komen et al., 1996).

The accuracy of wave height and wind speed measurements strongly depends on the precision with which an altimeter measures the shape of the sea surface. A long way has been needed to improve the precision of altimeter measurements as obvious from Table 2.5.

Table 2.5: The improvement of altimeter measurement precision (Adapted from Robinson I. S., 2004, Table 11.1)

Satellite	Mission Period	Precision per Radar Pulse(cm)
GEOS-3	Apr. 1975-Dec. 1978	25
Seasat	Jul. 1978-Oct. 1978	5
Geosat	Mar. 1985-Dec. 1989	4
ERS-1	Jul. 1991-May 1996	3
TOPEX/POSEIDON	Oct. 1992-present	2
ERS-2	Aug. 1995-present	3

Altimeter data from the ERS-2 satellite, reprocessed by ESA, were used in this study. The significant wave height altimeter data used in this study are full time and space resolution original data from ERS-2 every second, i.e. every 6 km. More detail about the ERS-2 altimeter data can be found at website: http://www.esa.int/.

2.5.2 HOAPS

The wind speed data set used in this study from the Hamburg Ocean Atmosphere Parameters and Fluxes from Satellite (HOAPS) is part of a multi satellite product for many parameters over the global ice free ocean. All variables are derived from the US Special Sensor Microwave/Imager (SSM/I) measurements, except for the SST which stems from the NODC/RSMAS Pathfinder data set. SSM/I characteristics are introduced in the following Table 2.6.

The SSM/I has operated on all satellites of the US Department of Defense Meteorological Satellite Program (DMSP) since June 1987. All DMSP satellites are in a near polar, sun synchronous orbit at an altitude of approximately 830 km above the earth with an orbital period of about 101 minutes. Sun-synchronous orbits are described in terms of their daytime equatorial crossing times and their inclination, which is about 98.8° for all DMSP satellites. The SSM/I is a conical scanner that operates with an incidence angle at the sea surface of 54°. Table 2.6 gives details about the SSM/I sensor, and a more detailed description is given by Hollinger et al. (1990).

As listed in Table 2.6, it takes 1.9 seconds for SSM/I instruments to complete one conical scan, whose area is limited to a maximum nadir opening angle of 102.4°, corresponding to a 1400 km swath on the Earth's surface. SSM/I measurements can provide complete coverage of the earth every two to three days except for small patches near the poles. Each scan (arc) is separated by 12.5 km along the ground track direction. The footprint for each SSM/I frequency is an ellipse formed by the cross scan and the along scan mirror movement, whose sizes are displayed in Table 2.6.

Table 2.6: Characteristics of the SSM/I sensor.

Frequency bands (GHz)	19.35	22.235	37.0	85.5
Polarisation	V,H	V	V,H	V,H
Integration time (ms)	7.95	7.95	7.95	3.89
Footprint size (km^2)	43×69	40×50	28×37	13×15
Sample interval along track (km)	25	25	25	12.5
Sample interval along scan (km)	25	25	25	12.5
Altitude of satellite (km)	830-860			
Swath width (km)	~1400			
Scan	A parabolic reflector rotates once every 1.9s at 45° about a vertical axis, scanning a 102.4° which are centred at the aft ground track.			

The wind speed close to the ocean surface is retrieved from the brightness temperature measurements of SSM/I which results from the variable emission at different surface wave conditions for different wind speeds. Factors such as rain that roughen the sea surface can result in enhanced brightness temperatures, thus the wind speed contains large errors with heavy rain. Davis (1999) gives estimates of the effect on wind speed retrievals.

HOAPS is a multi-satellite product consisting of measurements from all available SSM/I instruments (Table 2.7). F11 has been set as a reference because of its good performance. The different contributing SSM/I instruments were fixed to F11 by careful intercalibration. The wind speed algorithm in the current HOAPS-3 data set uses a neural network to derive the wind speed at 10 m height above the sea surface. It consists of 3 layers: an input layer with 5 neurons (brightness temperatures from the 19.35GHz, V; 19.35GHz, H; 22.235GHz, V; 37GHz, V channels, described in Table 2.6), a hidden layer with 3 neurons and an output layer with one neuron (wind speed). The network was trained with a composite data set of buoy measurements and radiative transfer simulations.

To avoid mis-detection of wind speed, the HOAPS retrieval procedure filters pixels which contain substantial atmospheric contamination e.g. by rain. The filtering uses brightness temperature thresholds for 19 and 37 GHz channels. If one of these thresholds is exceeded the corresponding pixel is flagged and wind speed is not calculated. For rain rates above 6 mm/h all pixels are flagged.

Table 2.7: Satellites used for HOAPS. LT and LST represent local time and local solar time. It should be noted that F10 did not reach the desired orbit, as a result the equatorial crossing time increased by about 45 minutes per year.

Satellite	F08	F10	F11	F13	F14	F15
Start date	1987-07-09	1991-01-07	1992-01-01	1995-09-01	1997-06-01	2000-03-01
End date	1991-12-31	1996-12-31	1999-12-31	2005-12-31	2005-12-31	2005-12-31
Equatorial crossing time	06:17 (LT)	22:09 (LT)	18:25 (LT)	18:33 (LST)	19:08 (LST)	21:05 (LST)

Three HOAPS-3 data sets are available, HOAPS-G and HOAPS-C can be downloaded from the CERA database at http://cera-www.dkrz.de/cera/:

- HOAPS-G: The default spatial resolution of HOAPS-G is 0.5 degrees on a global grid. Pentade, monthly and climatological means are available, consisting of multi-satellite averages including all SSM/I instruments available at the same time.
- HOAPS-C: This data set contains 1 degree twice daily globally gridded multi-satellite composite products, providing high temporal resolution. Each grid-cell contains data from one satellite pass, there is no average from two or more satellite.
- The HOAPS-S data set contains all retrieved physical parameters in the original SSM/I scan resolution for every individual satellite, HOAPS-S data is used as input to obtain HOAPS-G and HOAPS-C and is not provided with the CERA data base but only on request via email for specified limited time periods.

The HOAPS wind speed data is used for direct comparison with CWAVE results in this study. For a more detailed description of HOAPS please refer to Andersson et al. (2006) or the HOAPS website at www.hoaps.org.

2.6 ERA-40 Model Reanalysis

The ERA 40 data sets, which have been calculated at the European Centre for Medium-Range Weather Forecasts (ECMWF), using its Integrated Forecasting

System (IFS, a coupled atmosphere-wave model) with variational data assimilation, are a global atmospheric and oceanic analysis of many conventional observations and satellite data streams for the period September 1957 to August, 2002. The basic analysed variables include not only the conventional meteorological wind, temperature and humidity fields, but also stratospheric ozone and ocean-wave and soil conditions. All of these varables which can be found from the website http://data.ecmwf.int/data/d/era40_daily/ contain daily and monthly analyses and forecast values interpolated to a 2.5°×2.5° regular latitude/longitude grid. Of these variables, wind speed, significant wave height and mean wave period are used in this study for comparison with CWAVE results. These variables are extracted from ERA-40 GRIB type datasets at the four synoptic hours 00:00, 06:00, 12:00 and 18:00 UTC each day.

The ERA 40 ocean wave data used in this study have been validated by Caires and Sterl (2001) using the American, UK and Canadian Buoy Networks, Geosat and Topex satellites products and the hindcasts of the ODGP2 (Ocean Data Gathering Program version 2) wave model (Cox and Swail, 2001). A few points to which one should pay attention are listed now:

- Many kinds of observations have been assimilated in the ERA 40 reanalysis data, such as SSM/I 1D-Var winds from July 1987 onwards, the available buoy winds from June 1990, the available altimeter wave height Fast Delivery Product (FDP) data from the ERS 1/2 satellites, the scatterometer winds over oceans from April 1992 onwards. It should also be noted that data for the periods from September 1957 to November 1991 and from June 1993 to December 1993 had no altimeter wave height data assimilation; ERS-1 FDP altimeter wave-height data were assimilated into ERA-40 from December 1991 onwards. The data are, however, of poor quality during the first two years due to an external processing error. Assimilation of the FDP data was halted as soon as this problem was realised, production having reached May 1993; assimilation was resumed in January 1994 using good but uncalibrated ERS-1 FDP data up to May 1996; FDP ERS-2 measurements of wave height have been assimilated in ERA-40 from June 1996 onwards. Before the 80's, the Voluntary Observing Ships (VOS) and the Comprehensive Ocean-Atmosphere Data Set (COADS) were used when hardly any other observations were available.
- The ERA 40 data are high quality for the mean wave and wind characteristics.
- The ERA 40 significant wave height compare well for values between 2 and 4 meters both in terms of monthly means and of data at synoptic times. However, the ERA 40 reanalysis results tend to underestimate high waves and overestimate very low values. On average there is an underestimation of about 0.5 meters.

- There is a better agreement between ERA 40 results and observations in terms of wind speeds than in terms of wave heights. The underestimated high wave heights do not always correspond to underestimated high wind.
- The ERA-40 mean wave periods are shown to compare well with the altimeter's results in non swell-dominated conditions.

Chapter 3

Wind Vector Retrieval Using ASAR Image Mode Data

Following the ERS-1/2 satellites, the ENVISAT advanced synthetic aperture radar was launched on March 1st, 2002, carrying the advanced synthetic aperture radar (ASAR) instruments which extended the mission of the Active Microwave (AMI) Synthetic Aperture Radar (SAR) instrumentation flown on the ERS-1/2 satellites. ASAR uses an active phase-array antenna, with incidence angles between 15 and 45 degrees. ASAR is an all-weather, day-and-night, high-resolution imaging instrument that can provide radar backscatter measurements indicative of terrain structure, surface roughness, and dielectric constant. Compared with ERS-1/2 SAR, the new features of ASAR include beam steering for acquiring images with selectable incidence angles, dual polarization, and wide swath coverage.

Firstly, ASAR could provide continuity of the ERS SAR Image and Wave Modes but with the opportunity for better temporal frequency of coverage. The nominal spatial resolution and swath coverage of ASAR Image Mode are the same as the ERS Image Mode, and ASAR is also in a 35-day repeat orbit. However, using beam steering, it becomes possible to obtain images of the same area on the ground from different orbits with different incidence angles.

Secondly, ASAR has dual polarization capabilities, a special Alternating Polarization Mode has been implemented that permits half of the looks from a scene to be acquired with horizontal and half with vertical polarization, thereby considerably increasing the target classification capability and providing more information on the target. This provides the opportunity for eliminating the inherent 180° ambiguity when retrieving wind field using ASAR image.

Thirdly, wide area coverage is achieved by switching between different swaths using the ScanSAR technique. This enables 405 km coverage at resolutions of 150 m or 1 km. At 1 km resolution, the data rate is low enough for tape recording on board and the spacecraft and the recording capacity is sufficient for downloading low-resolution global coverage through a single receiving station. Considering these advantages of ASAR image, it is used to retrieve the wind field in coastal areas.

In recent years, several algorithms have been developed and applied for SAR wind retrievals (Alpers and Brummer, 1994; Fetterer et al., 1998). Common among these are the CMOD4 (Stoffelen and Andersen, 1993) model and CMOD_IFR2 (Quilfen and Bentamy, 1994) model. The CMOD4 model was originally developed for the ERS-1 scatterometer (Stoffelen and Andersen, 1997) and it has been shown to give reasonable estimates of wind speed when applied to ERS SAR images (Johannessen et al., 1994). The model is based on the backscatter from a rough ocean surface at moderate incidence angles (20º–60º), which is dominated by resonant Bragg scattering (Valenzuela, 1978). The CMOD_IFR2 model was applied for the retrieval of tropical cyclones (Quilfen et al., 1998). Since predicted NRCS values were found to increase too fast with the wind speed (Bentamy et al., 1994), high wind speed is likely to be underestimated. Thus a bias correction is applied to better estimate high wind in CMOD_IFR2 model. However, little comparison has been done between the CMOD4 model and CMOD_IFR2 model using them to retrieve ENVISAT ASAR wind vector in high sea-state conditions.

In this chapter, two models (CMOD4 and CMOD_IFR2) are compared in a case study. The wind direction information is extracted from linear, low frequency components of the ASAR image. This result would have an inherent 180º ambiguity with respect to the wind direction since only one ASAR image is used. The NOAA buoy data have to be utilized to eliminate the ambiguity and to obtain the estimated wind direction.

Then, a new approach to retrieve wind vector from ASAR dual polarization data is developed. The new algorithm is deducted based on the combination of the co-polarization algorithm and the cross-polarization algorithm. Wind direction and wind speed could be directly obtained using the new algorithm without other information. Comparisons are made between the retrieved results using the new method and Quikscat and buoy data.

3.1 The Comparison between Two Wind Field Models

CMOD4 and CMOD_IFR are two common models used for retrieving wind fields from SAR images. But the comparison between them is seldom performed, especially in high sea state condition. It is necessary to compare them and select the better one. The better one will be used to develop the new algorithm in the next section.

3.1.1 ASAR, Quickscat and Buoy Data

The information on the ASAR image and the buoy data used in this section is summarized in Table 3.1. It can be seen that the temporal gap between ASAR and buoy is only 22.52 Min; however, the spatial gap between them is larger than 300 km.

Table 3.1: Summary of ASAR imagery and buoy data

	Date	Time	Location
ASAR	Nov. 15, 2003	08:22:37	N18°56′8″, W 155°49′37″
Buoy	Nov. 15, 2003	08:00:00	N17°8′35″, W 157°47′06″

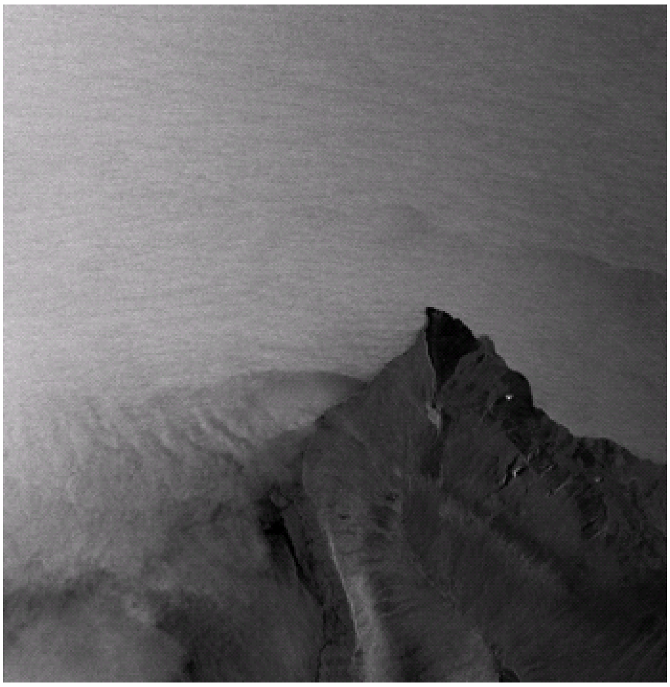

Figure 3.1: ENVISAT ASAR image acquired at 08:22:37 on November 15th, 2003

The ASAR imagery used in this article is a precision image (PRI) product from the European Space Agency (ESA) and it has 8413 pixels in range direction and 8580 pixels in azimuth direction (Fig.1). The pixel resolution is 12.5 m. The buoy data were collected by the US NOAA (National Oceanic and Atmospheric Administration) National Data Buoy Center (NDBC) and the National Weather Service (NWS). Both time and location between ASAR and buoy are consistent (Table 3.1). Thus we could use the buoy data to resolve the 180° ambiguity. The grid resolution of Quikscat data used to compare the wind retrieval result from ASAR imagery is 0.25°×0.25°. The resolution is high enough to validate the wind retrieval result from ASAR imagery.

3.1.2 Introduction of Both Model

CMOD4:

The CMOD4 model (Stoffelen and Andersen, 1997) provides NRCS values (σ_0) as a function of relative wind direction (ϕ), wind speed (U) and incidence angle (θ). The relationship (Stoffelen and Andersen, 1997) can be expressed as

$$\sigma_0 = b_0[1 + b_1 \cos\phi + b_3 \tanh b_2 \cos 2\phi]^{1.6} \tag{3.1}$$

Where,

$$b_0 = b_r 10^{\alpha+\gamma F(U+\beta)} \tag{3.2}$$

and

$$F(U+\beta) = \begin{cases} -10 & U+\beta \le 10^{-10} \\ \log(U+\beta) & 10^{-10} < U+\beta \le 5 \\ \sqrt{U+\beta}/3.2 & U+\beta > 5 \end{cases} \tag{3.3}$$

α, β, γ, b_1, b_2, and b_3 are expanded as Legendre polynomials P_i with $i = 1, 2, 3$ to a total of 18 coefficients.

b_r is a residual correction factor to b_0, given as a look-up table as a function of incidence angle.

$$\alpha = c_1 P_0 + c_2 P_1 + c_3 P_2 \tag{3.4}$$

$$\gamma = c_4 P_0 + c_5 P_1 + c_6 P_2 \tag{3.5}$$

$$\beta = c_7 P_0 + c_8 P_1 + c_9 P_2 \tag{3.6}$$

$$b_1 = c_{10} P_0 + c_{11} U + (c_{12} P_0 + c_{13} U) F^2(x) \tag{3.7}$$

$$b_2 = c_{14} P_0 + c_{15}(1 + P_1) U \tag{3.8}$$

$$b_3 = 0.42(1 + c_{16}(c_{17} + x)(c_{18} + U)) \tag{3.9}$$

$$F^2(x) = \tanh(2.5(x + 0.35)) - 0.61(x + 0.35) \tag{3.10}$$

where the Legendre polynomials are

$$P_0 = 1\text{，}\quad P_1 = x\text{，}\quad P_2 = (3x^2 - 1)/2 \tag{3.11}$$

with $x = (\theta - 40)/25$, θ is in degree unit and the constants c_1 to c_{18}.

Values of residual factor b_r are given in Table 3.2.

Table 3.2: Values of residual factor b_r

θ (deg)	b_r	θ (deg)	b_r	θ (deg)	b_r
16	1.075	31	0.927	46	1.054
17	1.075	32	0.923	47	1.053
18	1.075	33	0.930	48	1.052
19	1.072	34	0.937	49	1.047
20	1.069	35	0.944	50	1.038
21	1.066	36	0.955	51	1.028
22	1.056	37	0.967	52	1.056
23	1.030	38	0.978	53	1.016
24	1.004	39	0.988	54	1.002
25	0.979	40	0.998	55	0.989
26	0.967	41	1.009	56	0.965
27	0.958	42	1.021	57	0.941
28	0.949	43	1.033	58	0.929
29	0.941	44	1.042	59	0.929
30	0.934	45	1.050	60	0.929

CMOD_IFR2:

The CMOD_IFR2 model (Quilfen et al., 1998) is formulated as follows:

$$\sigma_0 = 10^{m+n\sqrt{U}}(1 + d_1 \cos\phi + \tanh b_2 \cos 2\phi) \tag{3.12}$$

where

$$m = s_1 + s_2 l_1 + s_3 l_2 + s_4 l_3, \tag{3.13}$$

$$n = s_5 + s_6 l_1 + s_7 l_2, \tag{3.14}$$

$$d_1 = s_8 + s_9 V_1 + s_{10} Q_1 + s_{11} Q_1 V_1 + s_{12} Q_2 + s_{13} Q_2 V_1, \tag{3.15}$$

$$\begin{aligned} b_2 = s_{14} + s_{15} Q_1 + s_{16} Q_2 + (s_{17} + s_{18} Q_1 + s_{19} Q_2) V_1 + \\ (s_{20} + s_{21} Q_1 + s_{22} Q_2) V_2 + (s_{23} + s_{24} Q_1 + s_{25} Q_2) V_3 \end{aligned} \tag{3.16}$$

where $l_1 = t,\ l_2 = (3t^2 - 1)/2,\ l_3 = t(5t^2 - 3)/2,\ t = (\theta - 36)/19,\ Q_1 = y,\ Q_2 = 2y^2 - 1,$ $y = (2\theta - 76)/40,\ \ V_1 = (2U - 28)/22,\ \ V_2 = 2V_1 - 1,\ \ V_3 = (2V_2 - 1)V_1,\ \ s_1$ - s_{25} are constants.

After the wind speed U has been calculated from the model (3.12), the following bias correction is added:

$$U_{last} = U + U_{bias} \tag{3.17}$$

with

$$U_{bias} = \begin{cases} 0 \quad if\ U \le 10 \\ 0.0831 \times U_{10} - 0.0173 \times U_{10}{}^{2} + 0.0009 \times U_{10}{}^{3} \quad if\ 10 < U \le 22 \\ \arctan(U - 22) + 3.0382 \quad if\ U > 22 \end{cases} \tag{3.18}$$

3.1.3 The Application of Both Models

Both models need to first decide on the wind direction to further retrieve wind speed. By calculating the direction of wind rows in ASAR imagery, the wind direction is estimated.

Firstly, ASAR imagery is divided into many subscenes of the 2048 ×2048 pixels image, and carried out radiometric calibration for each subscene to convert the image data into σ_0. Since the wind rows are large compared to the pixel resolution, we averaged over eight times eight pixels in range and in azimuth directions, then we removed low frequency variability in the imagery by applying a Wiener filter several times.

Secondly, Fast Fourier transforms (FFTs) were applied for every subscene. The objective of this step is to reduce noise for a high spectral peak. Fig. 3.2 depicts the ASAR image spectra. The orientation of the spectral peak can be easily seen from Fig.3.2 to point towards 149°/329°. Since the wind rows in ASAR imagery are linear, we need to rotate the angle of the spectral peak by 90° to obtain the wind direction according to the boundary-layer rolls theory (Gerling, 1986). Thus, the dashed strait line in Fig. 3.2 indicates the retrieved wind direction and the arrow represents the wind direction measured by the buoy. Thirdly, the 180° ambiguity in the wind direction is resolved using the buoy wind direction. The estimated wind direction in Fig. 3.2 is approximately 59°. Thus we have obtained the wind direction estimation from the ASAR imagery.

Then we move on to retrieve wind speed for both the CMOD4 and CMOD_IFR2 models. As input we have the estimated wind direction and the incidence angle of the subscene to compute σ_0 and wind speed. When the difference between the computed σ_0 and the σ_0 of the subscence reached the minimum value, the corresponding wind speed was obtained as the model result.

Table 3.3 shows the wind vector retrieval results using ASAR imagery. There are only 8 subimages can be used to retrieve wind field in this ASAR image. The retrieval results agree well with the wind vector taken from Quikscat. The Quikscat data were taken at 2:08 on November 15th, 2003. The difference in location between each subscene and the Quikscat data was within 0.1°.

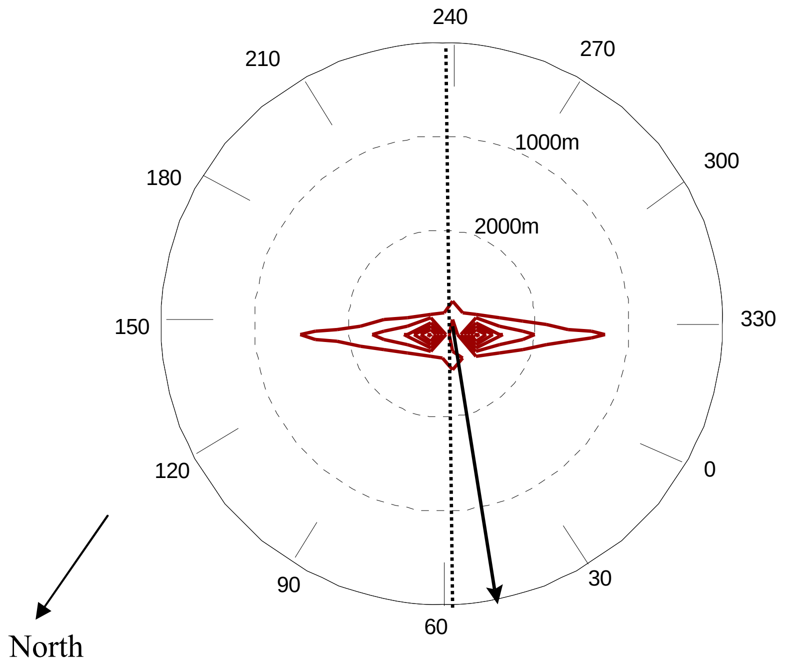

Figure 3.2: ASAR image spectra obtained from every subscene using FFT, the bin size of spectra is 0.09 rad/m.

The statistical analysis of retrieval results and Quikscat data shows a RMSE of wind direction of 2.80° and of 1.09 m/s or 0.60 m/s wind speed for CMOD4 model and CMOD_IFR2, respectively.

Table 3.4 shows the comparison between the retrieval results and the buoy data. The retrieval results we choose to compare with the buoy data were the closest to the buoy location. The comparisons to Quickscat and buoy have shown that the wind speed retrieval results using CMOD_IFR2 model are slightly better than for CMOD4.

Table 3.3 Comparison of wind speed and direction for the SAR image and Quickscat.

Wind speed (m/s)			Wind direction (º)	
CMOD4	CMOD_IFR2	Quikscat	Retrieval from ASAR	Quikscat
13.01	13.35	13.60	58.02	60.23
13.60	13.79	14.01	58.14	60.13
13.70	14.67	14.40	57.32	55.03
12.65	13.98	14.52	42.56	39.87
14.25	14.66	13.51	63.23	65.01
14.78	14.13	13.94	65.11	63.90
15.72	14.98	14.38	57.08	62.86
11.56	10.98	10.18	59.04	57.22

Table 3.4: Comparison between the retrieval results and buoy data

Wind speed (m/s)			Wind direction (°)	
CMOD4	CMOD_IFR2	buoy	Retrieval from ASAR	buoy
13.01	13.35	13.20	58.02	56

3.2 Development of a New Algorithm

In this section, a new algorithm is derived to retrieve wind speed and wind direction from ASAR dual polarization image without other prior information. The retrival results are validated by buoy data, and also compared to Quickscat data.

3.2.1 Derivation of the New Algorithm

Publications by Stoffelen and Anderson (1997) and Quilfen et al. (1998) have proven that the C band empirical model-CMOD algorithm can be used to retrieve the wind field from a SAR image. The co-polarization algorithm CMOD_IFR2 provides co-polarization NRCS values (σ_{kk}) as a function of relative wind direction (ϕ), wind speed (U) and incidence angle (θ). The relationship which is the same as Eq. 3.12 can be expressed as

$$\sigma_{kk} = 10^{m+n\sqrt{U}}(1 + d_1 \cos\phi + \tanh b_2 \cos 2\phi) \tag{3.19}$$

The detailed meaning of each parameter can be found in Section 3.1.2.

The cross-polarization algorithm (Tsai et al., 2000) is formulated as follows:

$$\sigma_{\mu\tau} = \alpha_1 \sin\phi + \alpha_2 \sin 2\phi \tag{3.20}$$

where σ_{kk} and $\sigma_{\mu\tau}$ denotes the value of co-polarization NRCS and cross-polarization NRCS, respectively. d_1, b_2, m, n, α_1 and α_2 are functions of wind speed, incidence angle and polarization.

Where

$$\alpha_1 = -\xi\delta\alpha, \tag{3.21}$$

$$\alpha_2 = \xi(1+\delta)\alpha, \tag{3.22}$$

Usually one assumes $\xi = 1$; then

$$\alpha = \frac{\sqrt{e_V}\,\rho\sigma_{kk}(\phi = 60^{\text{o}})}{(1+\delta)\sin(120^{\text{o}}) - \delta\sin(60^{\text{o}})}, \tag{3.23}$$

with

$$\rho = 0.5\rho_0(1+\theta/30), \tag{3.24}$$

$$\begin{aligned}\rho_0 &= 5.234187\times10^{-2}U - 4.635087\times10^{-3}U^2 + 1.5992\times10^{-4}U^3 \\ &\quad - 2.4191\times10^{-6}U^4 + 1.3440\times10^{-8}U^5\end{aligned} \tag{3.25}$$

e_V and δ are constants, e_V represents the ratio of cross polarization.

Let $p_1 = \sigma_{\mu\tau}$, $p_2 = \sigma_{\kappa\kappa}10^{-m-n\sqrt{U}} - 1$ and $d_2 = \tanh b_2$, then Eq. (3.19) and Eq. (3.20) can be rewritten as:

$$d_1 \cos\phi + d_2 \cos 2\phi = p_2 \tag{3.26}$$

$$\alpha_1 \sin\phi + \alpha_2 \sin 2\phi = p_1 \tag{3.27}$$

After a simple algebraic calculation, we get,

$$\left(\frac{-d_1 + \sqrt{d_1{}^2 + 8d_2(p_2+d_2)}}{4d_2}\right)^2 + \frac{4d_2{}^2 p_1{}^2}{\left(2\alpha_1 d_2 - \alpha_2 d_1 + \alpha_2\sqrt{d_1{}^2 + 8d_2(p_2+d_2)}\right)^2} = 1 \tag{3.28}$$

$$\sin\phi = \frac{2d_2 p_1}{2d_2\alpha_1 - d_1\alpha_2 + \alpha_2\sqrt{d_1^{\,2} + 8d_2(p_2 + d_2)}} \tag{3.29}$$

$$\cos\phi = \frac{-d_1 + \sqrt{d_1^{\,2} + 8d_2(p_2 + d_2)}}{4d_2} \tag{3.30}$$

As shown in Eq. (3.28) there is only one unknown variable, wind speed. By iteration wind speed U can be obtained. Substituting the value of wind speed, incidence angle and the value of NRCS into Eq. (3.29) and (3.30) allows us to obtain wind direction as well.

3.2.2 Application and Comparison

An ENVISAT ASAR dual polarization image (Fig. 3.3) is used in this study to retrieve the wind field using the above new method. Imaging radars can transmit horizontal (H) or vertical (V) electric-field vectors, and receive either horizontally or vertically polarized return signals, or both. ENVISAT ASAR can provide dual-channel data. In Alternating Polarization Mode (AP Mode), it provides one of three different channel combinations: VV and HH, HH and HV and VV and VH. The ASAR image used in this study has VV and VH polarization, received by the China Remote Sensing Satellite Ground Station (RSSG) in Beijing, China and it has 8210 pixels in the range direction and 6484 pixels in the azimuth direction. The pixel resolution is 12.5 meter. The ASAR image was acquired at 2:25 UTC on April 6, 2004 and its central position is at 20.60º N, 113.19º E in the East China Sea.

For comparison Quickscat wind field data was used. The wind information of Quikscat was acquired at 2:08 on April 6, 2004 17 minutes before the ASAR image. The horizontal resolution of Quikscat data is 0.25°×0.25°, which is high enough to validate the wind retrieval result from the ASAR image.

Buoy data provided by the National Marine Environmental Forcasting Center is also used to validate the new results. The buoy wind vector data was acquired at 3:00 UTC on April 6, 2004 and located at 21.5°N, 114.0°E which is near the ASAR image.

There are three steps in this new method to obtain wind vector from ASAR dual polarization data. First, we divide the co-polarization image and cross-polarization image into 2048 by 2048 pixel subscenes respectively and the radiometric calibration is carried out in each of the subscenes to convert the image data into σ_{kk} and $\sigma_{\mu\tau}$. Next, using σ_{kk}, $\sigma_{\mu\tau}$ and incidence angle in Eq. (3.27), we obtain after iterative calculation wind speed U. Finally, substituting σ_{kk}, $\sigma_{\mu\tau}$, V, and incidence angle into Eq. (2.28) and (3.29) allows us to obtain wind direction.

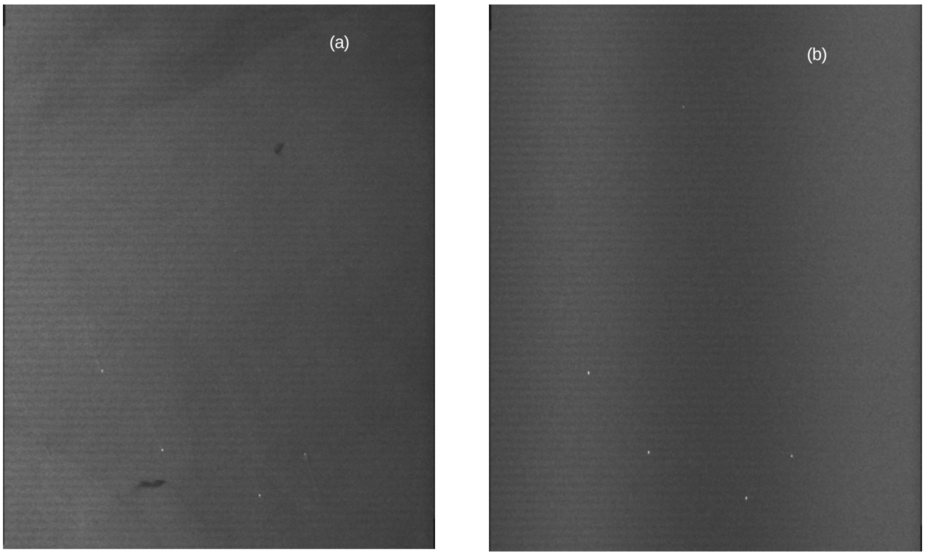

Figure 3.3: ENVISAT dual polarization ASAR image acquired at 2:25 UTC on April 6, 2004. (a) VV polarization; (b) VH polarization.

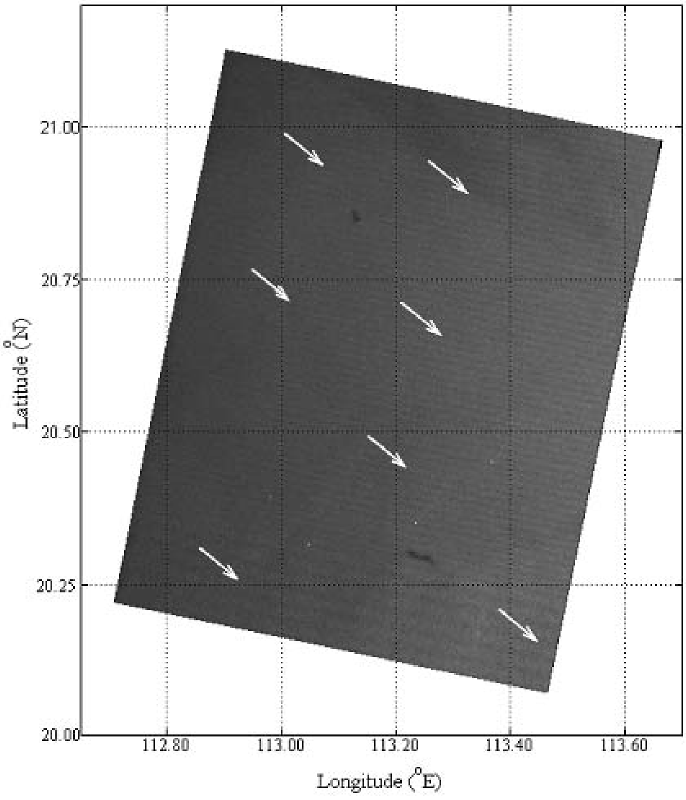

Figure 3.4: The wind vector plot of the new method results

Table 3.5 shows the wind retrieval results from ASAR dual polarization image applying the method discussed above. There are only seven subscenes which can be used to retrieve wind field because the others are contaminated by slicks or ships. It can be seen from Table 3.5 that the retrieval results from the ASAR image agree well with the wind vector acquired from Quikscat. The difference of location between each subscene and the Quikscat data does not exceed 0.1°. The root mean square (rms) error of wind direction and wind speed are only 2.21° and 0.53 m/s, respectively.

The wind vectors are plotted in Fig. 3.4. The ASAR image is put into the corresponding geophysical location. The direction of the arrow represents the wind direction and the lenghth of the arrows is proportional to wind speed.

Table 3.5: Comparison of wind speed and wind direction between retrieval results and Quickscat data

Location(°)		Wind speed (m/s)		Wind direction (°)	
Longitude	Latitude	New method	Quikscat	New method	Quikscat
113.005	20.989	5.65	5.19	121.80	123.84
113.258	20.945	5.84	5.23	127.19	129.96
112.956	20.762	4.17	4.73	122.25	124.23
113.208	20.713	6.02	5.32	122.47	124.35
113.159	20.489	4.85	5.44	125.09	123.98
112.858	20.308	5.48	5.09	121.11	124.19
113.381	20.209	5.67	5.94	126.51	124.44

Table 3.6: Comparison between the retrieval results and buoy data

Wind speed (m/s)		Wind direction (°)	
New method	5.65	New method	121.80
Traditional method	5.74	Traditional method	122.12
Buoy	5.0	Buoy	120.0
Quikscat	5.19	Quikscat	123.84

The corresponding retrieval results are also compared with the buoy data, see Table 3.6. The results from the ASAR dual polarization image are in agreement with the buoy data. Traditional method here means that the wind field results are obtained from the empirical algorithm-CMOD4. The new method fits better with the buoy data both in wind speed and wind direction. The accuracy of buoy measurements is only up to 0.1, so the precision of buoy measurements need further improvement.

3.3 Discussion

In this chapter two traditional models CMOD4 and CMOD_IFR2, are compared and assessed using an ASAR image. In a case study, the performace of CMOD_IFR2 is better than CMOD4 in high sea state condition, however, this needs much more data to validate this conclusion.

Another point of this section is that a new method to retrieve ocean wind vector using dual polarization ASAR image was developed. Results appear to fit Quikscat data and buoy data well. There are two advantages of this new method: wind direction of 180º ambiguity is eliminated without using information from other sources such as numerical model analyses, predictions or buoy data. The other is that the retrieval is possible for very small spatial scales. Results of small-scale wind fields could be obtained with the new method. Much more work has to be done to further validate the method, using many more ASAR images.

Chapter 4

Assessment of CWAVE results

In situ sea state measurements such as significant wave height, near sea surface 10 meters wind speed and wave period are rare, especially far off-shore. The first and most common observation before the satellite era was the estimation of the sea state by mariners. Data quality was limited to shipping routes and depended on the experience of the observer. Another source for sea state measurement is buoys equipped with different sensors. However, most of the buoy measurements are also restricted to coastal areas. These measurements can not meet the global research requirements. Remote sensing with altimeters, synthetic aperture radars (SAR) and scatterometers offers a number of different methods for acquiring information on the open ocean and coastal regions. The SAR is the only instrument which can provide high-resolution two-dimensional sea state information in principle on a global scale and continuously. Another advantage of SAR is that it can retrieve high resolution met-ocean parameters in coastal areas with full coverage.

SAR onboard the ESA satellites ERS-1 and ERS-2 can observe the sea surface in wave mode over the global oceans. Information from these (5 km×10 km) wave mode imagettes is delivered as an ESA product, in form of two dimensional image spectra, which are used at weather centres to estimate ocean waves over the global oceans in nearly real time. The SAR image spectra are also used together with first guess information from a wave model to derive two dimensional ocean wave spectra in order to improve the ocean wave forecast.

The CWAVE empirical algorithm which has been developed by Schulz-Stellenfleth et al. (2007) can retrieve the met-ocean parameters significant wave height (H_s), wind speed (U_{10}) and mean wave period (T_m) from an ERS-2 wave mode image. Unlike other algorithms or methods (Hasselmann et al. 1996; Mastenbrok and Valk, 2000) which can not directly derive parameters from SAR image, the CWAVE algorithm only needs a wave mode image as input for the retrieval of met-ocean parameters. The technique is based on a least squares approach with a quadratic model function. An integral ocean wave parameter such as significant wave height, wind speed or mean wave period is estimated from a set of SAR parameters such as the radar cross section, the image variance, and 20 parameters computed from the SAR image variance spectrum using a set of orthonormal functions.

The main goals of this chapter are

firstly to validate two years of CWAVE SAR results against NOAA buoy data and ship data acquired onboard the research vessel Polarstern and,

Secondly, to compare the retrieved parameters to the ERS-2 satellite altimeter and scatterometer as well as HOAPS and ERA-40 reanalysis data.

The NOAA buoy data is chosen because it is the biggest buoy network all over the world and hence can provide high probability for collocation with CWAVE results. Another reason is that the buoy measurements are believed to be at present the most reliable and accurate source of sea state measurements. However, the collocated pairs between NOAA buoy data and two year-results from CWAVE are still not enough. So the observations from the research vessel Polarstern were also chosen to validate the CWAVE results. The scatterometer and altimeter results are chosen mainly because both of them are installed on both ERS satellites like the SAR instruments. The temporal gap between them is very small. HOAPS and ERA 40 are chosen because they are long data sets: HOAPS is a representation of mere satellite results and ERA 40 is a representation of a consistent reanalysis.

4.1 Validation of CWAVE with NOAA Buoy Data

In 1977 the NOAA buoy network was started and an increasing number of buoys have been deployed since then. As time went by, there was not only an increase in the number of buoys but also an increase in the detail of information they reported. Initially, buoys would measure only the significant wave height and mean wave period, whereas nowadays most of the buoys report the full directional wave spectrum. So the significant wave height can be calculated from the full directional wave spectrum. The relation $H_s = 4\sqrt{\sum F_d \Delta f}$ is used to calculate significant wave height from the directional wave spectrum (F_d), Δf is frequency step.

It should be noted here that the anemometers of the buoys used in this study are mounted at different heights from 3.8 m to 10 m above the ocean surface as introduced in Section 2.2.1. Hence some wind speed measurements must be transferred to the standard height. The relationship between the measured wind speed at a height Z, and the wind stress at the surface depends both on Z and on turbulence of the flow. Turbulence is determined by the wind shear and buoyancy of the atmosphere, and the buoyancy is dependent on the density stratification in the atmosphere. Thus conditions that cause identical wind stress, and therefore identical satellite-measured wind speeds, could have different measured wind speeds at a given height. Also, measured wind speeds at different heights would be different from each other, even under identical atmospheric conditions. Because of these effects, comparing satellite-derived wind speeds directly to buoy measured wind speeds must lead to large errors. Instead, we convert all buoy-measured winds to a standard height, here 10 meters.

In this study, we use the simple approach of assuming a logarithmically varying wind profile, so that the corrected wind speed at a height Z is given by

$$U(Z) = \ln(Z/Z_0)/\ln(Z_m/Z_0)*U(Z_m) \tag{4.1}$$

Where $U(Z)$ is the wind speed at height Z, Z_0 is the roughness length, and Z_m is the measurement height. This expression can be derived using a mixing-length approach assuming neutral stability with the typical oceanic value for Z_0 of 1.52×10^{-4} m (Peixoto and Oort, 1992). Note that this approach does not include effects due to differences in atmospheric stability, and therefore may lead to errors when atmospheric conditions differ from neutral stability.

In this section we explain how CWAVE results are compared to the NOAA buoys first, and then discuss the results of the comparisons both for significant wave height (H_s) and wind speed (U_{10}).

4.1.1 Method

H_s and U_{10} from CWAVE are validated by comparing them to NOAA buoy measurements. In order to make such a comparison, a set of measurements collocated both in time and in space must be generated. Each collocated CWAVE-buoy pair was produced using the following procedure. First, we try to find a buoy measurement that occurs nearly at the same time as the CWAVE result. Since most buoys in the data set produce data on an hourly basis, the ERS-2 SAR over flight time will typically be no more than 30 minutes from the closest buoy measurements. If the time difference between the buoy and CWAVE is above 30 minutes, the buoy measurement is not used.

Secondly we must find a buoy measurement spatially collocated with the CWAVE result. Since it is unlikely that the buoy is exactly centered in the SAR imagette the following spatial difference is calculated. We know that the ERS-2 SAR instrument acquires a wave mode imagette of 5×10 km^2 size every 200 km along the satellite track, so we can imagine a square box (100 km × 100 km) centered at the CWAVE measurement. If the buoy measurement is totally within this box, the observation of the buoy is used. If the buoy location is exactly at the edge of the box, then the buoy measurement can be used for two CWAVE measurements.

Collocated measurements were generated for each CWAVE-buoy pair over the period from September 1st 1998 to November 30th 2000. Typically, a year in which both the buoy and SAR were completely operational resulted in 600-800 collocated measurements.

The comparison statistics to be presented will be only for ordinary statistical parameters, which are listed as follows:

First we determine the bias,

$$bias = \overline{y} - \overline{x} \tag{4.2}$$

Second is the root-mean-square-error (RMSE),

$$RMSE = \sqrt{n^{-1} \sum_{i=1}^{n} (y_i - x_i)^2} \tag{4.3}$$

Third is the correlation coefficient (R),

$$R = \frac{\frac{1}{n} \sum_{i=1}^{n} (x_i - \overline{x})(y_i - \overline{y})}{\sqrt{\sum_{i=1}^{n} (x_i - \overline{x})^2 (y_i - \overline{y})^2}} \tag{4.4}$$

Sometimes the scatter index (SI) is also used in this study,

$$SI = \frac{RMSE}{\overline{x}} \tag{4.5}$$

In all these formulae y_i represents the CWAVE results and x_i the other data source, such as buoy measurements, altimeter or scatterometer, HOAPS results or ERA 40 reanalysis data.

4.1.2 Results and Discussion

Significant wave height validation by NOAA buoy data

In this section we carry out a comparison of H_s measurements using collocated SAR and buoy measurement pairs gathered using the method outlined in section 4.1.1. In Fig. 4.1 we present a typical scatter plot of difference between the CWAVE and the buoy significant wave heights as a function of the buoy significant wave height. The total number of collocated CWAVE-buoy data pairs is 1429 for the period from 1 September 1998 to 30 November 2000. All 96 NOAA buoys are selected for these collocations. The mean CWAVE significant wave height is 0.02 m higher than the NOAA buoy significant wave height for all these CWAVE-buoy pairs, and the overall standard deviation of the H_s differences is 0.61 m. However, Fig. 4.1 indicates that CWAVE results overestimate the H_s value for low sea state, and underestimate it for high sea states.

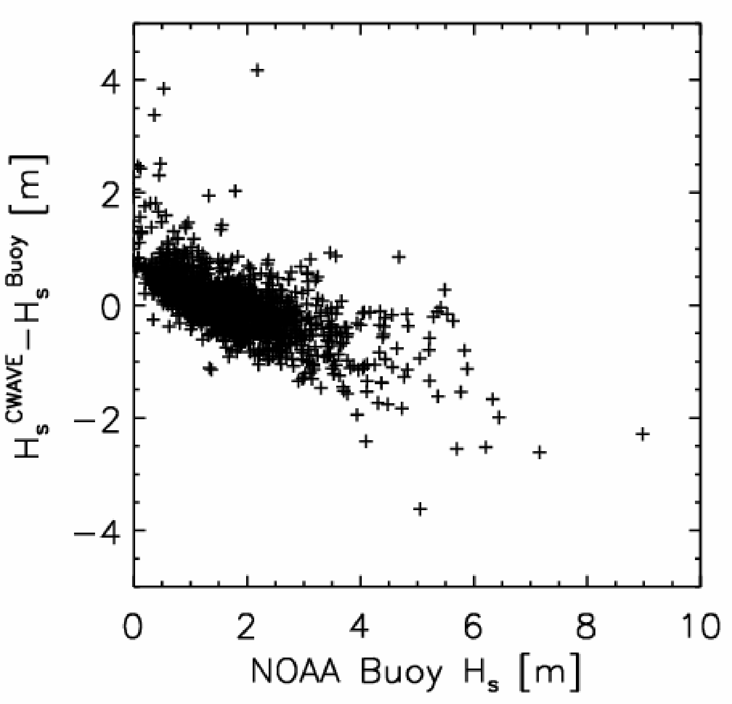

Figure 4.1: Scatter plot of significant wave height difference as a function of NOAA buoy significant wave height for all collocated CWAVE-buoy pairs. Each symbol corresponds to one CWAVE-buoy collocated measurement.

Neither the CWAVE nor the buoy significant wave height should be negative. Since the minimum value of the CWAVE significant wave height is zero, the minimum value of $H_S^{CWAVE} - H_S^{Buoy}$ is given by $-H_S^{Buoy}$. The data were then subdivivided into 0.91 m wide bins of the buoy significant wave height. The standard deviation of the CWAVE-buoy difference was then calculated, and the results are plotted in Fig. 4.2. The error bars are one standard deviation on each side of the mean. The maximum number of pairs is located in the second bin (0.91 m) which has 572 collocated pairs. The last three bins contain only one pair in fact. It can be seen that the buoy values become larger than CWAVE after the second bin. Most of the collocated pairs are contained in the first three bins with 1286 pairs. For each of the last three bins only one pair exists, therefore no standard deviation errors have been calculated.

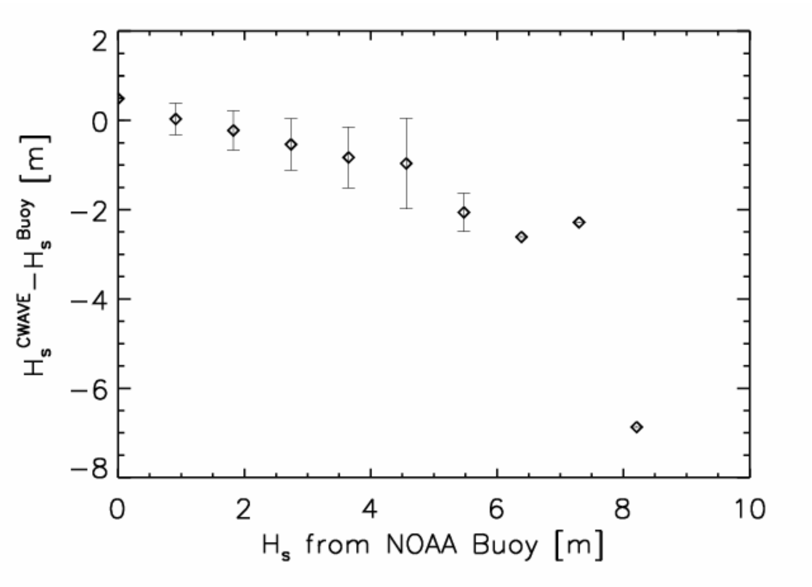

Figure 4.2: The binned mean differences of significant wave height as a function of NOAA buoy significant wave height, including standard deviation.

All 1429 collocated CWAVE-buoy H_s pairs have been plotted as a density scatter plot in Fig. 4.3. Most pairs (69%) lie within H_s equal to 0.5 m to 2 m, there is no substantial difference between CWAVE results and buoy measurements in this range. This is also the reason for the high correlation coefficient of 0.83.

The water depth has an effect on the comparison between the CWAVE results and buoy measurement as shown in Fig. 4.4. Firstly, in the low H_s part (H_s<0.5 m), the SAR results of both deep and shallow water are usually larger than the buoy data. The SAR results agree well with the buoy observation in the medium H_s part (0.5 m<H_s<3 m for deep water, 0.5 m<H_s<2 m for shallow water). But the SAR results underestimate the H_s value compared to the buoy for high sea state (H_s> 3m for deep water and H_s>2m for shallow water). One possible explanation is that most of the tuning data for the CWAVE algorithm come from medium sea state. Secondly, the buoy H_s measurements in shallow water contain only values up to 4m, while more than 6m are reduced for deep water. This is mainly because the wave can not fully develop in the shallow water due to the on average shorter fetch. Thirdly, SAR results fit better to deep water buoy measurements where the rms error is reduced to 0.58 m compared to 0.65 m for shallow water, and the correlation coefficient rises up to 0.86 for deep water, while it is only 0.69 for shallow water. One possible explanation for the difference is the influence by topography for shallow water.

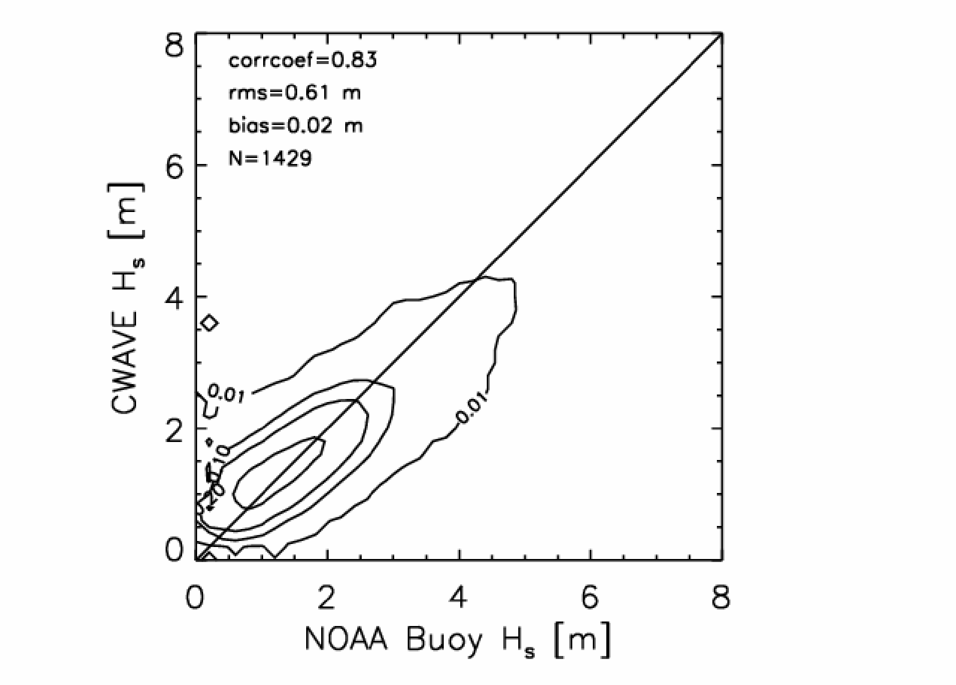

Figure 4.3: Scatter plot with isolines of frequency for CWAVE significant wave height against NOAA buoy significant wave height.

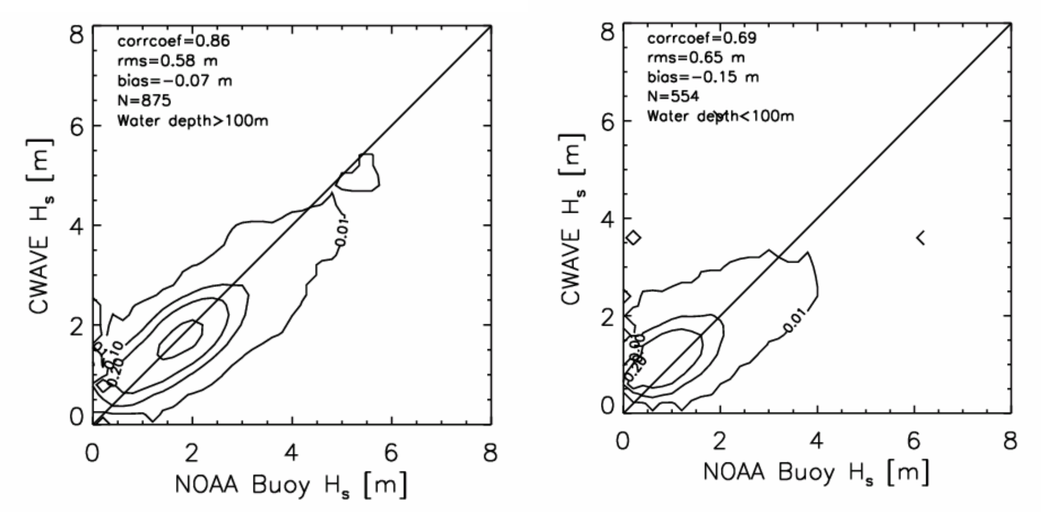

Figure 4.4: Validation of the CWAVE algorithm for significant wave height H_S with NOAA buoy data for deep (left) and shallow (right) water.

Wind speed validation by NOAA buoy

The wind speed retrieval from a SAR wave mode imagette is called CWIND (Song G. et al., 2007). The wind speed from the NOAA buoy was converted into U_{10} before collocating with CWIND results. In this section we carry out a similar comparison between CWIND results and NOAA buoy measurements as between CWAVE results and NOAA buoy measurements using collocated measurement pairs gathered using the same method outlined in section 4.1.1. A typical scatter plot of CWIND-buoy wind speed difference as a function of buoy wind speed is plotted in Fig. 4.5. The total collocated CWIND-buoy measurement is 825 for the period from 1 September 1998 to 30 November 2000 for all 96 NOAA buoys. The mean CWIND wind speed is 0.10 m/s lower than the NOAA buoy wind speed for this CWIND-buoy pairs, and the overall standard deviation of the U_{10} differences is 2.4 m/s. Fig. 4.5 also indicates that CWIND results tend to overestimate U_{10} for low sea state, and underestimate U_{10} for high sea state. This suggests that the CWAVE and CWIND algorithms should perhaps be split into different algorithms for different sea state.

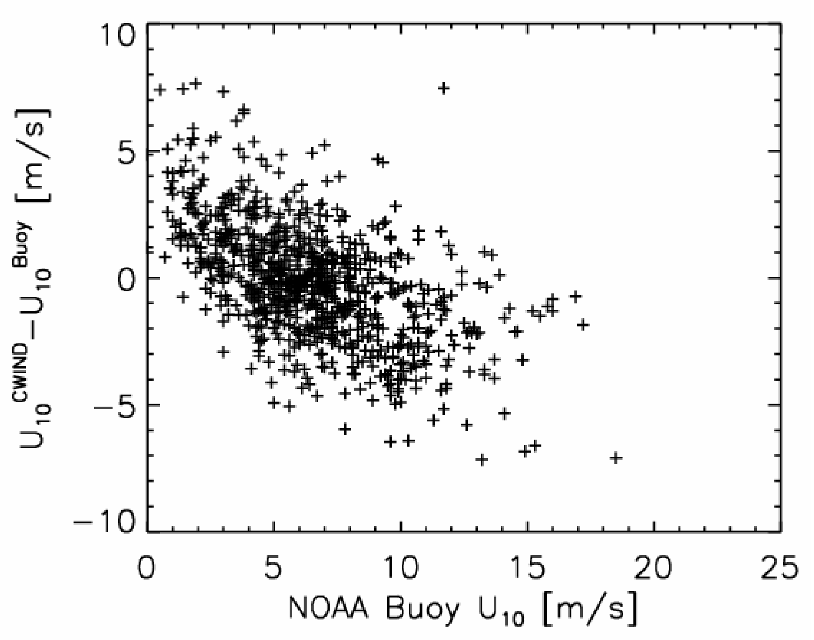

Figure 4.5: Wind speed difference as a function of NOAA buoy wind speed for all 825 collocated CWIND-buoy pairs. Each symbol corresponds to one pair.

The minimum value of $U_{10}^{CWIND}-U_{10}^{Buoy}$ is given by $-U_{10}^{Buoy}$ as discussed above. The data were again binned into 0.97 m/s wide intervals for the buoy wind speed. The standard deviation of the CWIND-buoy difference was then calculated, and the results are plotted in Fig. 4.6 together with the standard deviation on each side of the mean. When the buoy wind speed is lower than 5 m/s, the CWIND wind speed value is larger than NOAA buoy's wind speed, however, when the buoy wind speed is above 5 m/s, the buoy wind speed surmounts CWIND results on average. The last three bins have only one pairs so no standard deviation can be calculated. The largest standard deviation appears in the first bin with 4.36 m/s. For the other bins, except the last three, it is in the range from 1.5 m/s to 2.6 m/s.

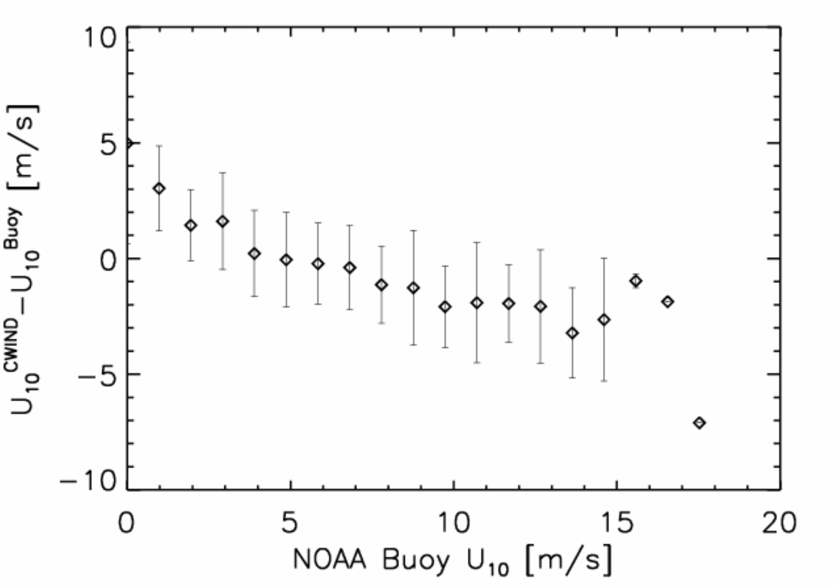

Figure 4.6: The binned wind speed difference as a function of NOAA buoy wind speed, including the standard deviation for each bin.

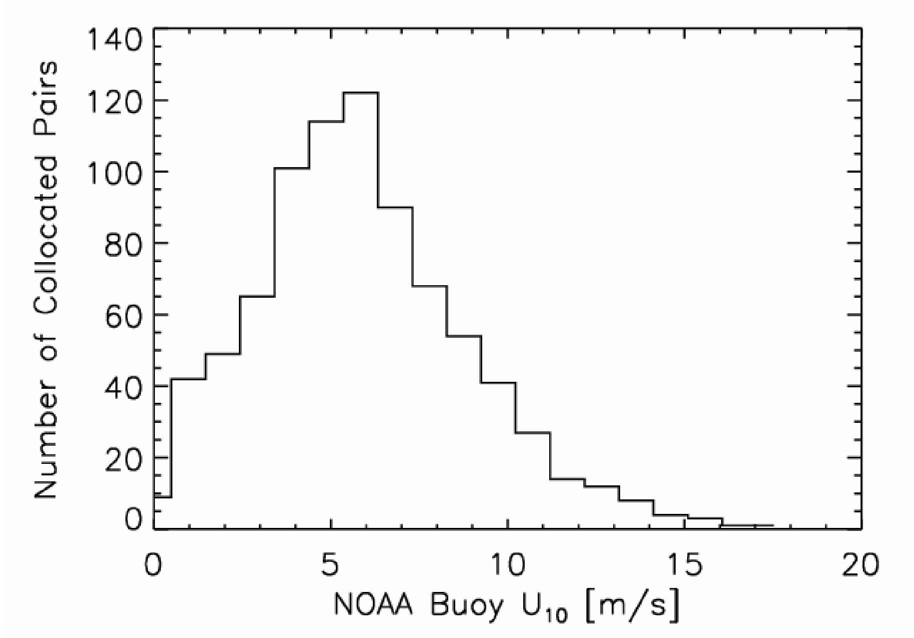

Figure 4.7: Numbers of collocated pairs per 0.91 m/s bin as a function of NOAA buoy wind speed. The distribution is close to a Gaussian.

The frequency distribution of collocated pairs as a function of NOAA buoy wind speed is close to a Gaussian distribution (Fig. 4.7). The maximum number of pairs is located in the seventh bin (5.84 m/s) with 122 collocated pairs. The RMS error (Fig. 4.8) for CWIND and NOAA buoy data is 2.4 m/s which is larger than the one found for other satellite instruments' wind speed retrievals. For example, Dobson et al. (1987) gave an RMS error of 1.8 m/s for the altimeter wind speed; Krasnopolsky et al. (2000), using a neural network multiparameter algorithm for SSM/I ocean wind speed retrieval, found 1.7 m/s. Fetterer et al. (1998) estimated wind speed from SAR image based on a C band scatterometer algorithm and found 1.1 m/s. The correlation coefficient between CWIND and buoy measurements is 0.67 for the 825 collocated pairs during the full two years data set used in this study. This is also lower than for the other results just mentioned. Thus the CWIND errors seem too high for operational use. Further improvement by taking additionally the CMOD algorithm into account could be achieved.

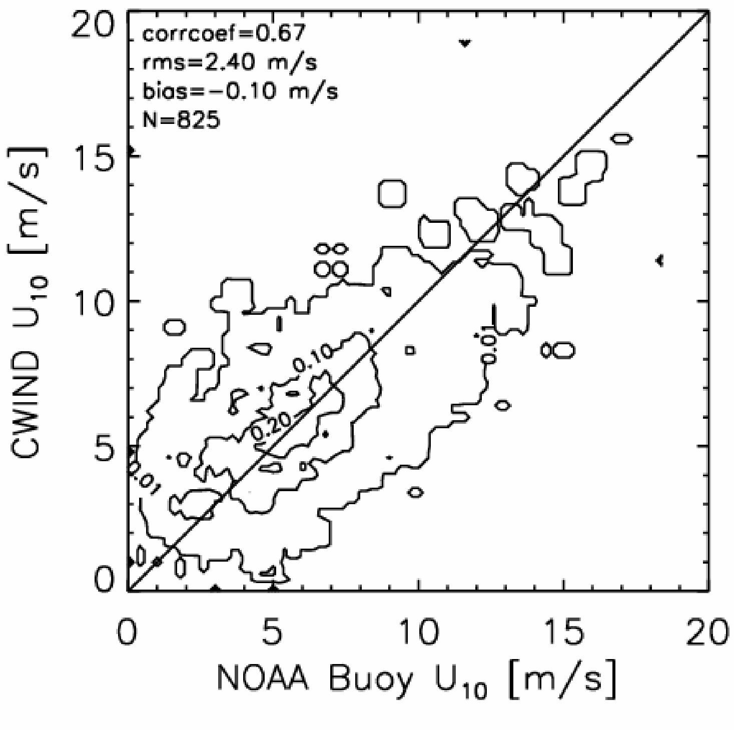

Figure 4.8: Scatter plot for CWIND wind speed versus NOAA buoy wind speed. The isolines represent the percentage of points out of each circle for example 0.2 represents 20% of points lie out of this isoline.

In order to investigate whether the water depth has an effect on the CWIND retrieval quality, the scatter plots of CWIND wind speed U_{10} versus NOAA buoy wind speed were separated into deep and shallow water cases as given in Fig. 4.9. No substantial differences were found from the statistical analysis between the deep water and shallow water results. The correlation coefficient is 0.68 for deep water, and 0.64 for shallow water. The RMS error is 2.28 m/s for deep water, and 2.24 m/s for shallow water. The bias is -0.20 m/s for deep water, and -0.11 m for shallow water. Therefore the water depth has no strong impact on the CWIND retrieval results.

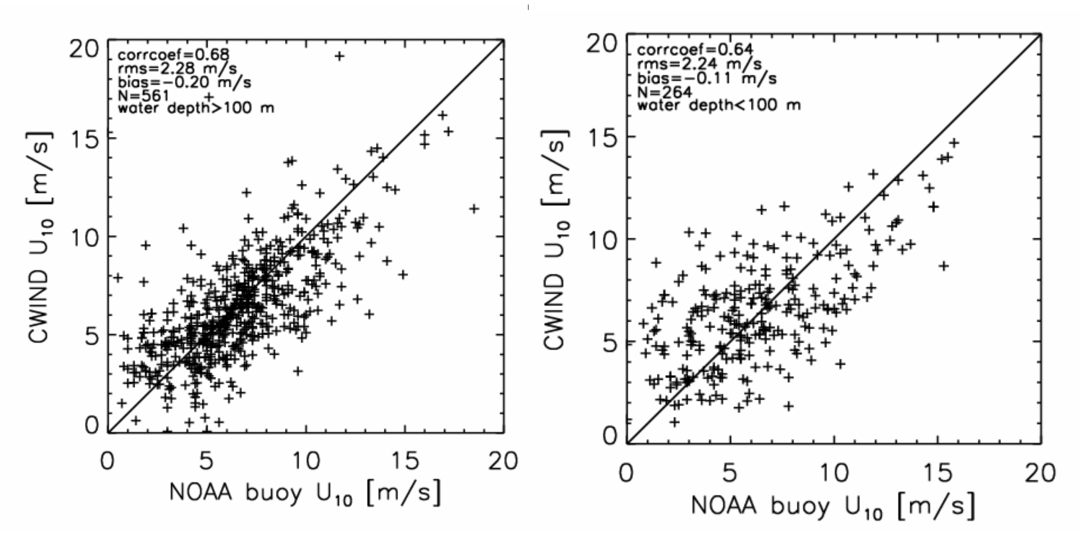

Figure 4.9: Validation of CWIND wind speed U_{10} by NOAA buoy data for deep (left) and shallow (right) water.

After the statistical quality analysis of SAR results (H_s and U_{10}) by comparison to buoy measurements, one should also pay attention to the different observing mechanisms leading to sampling errors. In many previous studies, the buoy observations have been assumed to be the “true” results, and all errors have been assigned to the remotely sensed results. This is obviously not correct since buoys and satellites measure two different quantities. Buoys measure the time average of atmopheric and oceanic parameters over a short time at a single point such as typically for less than 10 minutes for wind speed, while satellites make a nearly instantaneous measurement averaged over over the spatial footprint of the satellite. So it is in some sense “unfair” to assign all the differences between satellites and buoy measurements to errors of the satellite measurement. With this view, part of the standard deviation of the difference between buoy and satellite measurements can be assigned to sampling errors in the buoy estimate of parameters. The error of the satellite measurement inferred from the buoy-satellite difference is thus smaller than shown.

Another point also needs to be mentioned: most of the buoys used in this study are located in coastal areas. As we know that many satellite products such as scatterometer wind vector, altimeter wind and wave product do not perform well near shore. The high RMS error between SAR results and buoy observations may be partly due to reduced performance of the empirical algorithm CWAVE and CWIND near to the coast.

4.2 Validation of CWAVE with Polarstern Vessel Data

The purpose of this section is first to explain how CWAVE is validated by the Polarstern vessel data, and second to discuss the results of the comparison.

4.2.1 Method

Aboard the research vessel Polarstern wave height H is observed visually and instantaneously by a trained weather observer following an international standard called FM 13. In fact, the observer records estimated height of wind wave or directly measured wave height following a code in 1/2 meter steps (e.g. 01 = 0.5m, 02 = 1.0m, etc.). This value can be converted into significant wave height using the empirical relationship of Toba (1972) between significant wave height H_s and observed wave height H as follows:

$$H_S = 1.6H \tag{4.6}$$

Polarstern measures wind speed at a height of 39 m above the waterline as mentioned in section 2.2.2, so the wind speed also needs to be converted into U_{10} using Eq. (4.1). Then the significant wave height and wind speed observed by Polarstern vessel are compared to CWAVE and CWIND results. There are two possible methods of comparison. Taylor (1986) suggested that averages of vessel and satellite data should be compared. In order to do this there must be enough data to define an unbiased climatology for the region and period of the average from both the vessels and the satellite. However, in this study there is not enough data to do this. The other method is a point by point comparison of nearly coincident pairs of satellite and in-situ observations. This is the approach attempted in this study.

SAR results and Polarstern observations are collocated in space and time as follows: First, the coincident points between SAR imagettes and Polarstern observations are found. As we know Polarstern observations at fixed times, usually 00, 03, 06, 09, 12, 15, 18 and 21 UTC, 1.5 hours are used as a criterion for the maximum temporal difference. Second, the allowed difference in space has to be determined. Whenever the distance between the center of a SAR imagette and Polarstern position is less than 300 km the collocated pair is accepted. After these two steps, 188 pairs for significant wave height and 241 matched pairs for wind speed are found.

4.2.2 Results and Discussion

Significant Wave Height Validation by Polarstern Observations

In this section CWAVE H_s results are validated by Polarstern vessel observations. In order to analyze the H_s difference between them, Fig. 4.10 was plotted. Fig. 4.10 reveals the same tendency as Fig. 4.1 that CWAVE tends to overestimate the H_s value in low sea state ($H_s < 2$ m) and to underestimate the value in high sea state ($H_s > 5$ m). The mean CWAVE H_s is 0.39 m lower than the Polarstern H_s for this CWAVE-Polarstern pair.

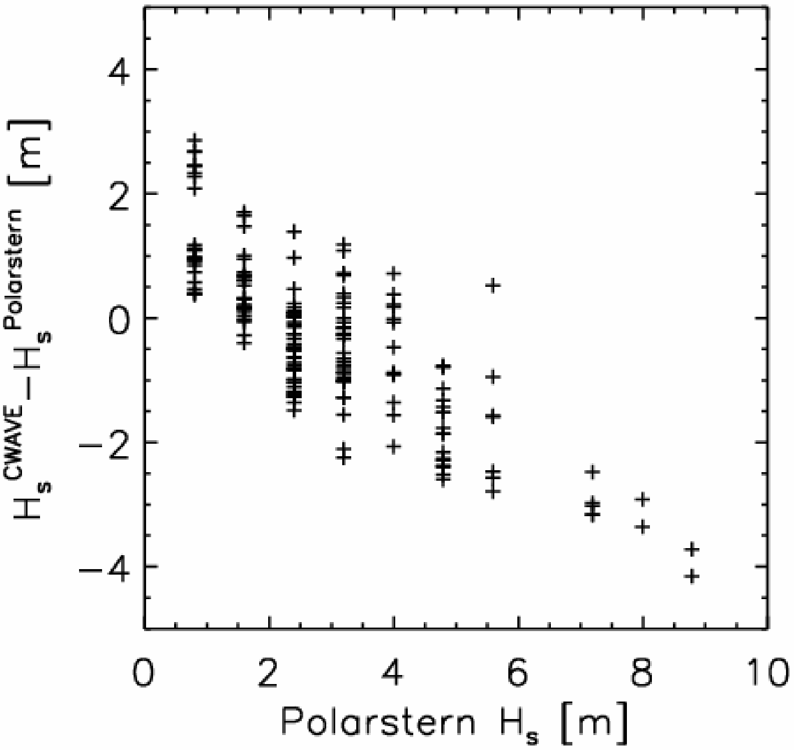

Figure 4.10: H_s differences as a function of Polarstern H_s for all collocated CWAVE-Polarstern pairs. Each symbol corresponds to one CWAVE-Polarstern pair.

Both the CWAVE and the Polarstern significant wave height should be reported to be positive. Since the minimum value of the CWAVE significant wave height is zero, the minimum value of $H_S^{CWAVE} - H_S^{Polarstern}$ is given by $-H_S^{Polarstern}$. The data were binned into 1 m wide intervals using H_s from Polarstern. The standard deviation of the CWAVE-Polarstern difference was then calculated, and the results are plotted in Fig. 4.11 (left) including the standard deviation on each side of the mean. The maximum number of pairs is located in the first bin (0.79 m) which has 55 collocated pairs which can also be seen from Fig. 4.11 (right). The fifth bin contributes the largest standard deviation with 1.15 m. The standard deviation of other bins is less than 1 m. The accumulation of the collocated pairs at small values of H_s indicates that the Polarstern vessel observed only few storms.

The scatter plot in Fig. 4.12 leads to a correlation of only 0.64 which is much smaller than for the NOAA buoys. Hence, both the bias (-0.39 m) and RMS error (1.35 m) are higher than for the intercomparison with buoys.

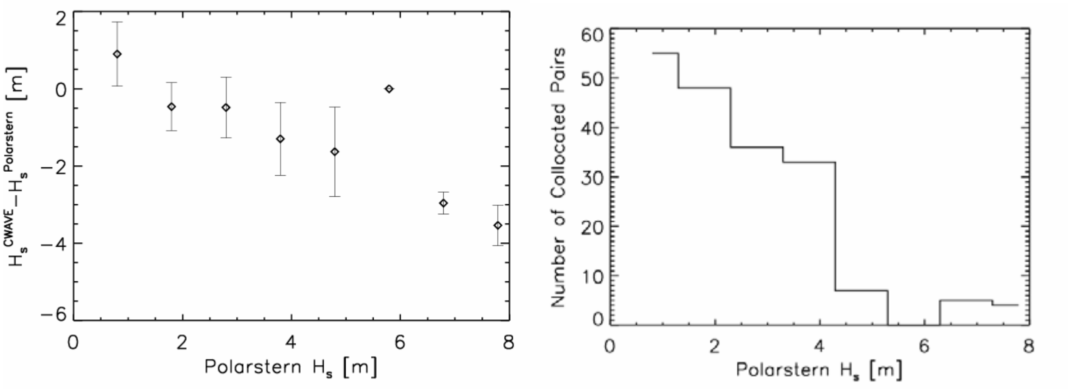

Figure 4.11: Significant wave height difference as a function of H_s measured by Polarstern for bins of 0.79 m size (left) and number of collocated pairs as a function of H_s (right).

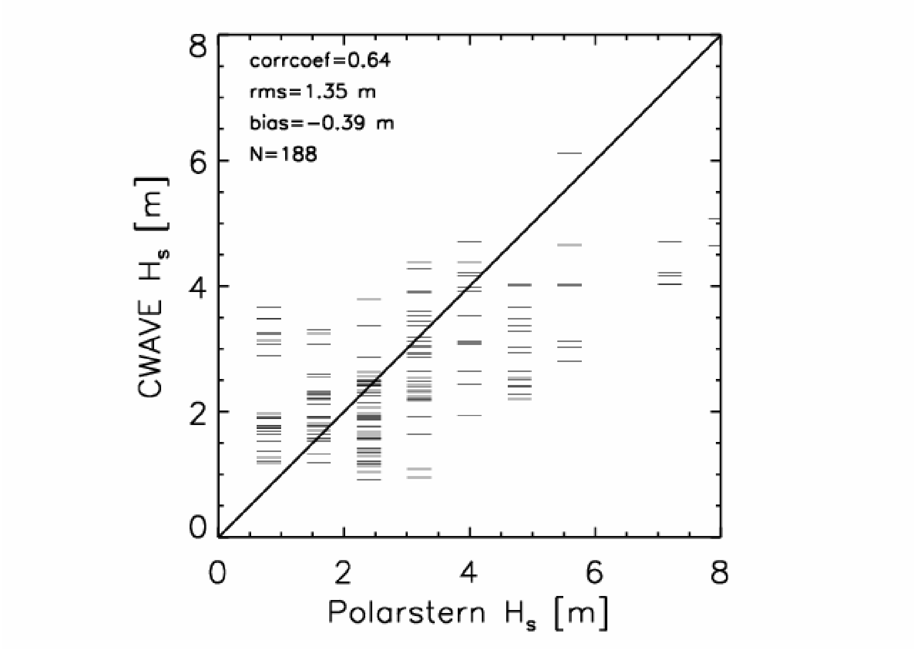

Figure 4.12: Validation of the CWAVE algorithm with observations from the research vessel Polarstern.

The comparably poor quality of the validation of the CWAVE H_s by Polarstern observations might have two major reasons. One reason is the small number of cases which might be too less for a meaningful comparison. Some previous studies (Kent et al., 1998; Taylor, 1986 and 1994) comparing ERS-1 scatterometer data with ship observations examined more collocated data as both more ship observations and longer time periods were available. Thus the high RMS error is partly caused by the small and unrepresentative sample. Another reason is the spatial separation of the observations which might be too high in the present case. The optimum separation would include as much as data as possible without increasing the RMS difference between the vessel and satellite data. However, 300 km had to be selected as spatial separation in order to find as much collocated pairs as possible. This large separation may not be the optimum, thus leading to a rather high RMS error.

Wind Speed Validation by Polarstern Observations

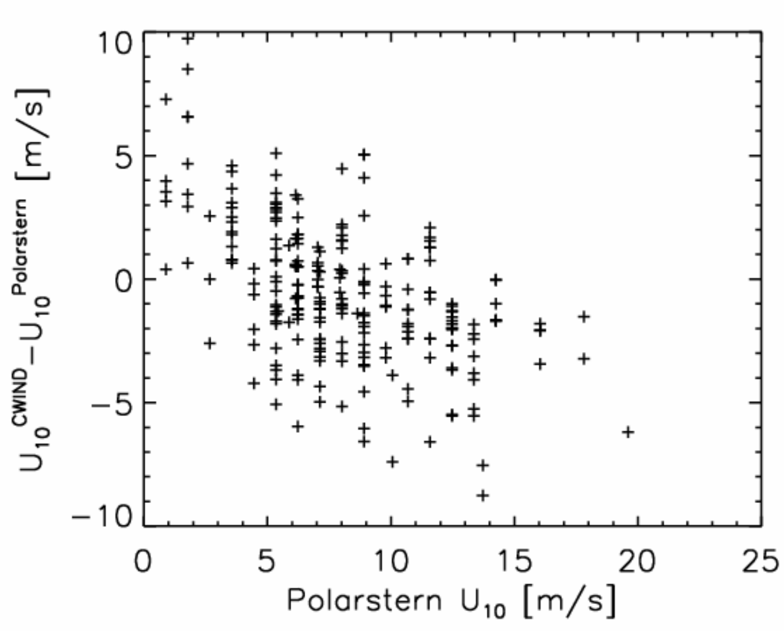

Figure 4.13: $U_{10}^{CWIND} - U_{10}^{Polarstern}$ as a function of Polarstern U_{10} for all collocated CWIND-Polarstern pairs. Each symbol corresponds to one CWIND-Polarstern collocated measurement.

Fig. 4.13 is a similar plot between CWIND U_{10} and Polarstern U_{10} as Fig. 4.10. For CWIND comparison to Polarstern, the mean CWIND wind speed is 7.43 m/s, and the mean Polarstern wind speed is 8.17 m/s, so the bias is 0.74 m/s. Note that while the bias of 0.74 m/s is not big, however the standard deviation of 3.19 m/s (Fig. 4.14 (left)) is quite large and well above the previous comparison between CWIND and NOAA buoys. The data were also binned into intervals of 0.89 m/s size of the Polarstern U_{10} values (see Fig. 4.14). The maximum number of pairs is located in the fifth bin (4.78 m/s) which has 31 collocated pairs.

The scatter plot of CWIND values versus Polarstern observations (Fig. 4.15) leads to a correlation coefficient of 0.62, much lower than compared to buoys. Also, both the bias (-0.74 m/s) and RMS error (3.19 m/s) are much higher than for the buoys. The reasons for the rather poor quality of the validation of CWIND values by Polarstern observations are similar to the ones given for the CWAVE and Polarstern H_s comparison.

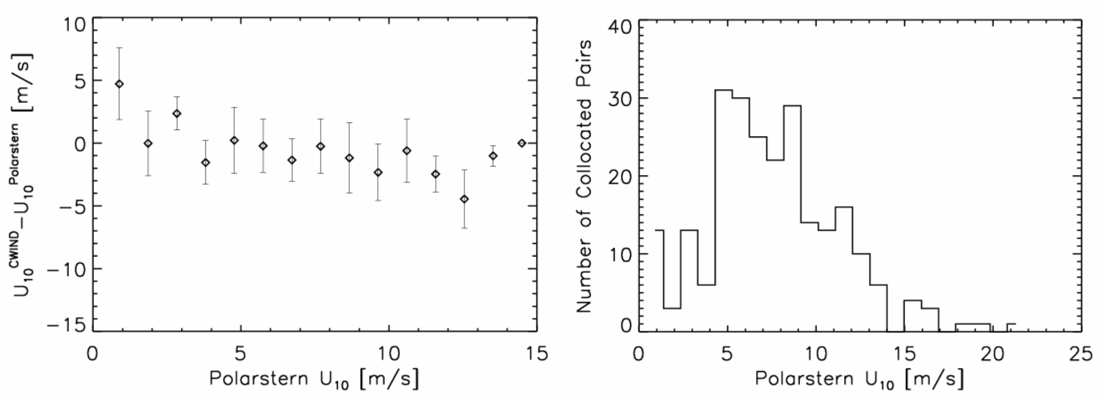

Figure 4.14: Average U_{10} difference as a function of Polarstern U_{10} for bin of 0.79 m/s size including standard deviation (left) and numbers of collocated pairs as a function of Polarstern H_s (right).

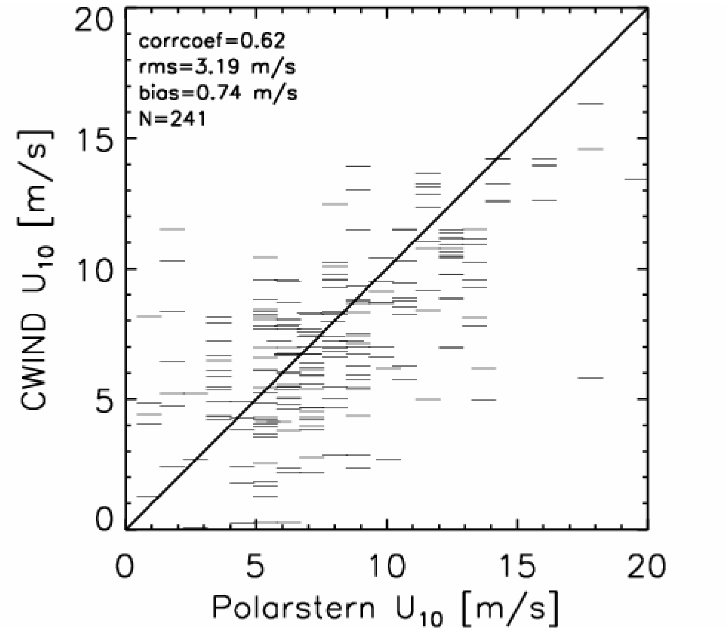

Figure 4.15: Scatter plot for U_{10} from the CWIND algorithm and from observations onboard the research vessel Polarstern.

4.3 Comparison of SAR Results with Other Satellite Data

In this section the SAR results are compared to other satellite products such as significant wave height from altimeters, wind speed from HOAPS, and wind speed from the ERS-2 scatterometer.

4.3.1 Comparison of CWAVE H_s with H_s from the ERS-2 Altimeter

The altimeter on ERS-2 is operating jointly with the SAR. Hence, it observes nearly simultaneously the ocean surface under a different look direction. In the following, the significant wave height H_s from SAR and the Radar Altimeter (RA) are compared. First, the collocation method is introduced, and then the comparisons are discussed.

Collocation Method

The significant wave height H_s derived with the CWAVE algorithm is compared the ERS-2 altimeter results only for 1999. A set of measurements collocated both in time and space must be generated for this comparison. The radar altimeter instrument emits a pulse every second, corresponding to approximately a 7 km resolution in nadir along the satellite track. However, the SAR instrument can acquire one wave mode imagette only every about 30 seconds, corresponding to a 200 km resolution along the satellite track. As the SAR is looking to the right of the track, there is at least an offset of about 300 km between SAR and altimeter measurements of the ERS-2 saellite. Therefore, we can only find collocated pairs between SAR and altimeter measurements with about 300 km distance but within 1 second.

Results and Discussion

24,413 pairs were found between CWAVE and altimeter during 1999 using the collocation method just described. It is important to note that the CWAVE measurements for H_s<1 m were excluded from this comparison due to reasons explained later. The density scatter plot (Fig. 4.16) leads to a RMS error of 0.56 m and a correlation coefficient of 0.83. The mean CWAVE H_s is only 0.08 m lower than the altimeter H_s. The RMS error of 0.56 m is higher than for comparisons of altimeter data to in-situ observations found in the literature. Gower (1996) reported a RMS error for H_s of 0.35 m for the TOPEX/POSEIDON altimeter when comparing to moored buoys deployed in the Pacific Ocean. Kshatriya et al. (2001) showed that a RMS error as small as ± 0.3 m is possible, when comparing H_s from TOPEX/POSEIDON altimeter with in situ observations aboard buoys in the North Indian Ocean.

Fig. 4.17(b) shows that the H_s difference of most of CWAVE-altimeter pairs is within 1 m. Both Fig. 4.16 and Fig. 4.17(a) indicate that for low sea state CWAVE overestimates H_s, and underestimate it in high sea states. This dependence on sea state is in line with the previous validations of CWAVE using NOAA buoy data and Polarstern vessel data.

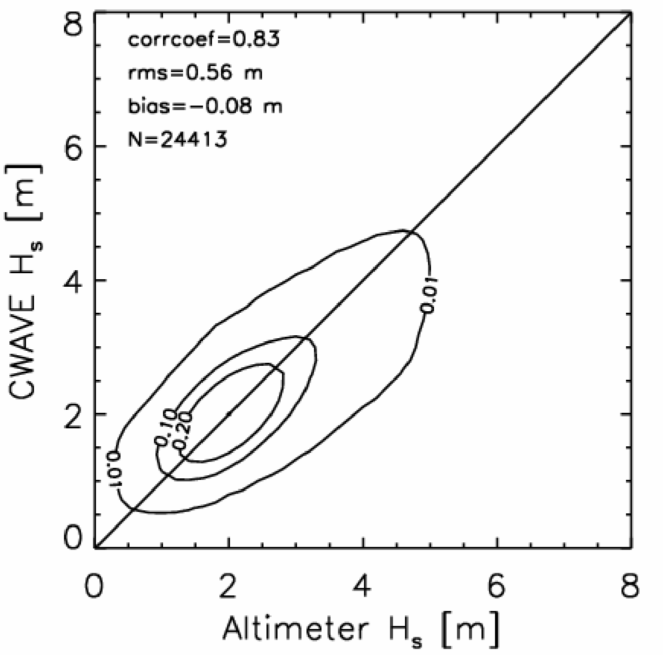

Figure 4.16: Scatter plot of H$_s$ derived from SAR and the altimeter on board ERS-2.

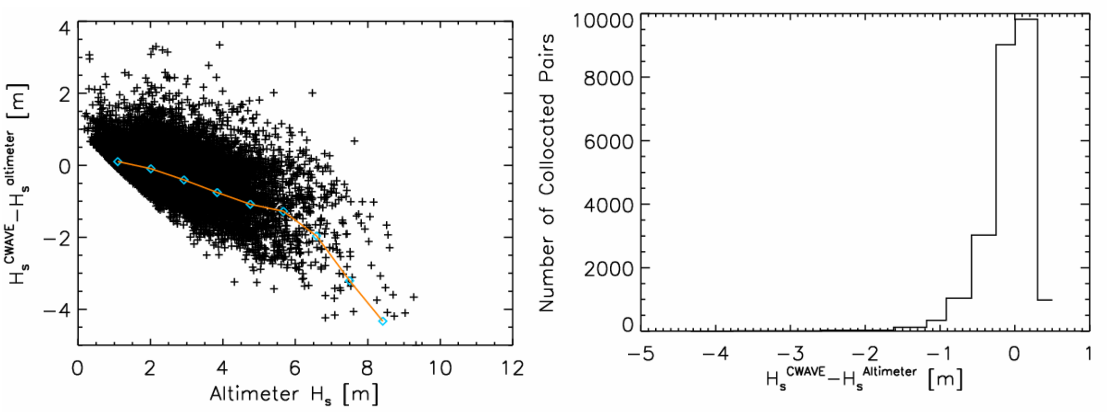

(a) (b)

Figure 4.17: (a) H$_s$ difference as a function of altimeter H$_s$ for all collocated CWAVE-altimeter pairs. Each symbol corresponds to one CWAVE-altimeter pair; (b) Number of collocated pairs as a function of H$_s$ defference between CWAVE and Altimeter.

The standard deviation and the mean difference amount in bins of 0.9 m size are analysed in Fig. 4.18. The largest standard deviation with 1.09 m in the seventh bin whose mean is 5.67 m. The standard deviation distribution is regular and shows no big change due to the large quantity of matched pairs found for each bin. The largest number of CWAVE-altimeter matched pairs is 6384 at H$_s$=2.11 m (Fig. 4.18b). Most collocated pairs lie in the altimeter H$_s$ range from 1.1 m to 3.1 m.

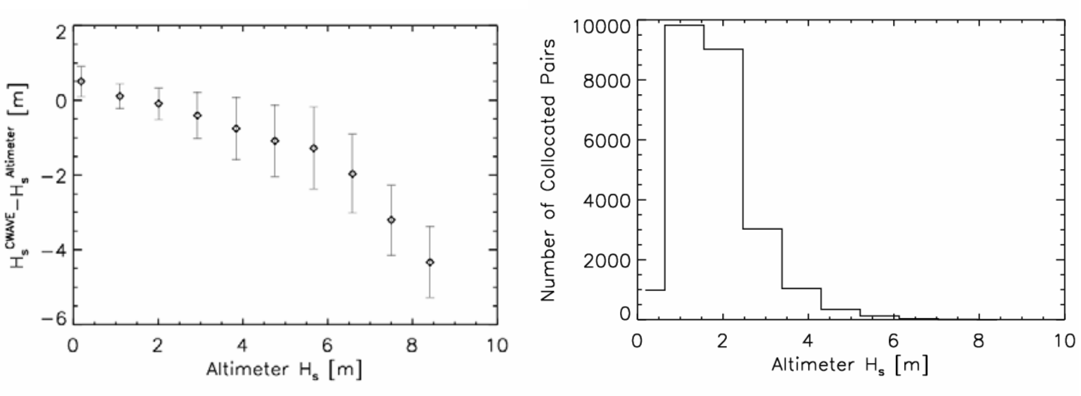

(a) (b)

Figure 4.18: (a) The binned mean H_s difference as a function of altimeter H_s including the standard deviation; Frequency distribution of H_s in 0.9 m bins for the CWAVE and altimeter matched pairs as a function of altimeter $H_{s.}$

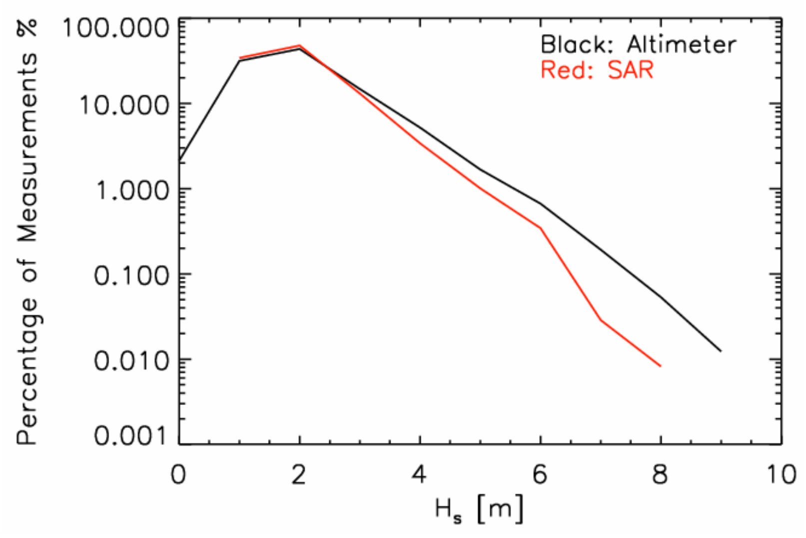

Figure 4.19: Frequency distribution of the percentage of significant wave height in 1m intervals for CWAVE and altimeter in 1999; for SAR (red) distribution and altimeter (black).

In order to further investigate the H_s distributions of CWAVE and altimeter, Fig. 4.19 is plotted. The distribution comparison between CWAVE and altimeter shows a good overall agreement. The profile of the distribution of both CWAVE and altimeter is similar to a Rayleigh distribution. Both CWAVE and altimeter reach a peak at 2 m, however, the peak of CWAVE is somewhat higher than that of the altimeter. For H_s from 3 m to 6 m the results is opposite. This again indicates that high waves tend to be underestimated by the CWAVE algorithm. One reason for CWAVE underestimating high wave is possibly due to the sampling used when developing the CWAVE algorithm. Most of the images selected for developing the algorithm were located in the northern hemisphere, and only a few images were selected from a high wave region like the Antarctic Circumpolar Current. The CWAVE algorithm could probably be improved by selection of more representive image distribution all over the world.

4.3.2 Comparison Wind Speed from SAR and HOAPS

The HOAPS-S wind speed data set from the current HOAPS-II version is used for the comparisons with wind speed from CWIND both on a daily and a climatological basis. Fig. 4.20 shows one example of a daily comparison at 24:00 on 17 September 1998. The background of the map is the wind speed from HOAPS, in which land, ice, rain and calibration issues contaminated pixels are plotted in white. The superimposed small squares contain the wind speed from CWIND results. Black and white frames, respectively, represent homogeneous and inhomogeneous SAR images. Most of the CWIND results are consistent with the HOAPS wind speed. There is one track of SAR exactly passing across a strong storm in the North Pacific. Both CWIND and HOAPS values show a storm of the order 18 m/s.

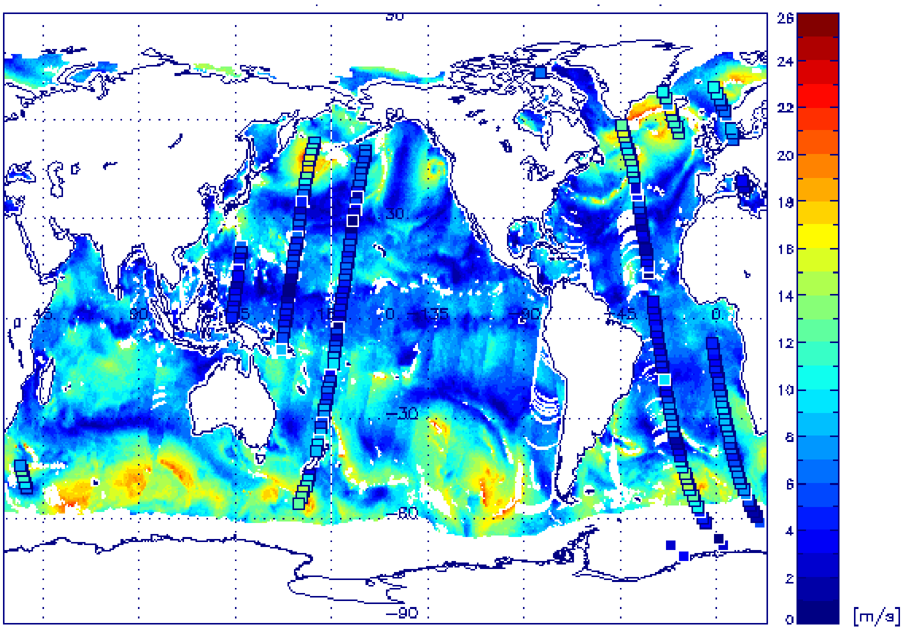

Figure 4.20: Wind speed map as derived from SSM/I in the HOAPS atlas (background) with superimposed CWIND SAR (square) wind speed values around 24:00 hours on September 17th 1998.

This section is structured as following: the comparison method between CWIND SAR wind speed retrievals and HOAPS wind speed is described; afterwards the results are presented and discussed.

Method

A similar method is used between CWIND and HOAPS to find collocated measurements as used before. The HOAPS pixel is 0.25° × 0.25° and given twice a day at 12:00 (noon) and 24:00 (midnight). First we check to see if a valid HOAPS observation is spatially collocated with the CWIND observation. We imagine a square box, 0.125 degree on a side, centred at the SAR image centre. If the box is totally within one HOAPS pixel, the value of the wind speed from that pixel is used. If the SAR image is exactly at the edge of the pixel, an average of two HOAPS pixels is taken. To finish producing a collocated observation we must find a CWIND measurement that occurs roughly at the same time as the HOAPS. In this study, a temporal window of 3 hours was used as criterion.

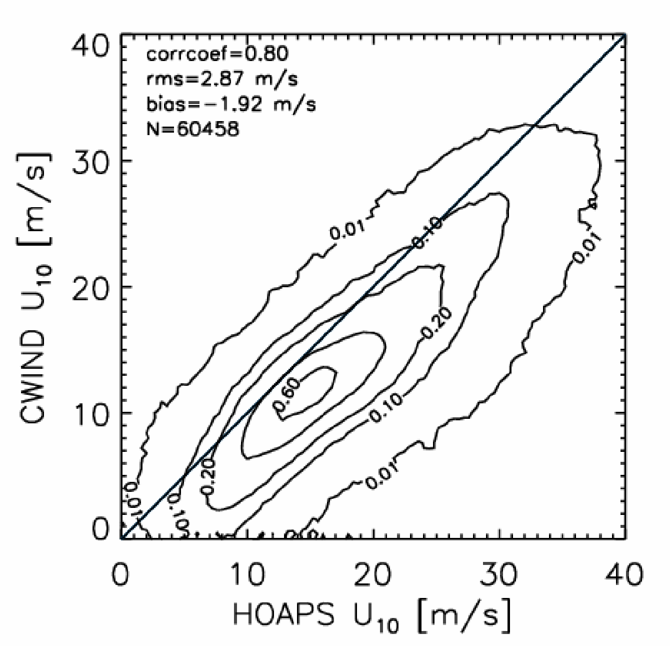

Figure 4.21: Scatter plot of CWIND versus HOAPS wind speed. The correlation coefficient is 0.80 and the RMS error reaches 2.87 m/s

Results and Discussions

The matched pairs of CWIND and HOAPS for the period September 1998 to November 2000 amount to 60458 using the collocation method described above. The density scatter plot (Fig. 4.21) shows a RMS error of 2.87 m/s with a correlation coefficient of 0.80. The bias is with -1.92 m/s rather high. The RMS error of 2.87 m/s is higher than the RMS errors between wind speed from HOAPS and other observations found in the literature. For example, Winterfeldt et al. (2008) found 2 m/s for all collocated HOAPS and in-situ wind speed from 12 stations. The large bias and RMS error indicate that the CWIND algorithm underestimates the wind speed in most cases compared to HOAPS observations.

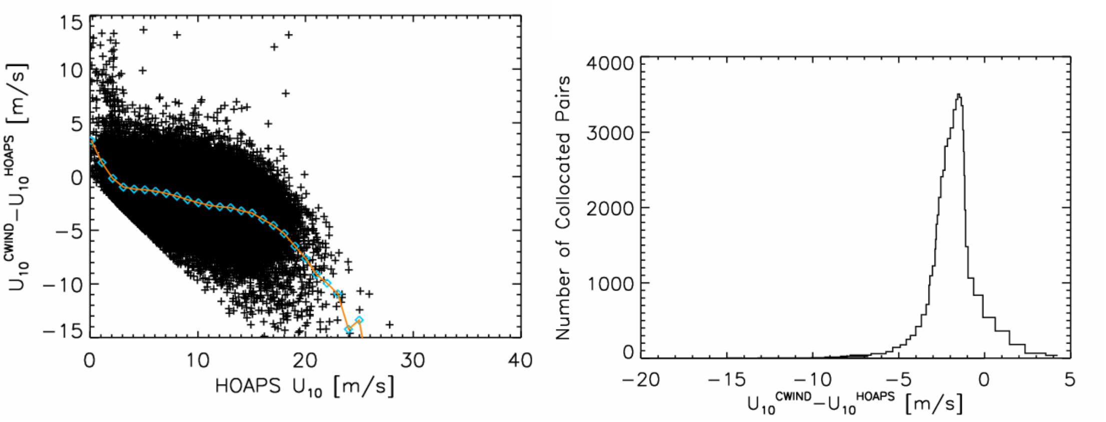

(a) (b)

Figure 4.22: U_{10} differences as a function of HOAPS U_{10} for all collocated CWIND-HOAPS pairs. Each symbol corresponds to one CWIND-HOAPS collocated measurement. The red line is the U_{10} difference as a function of HOAPS U_{10}; (b) number of collocated pairs per bin as a function of wind speed difference between CWIND and HOAPS.

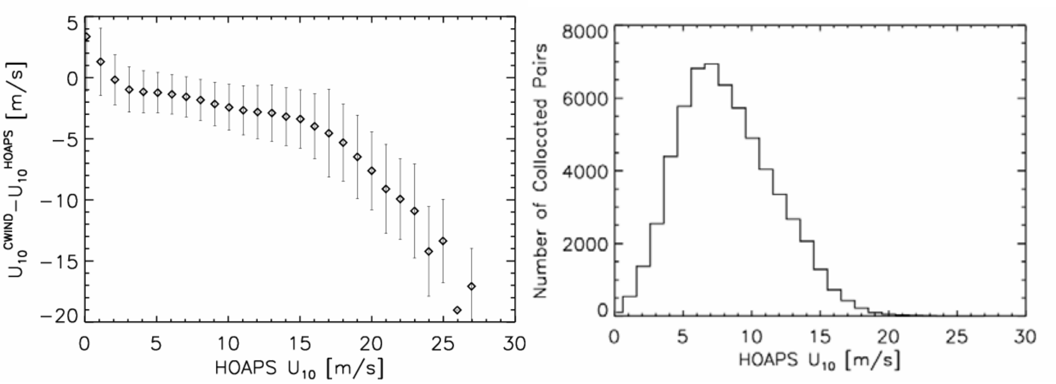

(a) (b)

Figure 4.23: (a) The binned mean U_{10} difference as a function of HOAPS U_{10}, including one standard deviation; (b) Frequency distribution of U_{10} per 1 m/s bin for CWIND and HOAPS as a function of HOAPS U_{10}.

Fig. 4.22(b) shows that the U_{10} difference of most CWIND-HOAPS pairs ranges from -5 to 0 m/s. Both Fig. 4.21 and Fig. 4.22 (a) indicate that the CWIND algorithm on average underestimates the U_{10} value. This needs further investigation of the CWIND algorithm.

The distribution of differences and standard deviation in every bin are further analysed in Fig. 4.23. The collocated pairs were binned into intervals 1 m/s wide using the HOAPS U_{10}. The largest standard deviation, whose value is 4.45 m/s, lies in the first bin at 0.10 m/s. The standard deviation distribution is smooth due to the large quantity of matched pairs. The largest number of matched pairs is 6937 at 7.07 m/s of the HOAPS U_{10} value (Fig. 4.23b). Most pairs lie in the HOAPS U_{10} range from 5 m/s to 10 m/s, medium sea state and they are also compared well in this range (Fig. 4.23(a)).

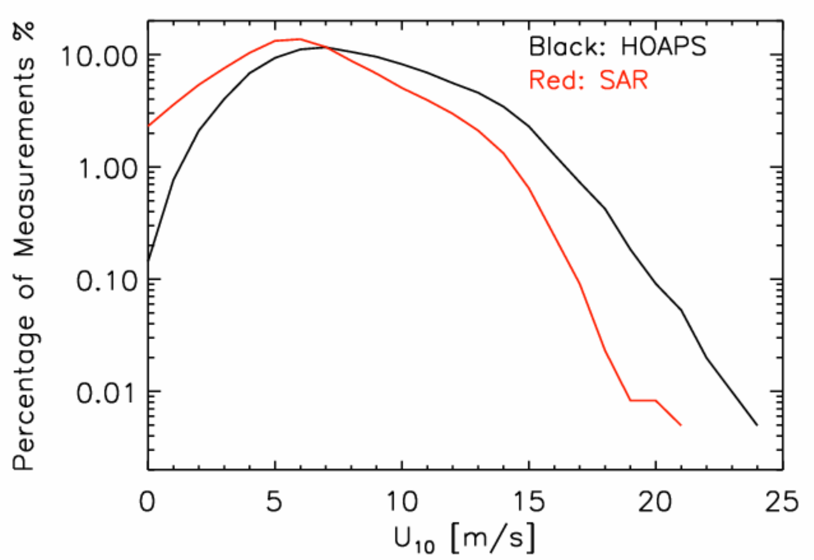

Figure 4.24: Percentage of wind speed per 1m/s interval for CWIND (red) and HOAPS (black).

With Fig. 4.24 we can further investigate U_{10} distributions. The distribution comparison between CWIND and HOAPS does not show good overall agreement. CWIND and HOAPS reach their peaks at 6 m/s and 7 m/s, respectively and the peak of CWIND is higher. For U_{10}>7 m/s, the percentage of CWIND measurements is increasingly below the HOAPS curve. One reason for CWIND underestimating high wave is possibly due to the sampling when developing the CWIND algorithm, which is the same as for CWAVE. Another reason, maybe, is due to the inhomogeneity test used currently, which needs further improvement.

On the other hand also HOAPS could overestimate wind speed. In order to investigate such a possibility, Fig. 4.25 was plotted using the collocation criteria described above. The correlation coefficient between buoy and HOAPS wind speed is only 0.71 and the RMS error reaches 2.82 m/s with a bias of -1.00 m/s. These statistical results seem to indicate that the HOAPS wind speed results tend to overestimate the wind speed value at NOAA buoy locations near the coast. This result is in agreement with the findings of Meissner et al. (2001). They showed that the mean biases between the wind speed derived from SSM/I F11 and F13 and wind speed from the forecasted NRA_R1 are 0.5 m/s. As both F11 and F13 are incorporated in the HOAPS product and F11 is the reference satellite used for the SSM/I intercalibration, part of the bias can arise from HOAPS.

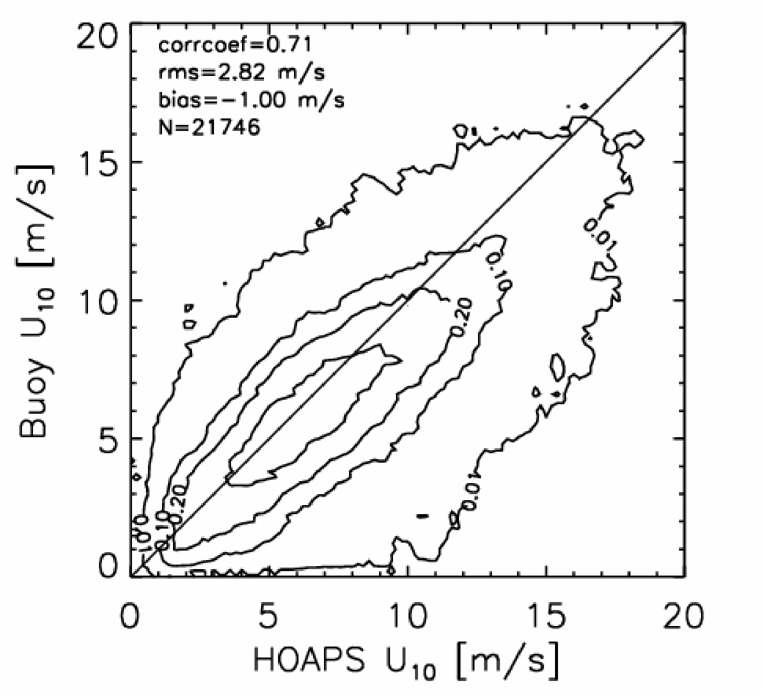

Figure 4.25: Scatter plot of NOAA buoy wind speed against HOAPS wind speed. The correlation coefficient between them is 0.71, RMS error is 2.82 m/s.

4.3.3 Comparison of Wind Speed from SAR and Scatterometer

In this section the CWIND U_{10} measurements are compared to scatterometer results. First the collocation method is described before the results are presented and discussed.

Method

The collocation procedure is similar to the one between SAR images and altimeter data because both the scatterometer and the SAR are operated on ERS-2. The SAR in image mode and Scatterometer can not be operated in parallel due to insufficient power. Only the SAR in wave mode imagette can be interleaved with the scatterometer. Hence it is easy to find matched pairs between CWIND SAR wave imagettes and scatterometer in temporal range. The main problem is to find the collocated pixel in spatial range. Because the spatial resolution of ERS-2 scatterometer is around 50 km, we set a spatial window of 50 km to find the appropriate scatterometer pixel.

Results and Discussions

114,052 matched pairs between CWIND and scatterometer were found for the period from 1 September 1998 to 30 November 2000. The statistical density scatter plot of CWIND wind speed versus scatterometer wind speed is depicted in Fig. 4.26 (a). The bin size is 0.2 m/s in each coordinate. The contours are in relation to total observations (1 means 100%). The correlation coefficient between CWIND wind speed and scatterometer retrievals is 0.84. The RMS error is 1.77 m/s and the bias is -0.23 m, an improvement compared to Birgitte et al. (1999) who found 2 m/s and 0.5 m/s.

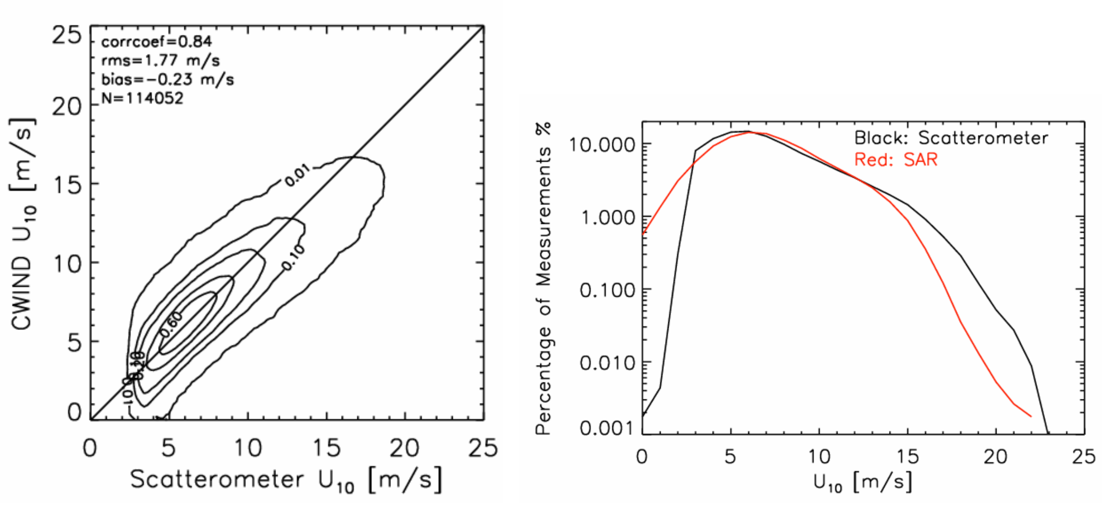

(a) (b)

Figure 4.26: (a) Scatter plot of CWIND wind speed versus scatterometer wind speed, leading to a correlation coefficient of 0.84, a RMS error of 1.77 m/s and a bias of -0.23 m; (b) Frequency distribution of wind speed in 1m/s intervals for CWIND (red) and scatterometer (black).

Fig. 4.26(b) shows the frequency distribution of wind speed in 1m/s intervals for CWIND (red) and scatterometer (black). Both distributions show an overall agreement from $3<U_{10}<15$ m/s. However, an unrealistic cutoff appears at 3 m/s in the scatterometer distribution, which can also be seen from Fig. 26(a). At the same time the frequency at $U_{10}>3$ m/s is higher than in the case of SAR data. This suggests that some wind speed observation < 3 m/s are assigned to higher wind speed. This is consistent with reports in the literature. For example, Stoffelen and Anderson (1992) pointed out that the scatterometer wind speeds are less accurate at low incidence angles, especially at low wind speed. The IFREMER product (Quilfen, 1995) further accepts that there is very little skill in wind speed detection at low wind speed and does not produce vectors for wind speeds below about 3 m/s.

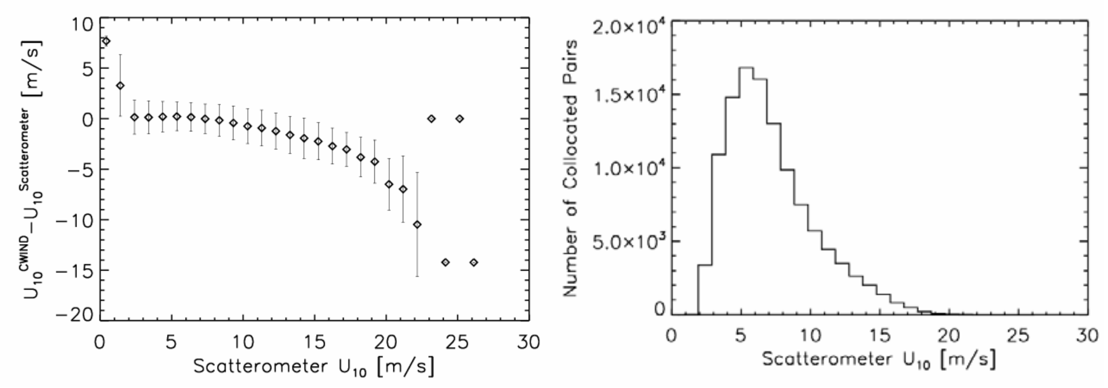

(a) (b)

Figure 4.27: (a) The binned mean U_{10} difference as a function of scatterometer U_{10} for a 1 m/s interval, including standard deviation; (b) Frequency distribution of U_{10} in 1 m/s bins for CWIND and scatterometer matched pairs as a function of scatterometer U_{10}.

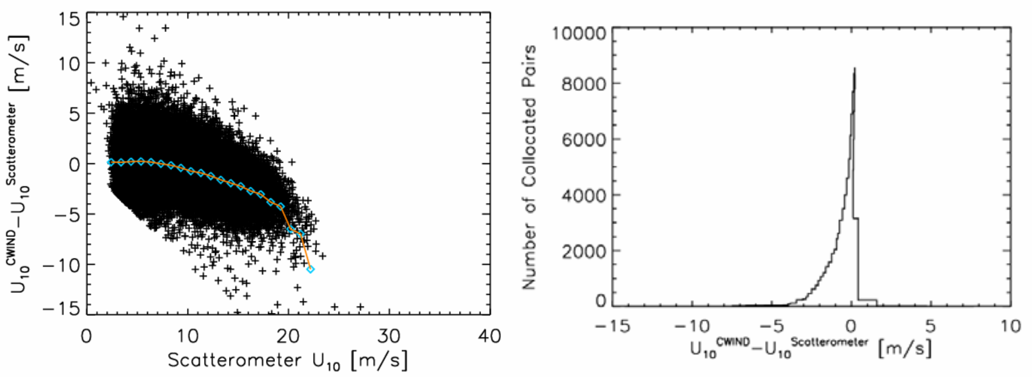

(a) (b)

Figure 4.28: (a) U_{10} difference as a function of scatterometer U_{10} for all collocated CWIND-scatterometer pairs. Each symbol corresponds to one CWIND-scatterometer collocated measurement. The orange line is the U_{10} difference as a function of scatterometer U_{10}.; (b) Number of collocated pairs as a function of the difference between CWIND and scatterometer in 0.5 m/s intervals.

The standand deviation distribution as a function of scatterometer wind speed in 1 m/s intervals are plotted in Fig. 4.27(a). In Fig. 4.27 (b), the frequency of matched pair, is plotted as a function of the U_{10} difference. Here we observe only few collocated pairs for U_{10} below 2 m/s or above 22 m/s. When there are enough matched pairs (2 m/s <scatterometer wind speed < 22 m/s), the standard deviation is regularly growing from 1.40 m/s to 2.4 m/s. For medium sea state (2 m/s < U_{10}< 15 m/s) the mean wind speed difference between CWIND and scatterometer is small. Fig 4.28 (b) also shows that the maximum number of collocated pairs lie in the range of ± 0.5 m/s wind speed difference. All plots indicate that the CWIND wind speed measurements show an overall good agreement with scatterometer measurements. One point needs to be mentioned. Scatterometer winds are not obtained within 25 km from the coast. However, in this study, defining a spatial window with a maximum separation of 50 km had allowed CWIND SAR imagette close to the coast to be matched with scatterometer wind in more open waters, which may lead to bias. In future studies, greater care needs to be taken when verifying scatterometer data near coastal area.

4.4 Comparison of SAR Results with ERA 40 Model Data

In this section H_s, U_{10} and mean wave period (T_m) retrieval from SAR wave mode imagettes, using the empirical algorithm developed by Schulz-Stellenfleth et al. (2007), are compared to ECMWF ERA 40 reanalysis data set both on daily and statistical basis. First, the collocation method is described, afterwards the results are presented and discussed.

4.4.1 Method

A similar collocation method is used here to compare ERA 40 model data with SAR results. The available ERA 40 pixel is 2.5° × 2.5° wide at four times per day 00:00, 06:00, 12:00 and 18:00 UTC. So the maximum distance between the SAR image center and the ERA 40 results should be smaller than 1.25° in longitude and latitude, and the maximum time difference should be 3 hours. If more than one ERA 40 result can be co-located with one SAR retrieval, the average is used.

It has to be noted that the definition of mean wave height is different for CWAVE and ERA 40. The CWAVE definition of mean wave period is given by

$$T_{m-10} = \frac{m_{-1}}{m_0} \tag{4.6}$$

where m_{-1} and m_0 are the -1th and 0th spectral moment, respectively. However, the ERA 40 mean wave period is zero-up-crossing wave period. The zero up-crossing wave means the portion of a wave record (the time history of wave elevation) between adjacent zero up-crossings. A zero up-crossing occurs when the sea surface rises (rather than falls) through the still-water level. Wave records are conventionally analyzed on the basis of the zero up-crossing waves they contain. The period of a zero up-crossing wave is the time interval between the two zero up-crossings that bound it. Mean zero up-crossing period is calculated for a random sea by dividing the wave sampling period by the number of zero up-crossing waves in the sampling period.

4.4.2 Results and Discussion

A daily comparison between SAR results and ERA 40 is presented first (Fig. 4. 29) including H_s, U_{10} and T_m.

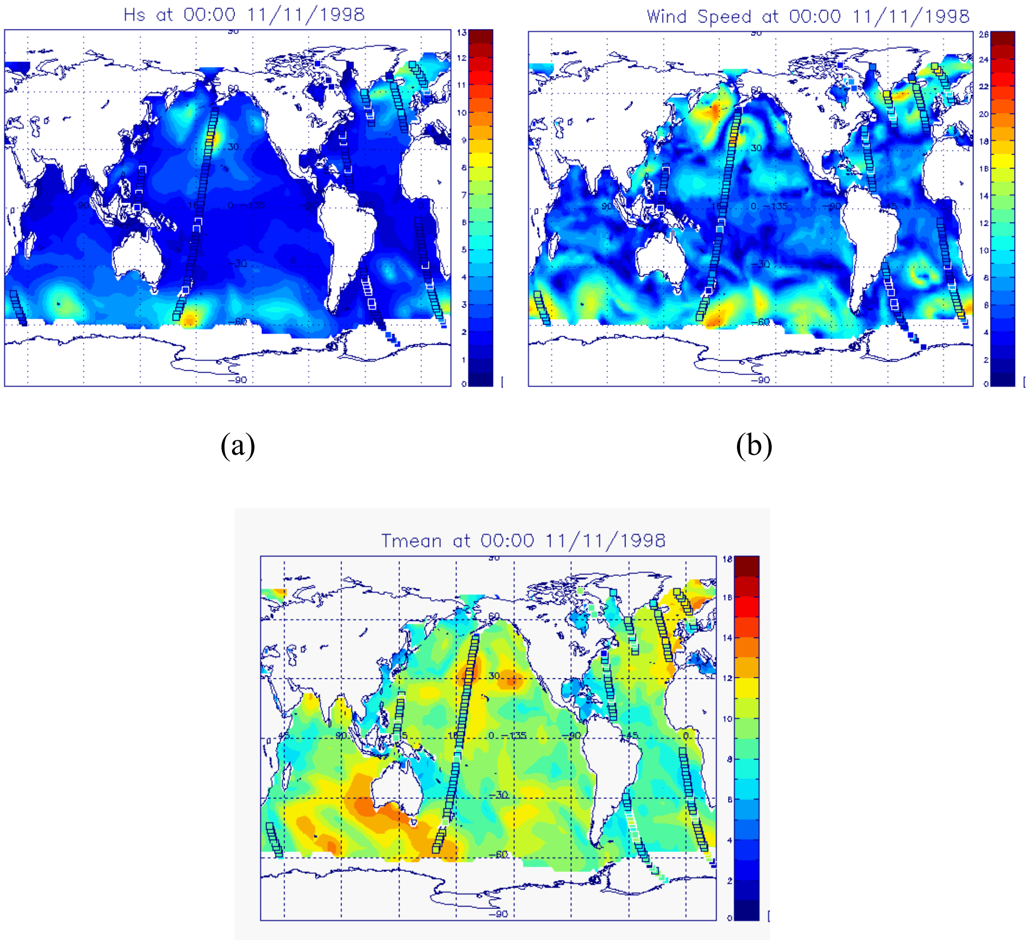

(a) (b)

(c)

Figure 4.29: Results of the SAR algorithm (squares) for significant wave height (a) and wind speed (b) mean wave period (c) in comparison to ERA 40 model results (background) at 00:00 on November 11th 1998.

Fig. 4.29 shows a typical example of the comparison to the SAR results superimposed on the map of the ERA 40 results. Colored squares represent the H_s, U_{10} and T_m derived from SAR data, the background map shows H_s, U_{10} and T_m from the ECMWF

ERA 40 model. The time difference between SAR measurement and ERA 40 data is less than 3 hours. A cyclone is situated in the north Pacific at 33.98° N, 169.57° W. The SAR measurement gives H_s=9.35 m, U_{10}=19.28 m/s and T_m=18.6 s, while the ERA 40 result is only 7.70 m, 16.47 m/s and 18.1 s. The SAR results show overall agreement with the ERA 40 model data for H_s and U_{10} along the satellite track. However, the SAR results are systematically smaller for T_m.

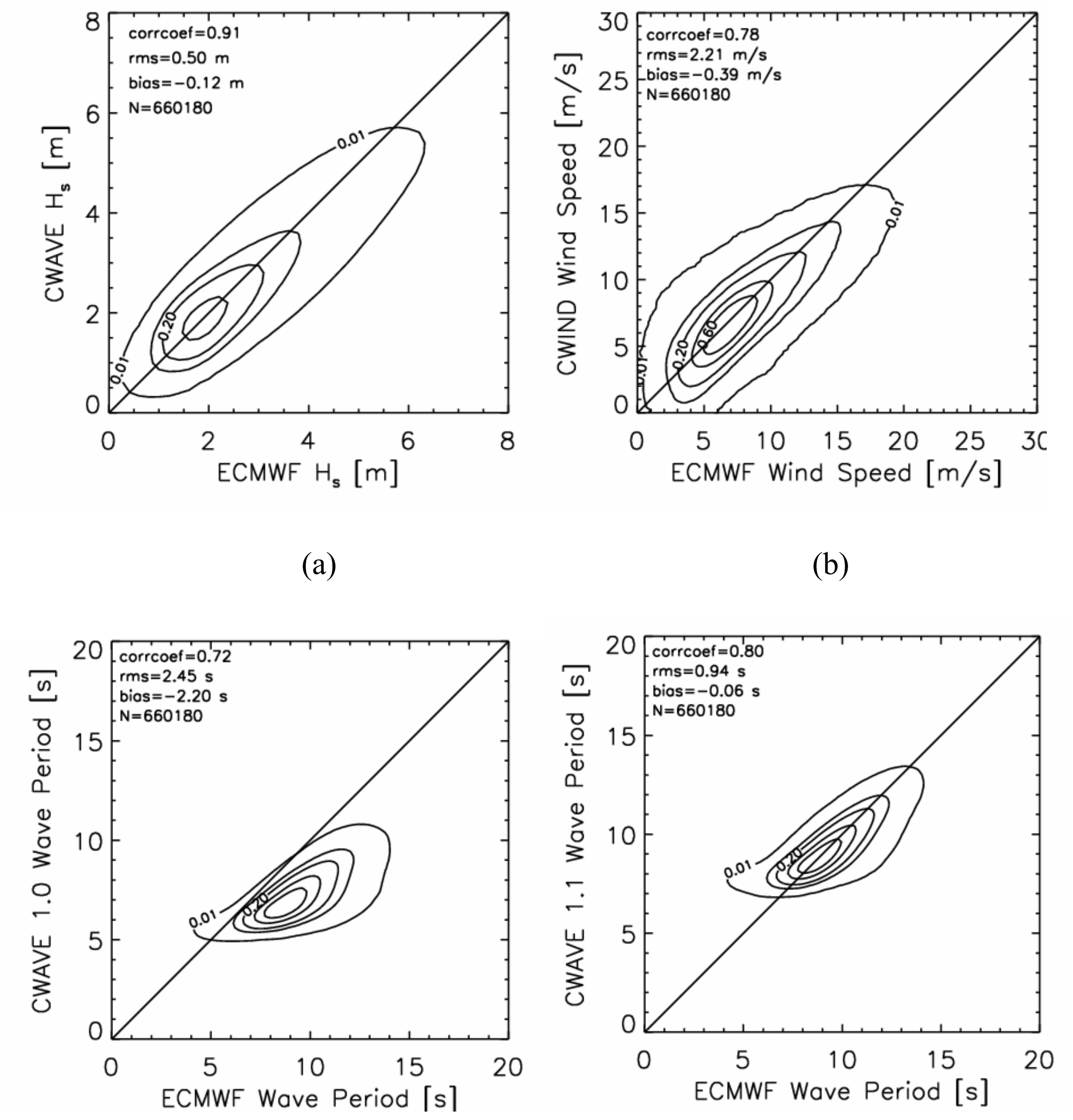

(a) (b)

(c) (d)

Figure 4.30: Scatter plot of SAR results versus ECMWF ERA 40 model data for (a) H_s, (b) U_{10}, (c) $T_{m\_1.0}$, (d) $T_{m\_1.1}$.

The statistical comparisons of SAR and ERA 40 data are depicted in Fig. 4.30 in scatter plots. The statistical parameters are also given using the formula Section 4.1.1. For H_s (Fig. 4.30(a)) with a rms error of only 0.50 m and a bias of -0.12 m, a very convincing correlation coefficient of 0.91 is found. The U_{10} comparison shows a bias of -0.39 m/s and a lower correlation coefficient of 0.78 jointly with a rms error of 2.21 m/s. The comparison of T_m shows a strong improvement from CWAVE 1.0 to CWAVE 1.1: the correlation coefficient grows from 0.72 to 0.80, rms error is reduced from 2.45 s to 0.94 s and the bias shrinks from -2.20 s to only -0.06 s. H_s and $T_{m\_1.1}$ from SAR show a better agreement with ERA 40 data than U_{10}.

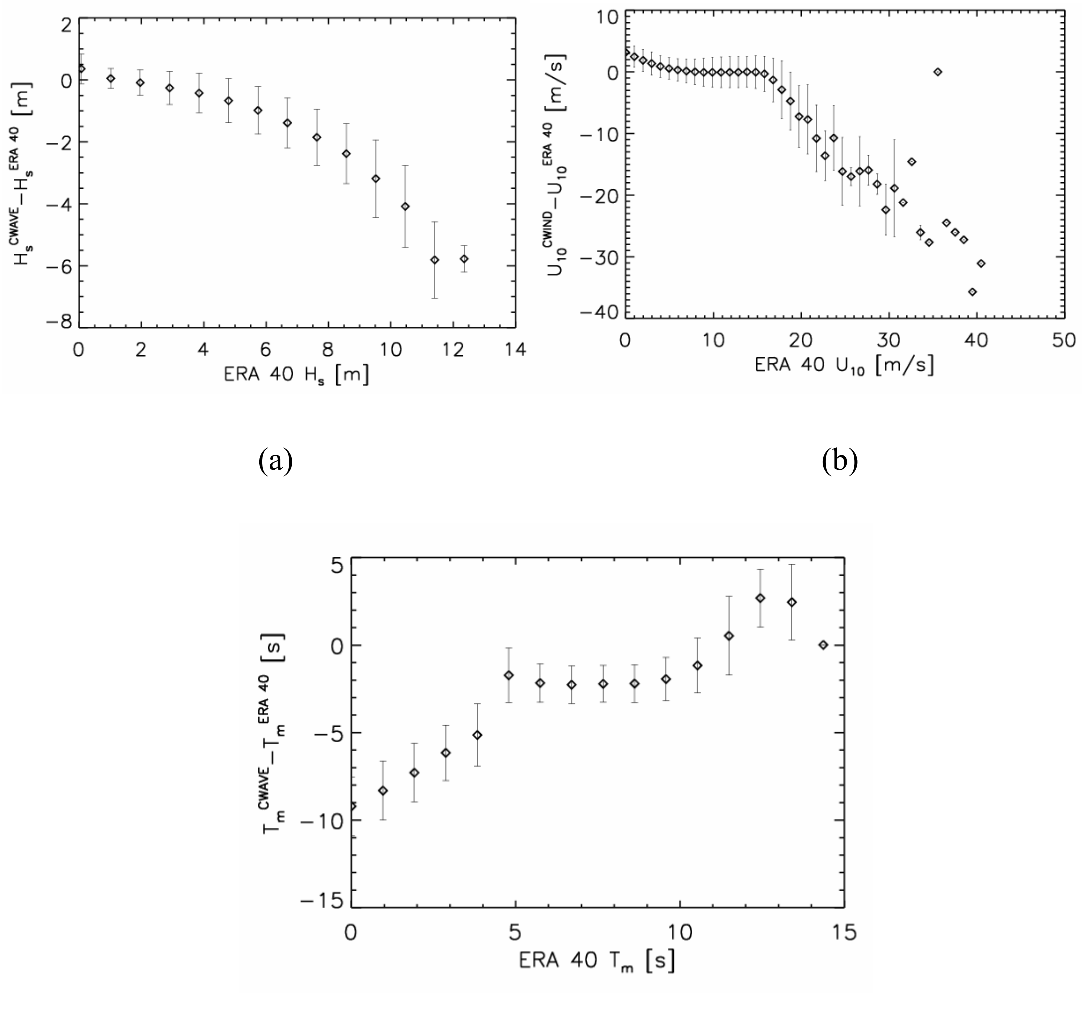

(a) (b)

(c)

Figure 4.31: The binned means for the H_s, U_{10} and T_m differences as a function of the ERA 40 value in 1 m, 1 m/s and 1 s intervals, including standard deviation for every bin.

In order to further compare SAR and ERA 40 data, the binned means for H_s, U_{10} and T_m differences as a function of ERA 40 in 1 m, 1 m/s and 1 s intervals are plotted in Figue 4.31 (a), (b), (c), respectively. The main results of these comparisons are:

- For the low and medium sea state ($H_s < 6$ m and $U_{10}<15$ m/s), there is a good agreement between SAR results and ERA 40 data for significant wave height H_s

and wind speed U_{10}. For the mean wave period T_m, the SAR results compare well with ERA 40 data only in the range from 5 s to 10 s.

- For high sea state, The SAR algorithms underestimate significant wave height and wind speed. However, there are only few collocated pairs (less than 20 for every bin) at high wind speed.
- The mean wave period T_m from SAR underestimates for the short mean wave periods ($T_m < 5$ s), while it overestimates for the long mean wave period ($T_m > 10$ s) in comparison to ERA 40.

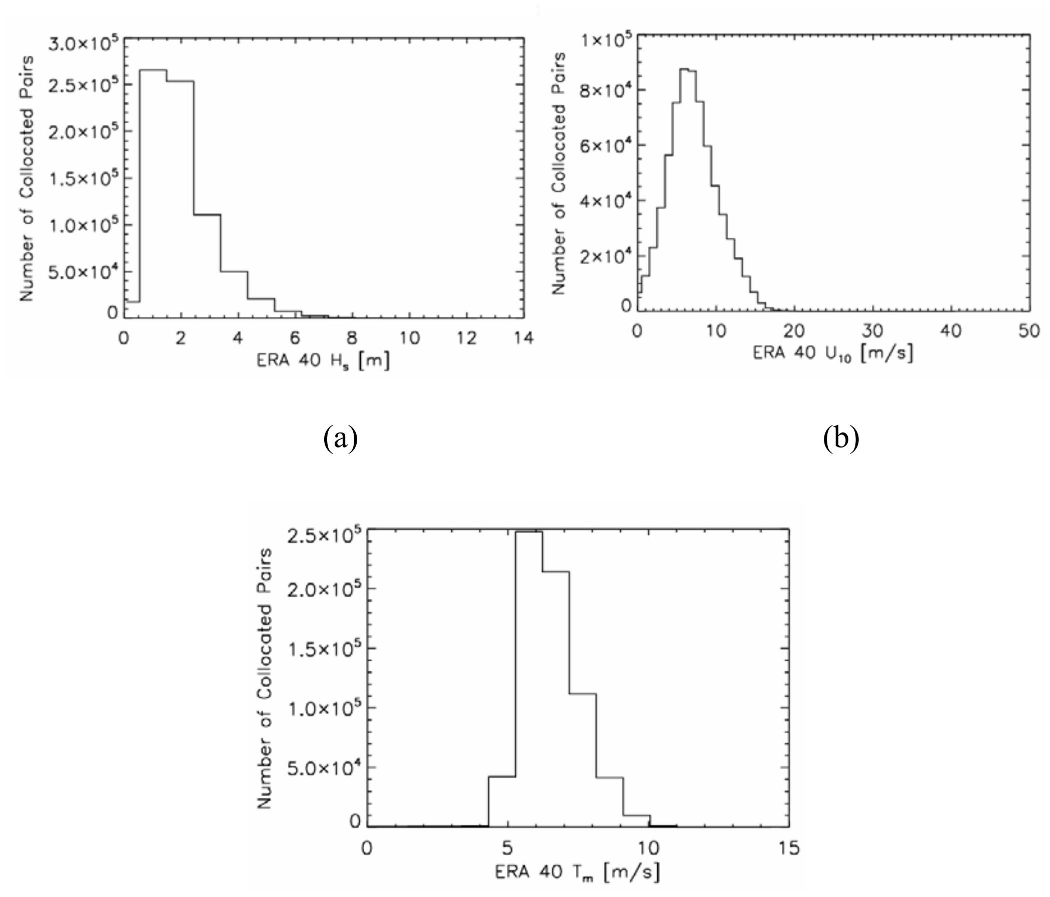

(a) (b)

(c)

Figure 4.32: Frequency distributions of the collocated pairs as a function of the ERA 40 parameter: (a) H_s, (b) U_{10} and (c) T_m.

The frequency distributions of collocated pairs between SAR results and ERA 40 data are given in Fig. 4.32. All indicate that most of the collocated pairs occur during medium sea state with $H_s \approx 2$ m, $U_{10} \approx 7$ m/s and $T_m \approx 7$ s. This point can also be seen from Fig. 4.33, which is a logarithmic scale for all three met-ocean parameters. Only, for $T_{m\_1.0}$, the histogram shows a strong differing distribution for SAR, while the histograms for H_s and U_{10} show good agreements.

We conclude from this comparison between SAR retrieval results and ERA 40 data for single days and the entire comparison period:

- H_s, U_{10} and $T_{m\_1.1}$ of SAR results show an overall agreement with the corresponding parameter of ERA 40 data, especially for low and medium sea state.
- Caires et al. (2001) point out that low wave heights up to 2 meters are overestimated and the high wave height are underestimated by ERA 40 data. This indicates that the SAR results may have the same problem as ERA 40 because they compare well with each other.
- There is a better agreement between SAR results and ERA 40 data for mean wave period in terms of $T_{m\_1.1}$ than in terms of $T_{m\_1.0}$.

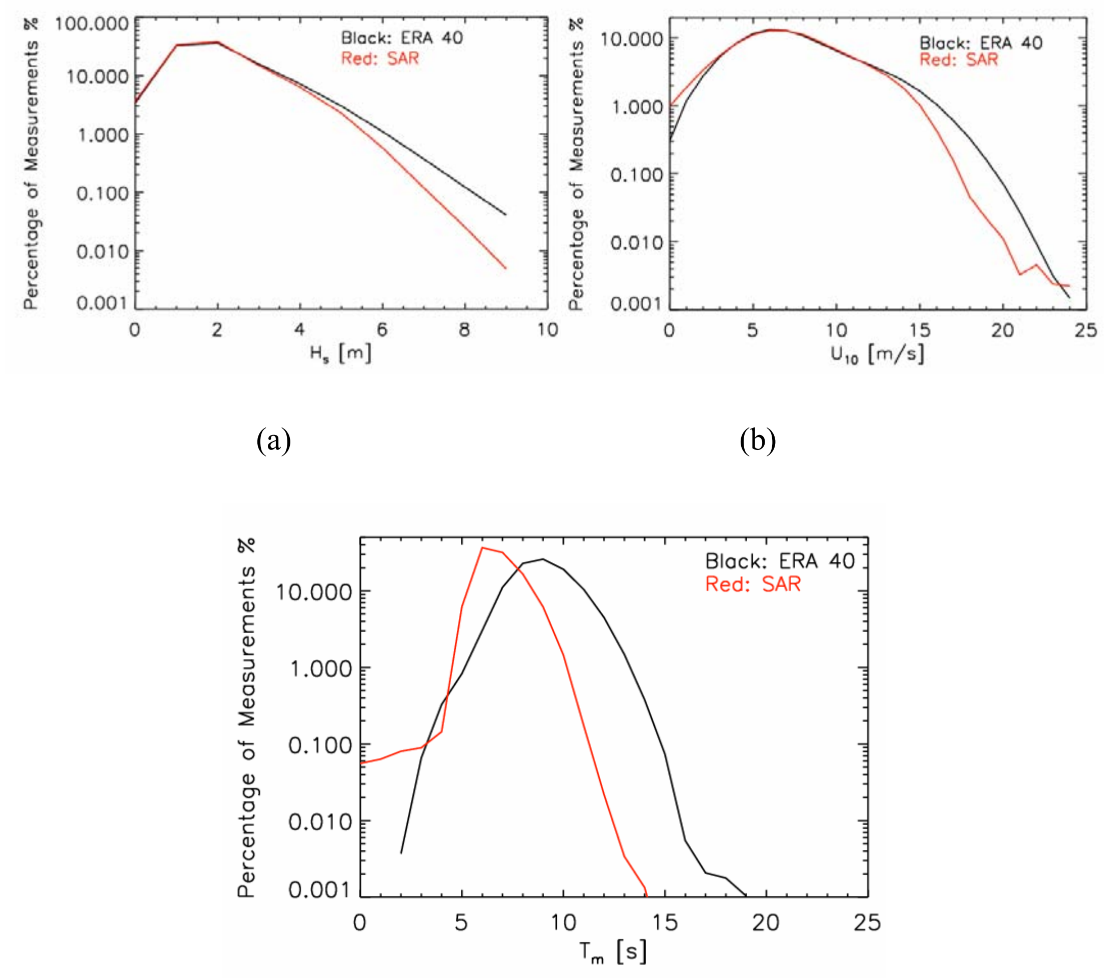

(a) (b)

(c)

Figure 4.33: Histograms of met-ocean parameter from SAR (red) and ERA 40 (black): (a) H_s, (b) U_{10} and (c) T_m.

4.5 Summary of Validations and Comparisons

In this section, first a summary of all validations and comparisons between SAR retrievals is presented, and then the latitudinal distributions of significant wave height for CWAVE and ERA 40 are compared and analysed.

4.5.1 Conclusions of Validations and Comparisons

In this chapter, six different types of data sets from NOAA buoys, Polarstern vessel, ERS-2 altimeter, ERS-2 scatterometer, HOAPS and ERA 40 are jointly compared to SAR retrievals. The maximally allowed temporal and spatial differences are given in Fig. 4.34. The scatterometer measurements fit to SAR wind speed best both in space and in time. Also the temporal difference between the SAR retrievals and altimeter data is close to zero, however, their spatial difference is large, up to 300 km due to observation geometry. The maximum collocation differences between NOAA buoy and SAR retrievals are half an hour in time and 100 km in space. However, larger differences between Polarstern vessel observations and SAR retrievals, namely 1.5 hours and 300 km, have to be allowed to get enough collocated pairs. The HOAPS wind speed values differ with SAR retrievals by up to 20 km and 3 hours. For the ERA 40 reanalysis data the maximum number differ from SAR retrievals by about 250 km and up to 3 hours.

Fig. 4.35 gives a summary of frequency distributions of all data sets, namely SAR retrievals, ERA 40 reanalysis, NOAA buoy observations, Polarstern vessel observations, HOAPS data and scatterometer measurements for significant wave height (a) and wind speed (b). The SAR retrieval distributions show a good overall agreement with other data sets, especially for medium sea state with 1 m<H_s<4 m and 5 m/s<U_{10}<15 m/s. However, a comparatively small percentage of SAR retrievals are found at high sea state condition with (H_s>5 m and U_{10}>15 m/s). Only the NOAA buoy data show smaller values. This is can be seen from Fig. 4.36, after removing the bins with too small number of collocated pairs, The binned mean H_s (a) and U_{10} (b) differences as a function of ERA 40, NOAA buoy, Polarstern, HOAPS, altimeter and scatterometer, respectively, including the standard deviation are presented in Fig. 4.36. It is obvious that the SAR retrievals tend to underestimate for high sea state, overestimate for low sea state and show a partly very good but overall good agreement for medium sea state. This comparison and validation figures strongly indicate that the SAR retrieval algorithms need to be improved for high sea state. One possible solution is to split SAR retrieval algorithms into different algorithm for different sea state.

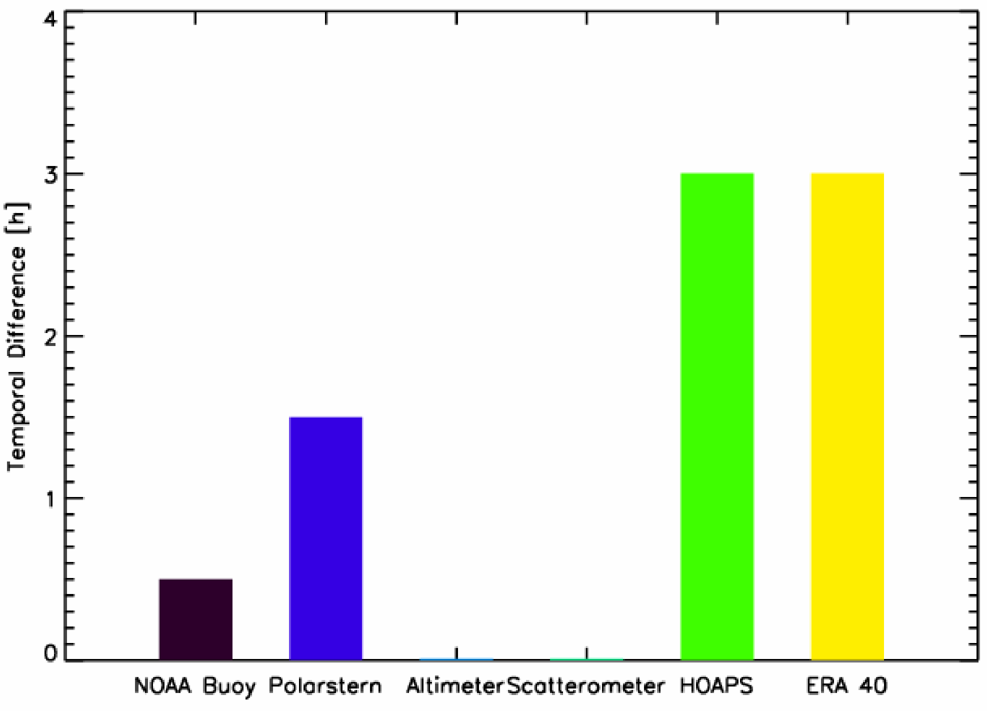

(a)

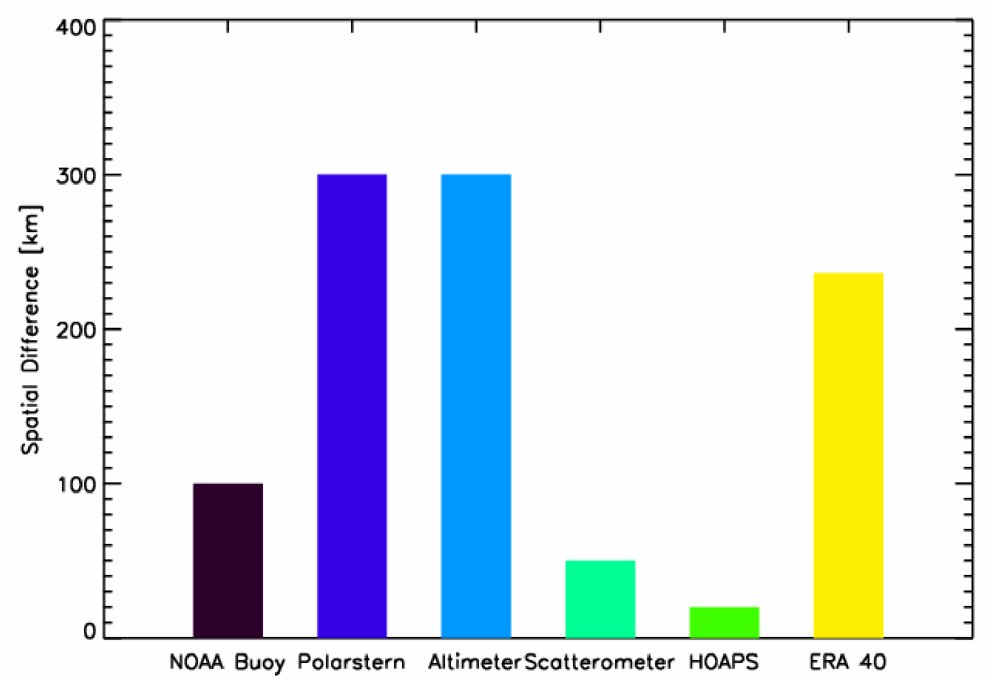

(b)

Figue 4.34: The maximum temporal (a) and spatial differences allowed between SAR retrievals NOAA buoy, Polarstern vessel, altimeter, scatterometer, HOAPS and ERA 40 data

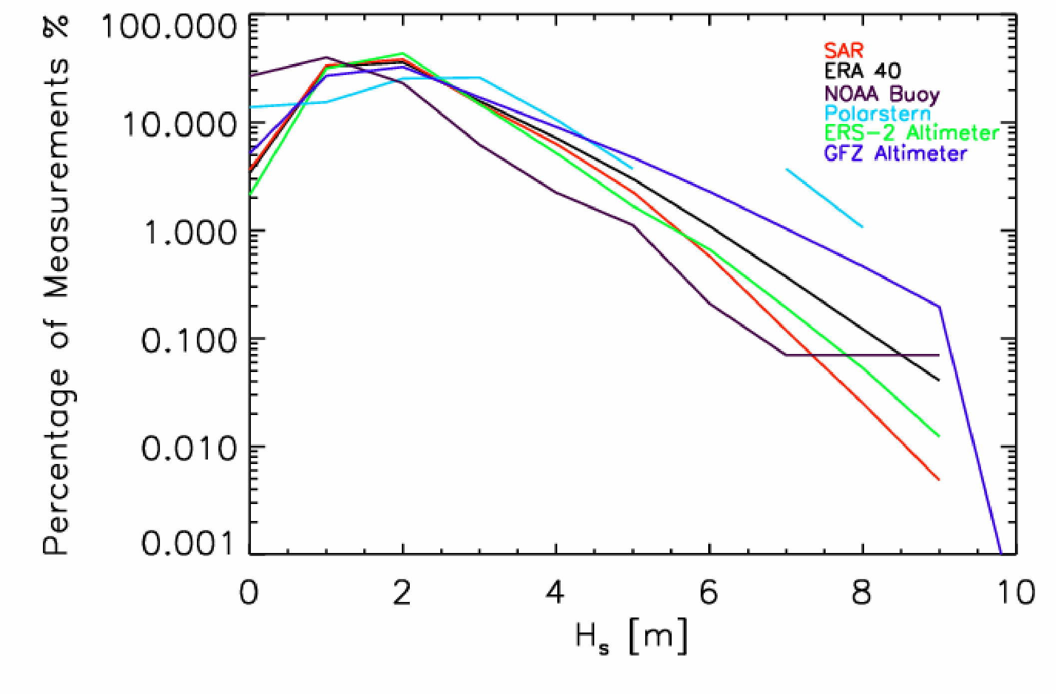

(a)

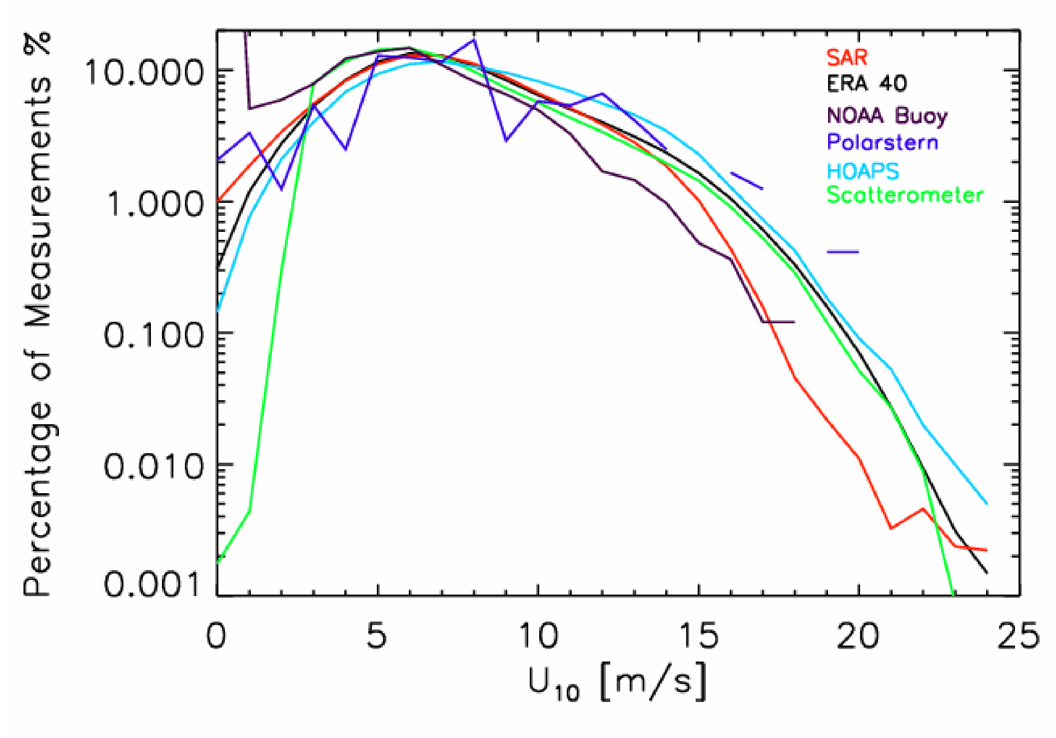

(b)

Figure 4.35: Frequency distributions of all data sets used for (a) significant wave height H_s and (b) wind speed U_{10}

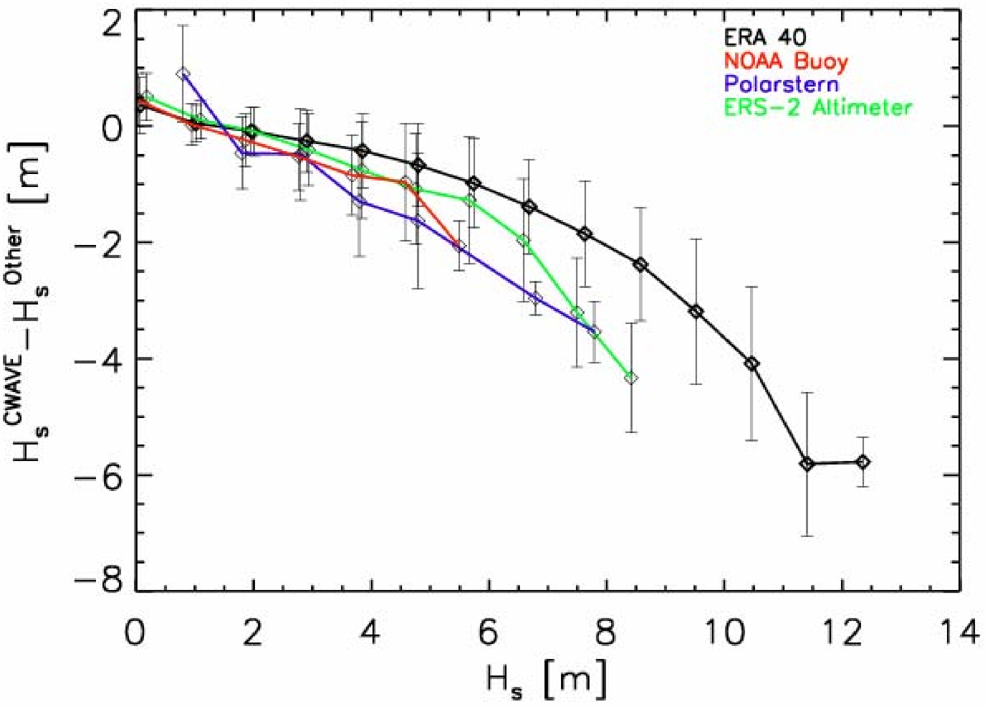

(a)

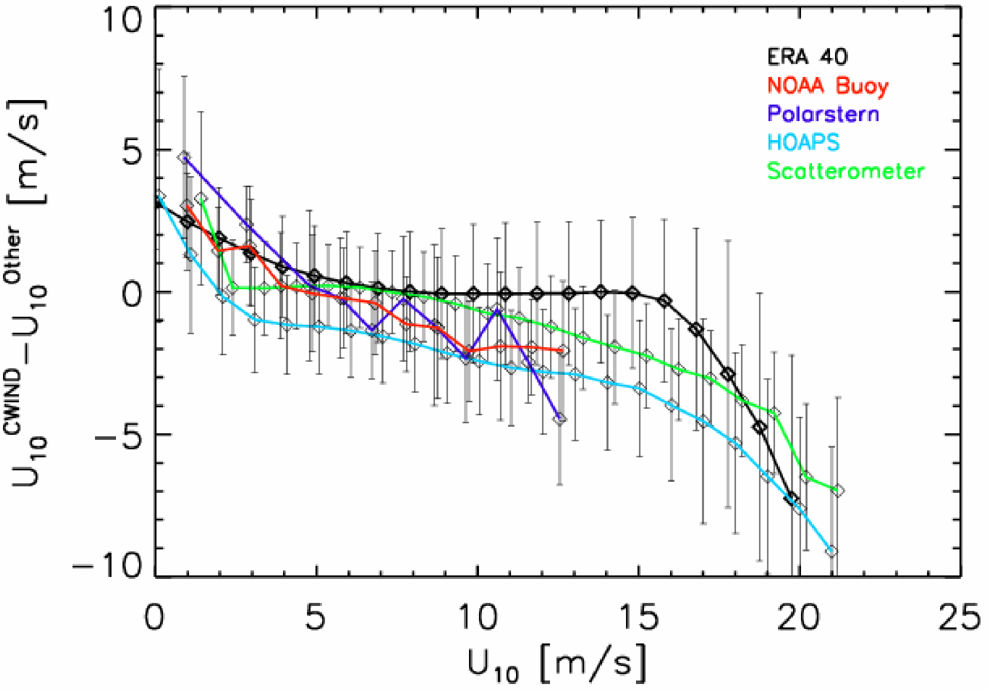

(b)

Figure 4.36: The binned mean between SAR retrievals and other datasets for (a) H_s and (b) U_{10} differences as a function of the values of all data sets used, including the standard deviation.

4.5.2 Latitudinal Dependence of Mean Significant Wave Height

Fig. 4.37 compares the seasonal means of H_s from SAR and ERA 40. The latitudinal dependence pattern of SAR and ERA-40 data is rather similar. Both data sets show maxima are between 40ºN and 60ºN in the Northern Hemisphere and around 50ºS in the Southern Hemisphere. The low H_s values near the equator are caused by the low wind speed zone known as 'doldrums'. The high H_s located between 40ºN and 60ºN in the Northern Hemisphere is due to high wind speed where a permanent high wind belt exists in winter, which (Fig. 4.38) is composed of wind speed maxima in both North Pacific and North Atlantic. The especially high H_s located at around 50ºS coincides with the so called circumpolar high winds in the roaring forties. It does not show a strong annual cycle in contrast to the Northern Hemisphere.

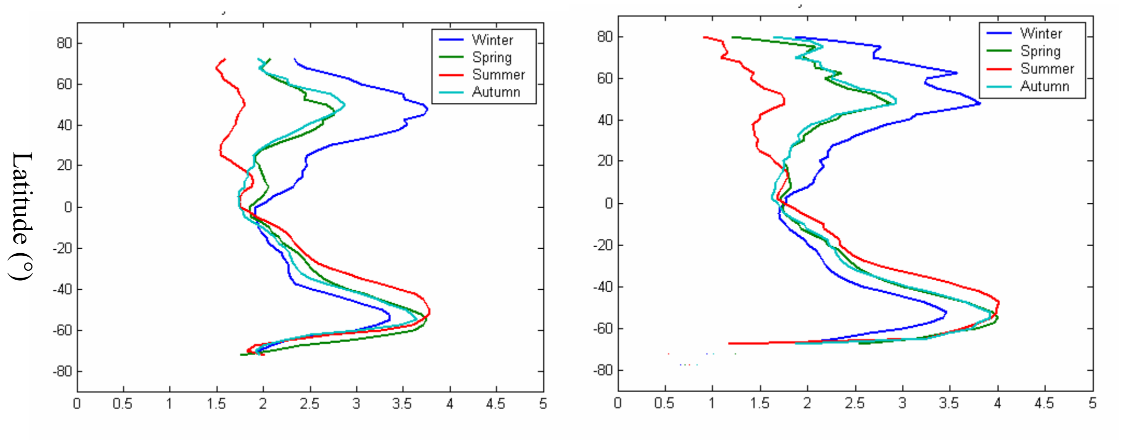

(a)

(b)

Figure 4.37: Mean values of H_s for all seasons from (a) SAR and (b) ERA 40 data.

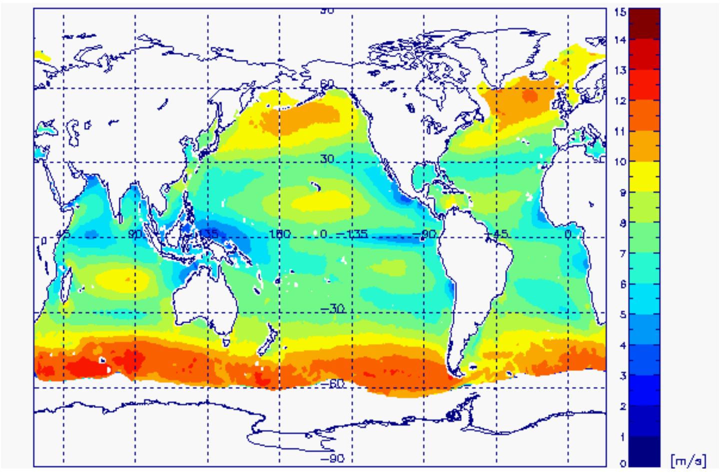

Figure 4.38: The mean wind speed from Sep. 1998 to Nov. 2000 from HOAPS with a spatial resolution 0.25º×0.25º

Chapter 5

Application of SAR Results

5.1 Retrieval of a Satellite-based Wind Wave Growth Relation

Normally, there are three methods to study ocean waves. The first one is the theoretical method which used hydrodynamics, mathematical statistics or energy balances to analyze the variability of ocean wave on the basis of some hypothesis. The second one is the experimental method that studies waves in the laboratory by choosing proper boundary and initial conditions to study the wave regime. The last one is the numerical modelling based on fluid dynamics, which starts with the energy balance equation and finally obtain the ocean wave spectrum. All results from these approaches should be validated by the in-situ data.

The wave growth relation is one of the most important subjects in the ocean wave research, especially in the wave analysis and prediction. In former studies, the wave growth relation has been derived from observations, experimental fitting, data analysis, theoretical analysis, or empirical formulae (Toba, 1972; Hasselmann et al., 1973; Wen，1962; Wang，1990; Guan, et al., 2002). However, all these approaches have two limitations.

The first limitation of former field observations lies in the unrealistic assumption of stationarity and homogeneity over time and length scales required to achieve the full development of a wind wave field. At a typical wind speed of 10 m/s these are, of the order of 16 h and 200 km, respectively. Four variables are usually needed to determine the wave growth relation: wave height, wave period, wind speed and wind fetch. Wave height, wave period and wind speed are easier measured than wind fetch. The wind fetch represents the distance over which a wind wave is fully developed under a homogeneous, steady wind field. But as such a steady wind field is not easy to find in observations. The wind fetch is difficult to determine from observations.

Secondly, the observation data used in the former studies were constrained to regions, and in many cases, the duration of observations was too short.

SAR images provide an opportunity to minimize both limitations, because the globally distributed significant wave height, wave period and wind speed can be directly obtained from SAR wave mode imagettes on a continuous basis using the empirical algorithm CWAVE. Therefore, in this section, a wind wave growth relation is derived from SAR images.

Figure 5.1 shows the statistical analysis of the significant wave height H_s versus mean wave period T_m derived from SAR images. The typical relationship between H_s and T_m can be seen in the red line, which represents the wind waves with smaller mean wave period. The blue line represents swell with larger mean wave periods. The mean value of H_s is 2.70 meters, and the mean value of T_m is 9.42 seconds. This indicates that the SAR results contain both kinds of waves: wind wave and swell.

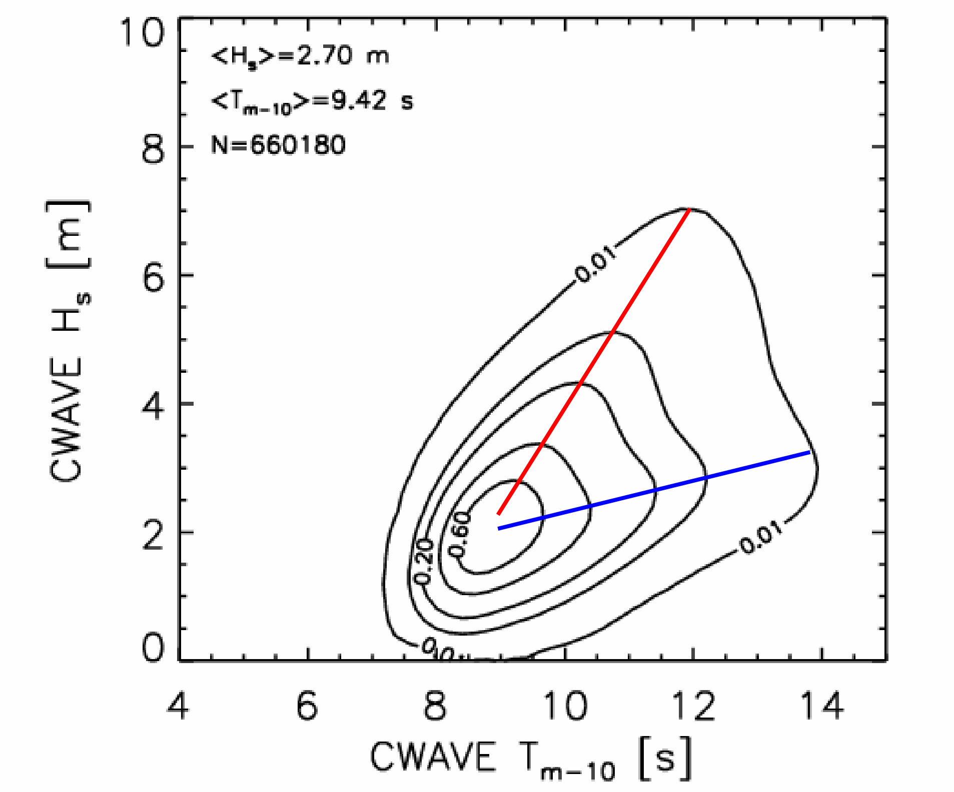

Figure 5.1: Significant wave height H_s versus mean wave period T_m derived from ERS-2 SAR imagettes

5.1.1 Existing Wind Wave Growth Relations

(1) Toba (Toba, 1972)

Toba (1972) proposed the famous three-half power law, based on dimensional analysis and Toba's 1961 wind-wave tunnel experiment data.

$$H_* = B_* T_*^{3/2} \tag{5.1}$$

Where $B_* = 6.2 \times 10^{-2}$, and

$$H_* = \frac{gH_s}{u_*^2} \qquad\qquad T_* = \frac{gT}{u_*} \tag{5.2}$$

u_* is the friction velocity, g is the acceleration of gravity, H_s and T are significant wave height and significant wave period, respectively. As we know the definition of the wave steepness (δ) and wave age (β) to be

$$\delta = \frac{H_s}{L} = \frac{2\pi H_*}{T_*^2}, \qquad \beta = \frac{C}{U_{10}} = \frac{\gamma}{2\pi} T_* \tag{5.3}$$

With L the wave length, we get after subtituting Eq. (5.3) into Eq. (5.1) the relation

$$\delta = (2\pi\gamma)^{\frac{1}{2}} B\beta^{-\frac{1}{2}} \tag{5.4}$$

Here $\gamma^2 = C_D$, represents the drag coefficient, for which Toba assumed $\gamma = 0.04$. Then the relationship between the wave steepness and wave age becomes

$$\delta = 0.031\beta^{-\frac{1}{2}} \tag{5.5}$$

(2) Neumann (1958)

The wind wave is more complicated than an ideal sinusoidal wave. There are many short and low waves overlapping with the long and high waves. The normal and tangential forces have an effect on each wave at the same time. In order to calculate the energy transport in this case, Neumann used the concept of the wave surface friction to propose a relationship between wave steepness δ and wave age β derived from in-situ observations as follows:

$$\delta = 0.215 / e^{1.667\beta} \tag{5.6}$$

(3) Ishida (Wang, 1990)

Ishida also proposed the following similar relationship derived from pipe experiments,

$$\delta = 0.0276 / \beta \tag{5.7}$$

(4) Wu (2004)

It is traditionally assumed that the relationship between wave steepness and wave age is independent of the wind wave growth state. In fact, the traditional relationship can not describe the whole course of wind wave growth. The relationship of the wave steepness and wave age also change with the wind fetch. Dimensionless wind fetch

$\tilde{x}$ is introduced to develop a new wind wave growth relation as follows:

$$\delta\beta = 6.0\times10^{-3}\,\tilde{x}^{2.04\times10^{-1}-3.40\times10^{-3}\ln\tilde{x}} \tag{5.8}$$

5.1.2 Derivation of a Wind Wave Growth Relationship from SAR Images

The SAR retrievals cover the global ocean which can avoid the limitation of former studies whose observation data normally were constrained to regions. Thus, the SAR retrievals are applied in this study to derive a new wind wave growth relation.

The friction velocity u_* is related to the wind speed at 10 meter level, U_{10}, by the equation,

$$u_*^{\,2} = C_D U_{10}^{\,2} \tag{5.9}$$

where C_D is the drag coefficient. Substituting (5.9) into (5.1), it follows that

$$\langle H_s\rangle = B\langle T\rangle^{3/2} \text{ or } \langle H_s\rangle C_D^{-\frac{1}{4}} = B_*\langle T\rangle^{3/2} \tag{5.10}$$

$$B = C_D^{\,1/4} B_* \tag{5.11}$$

$$\langle H_s\rangle = \frac{gH_s}{U_{10}^{\,2}} \qquad \langle T\rangle = \frac{gT}{U_{10}} \tag{5.12}$$

Since H_s, U_{10} and T can be derived from SAR image using the CWAVE algorithm, these data would be used to determine the remaining constants. It is however noted that the SAR results give a mean wave period, and need to be converted to the significant wave period by using the relation $T = 1.123\overline{T}$ (Guan and Sun, 2002). The value of B_* and the exponent of $< T >$ can be then refitted using SAR results. The universal formula can be written as,

$$\langle H_s\rangle C_D^{-\frac{1}{4}} = C\langle T\rangle^{\alpha} \text{ or } \langle H_s\rangle = CC_D^{\frac{1}{4}}\langle T\rangle^{\alpha} \tag{5.13}$$

Both C and α are constant and will be determined using the linear least square fitting.

C_D varies between 0.5×10^{-3} and 4.0×10^{-3}, and the arithmetic average of C_D is 2.25×10^{-3}. From Eq. (5.11), it follows that $B_1 = 0.927\times10^{-2}$ for low C_D, $B_2 = 1.56\times10^{-2}$ for high C_D and $\overline{B} = 1.35\times10^{-2}$ for mean C_D. However, the value of C_D was studied formerly as a function of both the wind speed and the air-sea temperature difference. Geernaert (1990) proposed an empirically determined drag coefficient as follows:

$$C_D = (0.49 + 0.07U_{10} + \frac{2.58}{U_{10}} - 1.06\frac{\Delta T}{U_{10}^{\,2}})\times10^{-3} \tag{5.14}$$

Where ΔT is the air-sea temperature difference.

Kara et al. (2000) gave another drag coefficient formula derived from a statistical analysis of global monthly climatologies of wind speed and air-sea temperature difference intervals.

$$C_D = C_{D0} + C_{D1}(T_s - T_a) \tag{5.15}$$

$$C_{D0} = 10^{-3}[0.862 + 0.088\hat{V}_a - 0.00089(\hat{V}_a)^2] \tag{5.16}$$

$$C_{D1} = 10^{-3}[0.1034 - 0.00678\hat{V}_a + 0.0001147(\hat{V}_a)^2] \tag{5.17}$$

$$\hat{V}_a = \max[2.5\,m/s, \min(32.5\,m/s, U_{10})] \tag{5.18}$$

Limits are set on the wind speed because the drag coefficient is constant (3.00×10^{-3}) when $U_{10} > 35$ m/s. Assuming U_{10}=10 m/s and $\Delta T = T_s - T_a = 1°C$, it follows that,

$$\frac{C_{D1}(T_s - T_a)}{C_{D0}} = 0.028 \tag{5.19}$$

$$\frac{1.06\dfrac{\Delta T}{{U_{10}}^2}}{0.49 + 0.07U_{10} + \dfrac{2.58}{U_{10}} - 1.06\dfrac{\Delta T}{{U_{10}}^2}} = 0.007 \tag{5.20}$$

Thus the air-sea temperature difference is less important than wind speed for C_D. Therefore, the air-sea temperature difference is assumed to be 0 in this study. Both Eq. (5.14) and Eq. (5.15) are used in this study to investigate the new wind wave growth relation.

After taking the natural logarithm, Eq. (5.13) reads as follows:

$$a\log\langle H\rangle - \frac{1}{4}a\log C_D = a\log C + \alpha a\log\langle T\rangle \tag{5.21}$$

$\langle H_s\rangle$, C_D and $\langle T\rangle$ can directly be obtained from SAR results, α and C need to be determined from a least squares fit.

5.1.3 Results and Discussion

In this section, 660,180 SAR measurements of significant wave height, mean wave period and wind speed are applied in a least squares fit of Eq. (5.21) to elimate the constants α and C. Fig. 5.2 contains the plot of $a\log\langle H\rangle - \frac{1}{4}a\log C_D$ versus $a\log\langle T\rangle$ for all SAR imagettes. The red line indicates the new wind wave growth relations derived from SAR results using different C_D formula. The blue line indicates Toba's 'three-half' power law. The new wind wave growth relation (Eq. (5.23)) using the C_D from Geernaert (1990) agrees better with Toba's 3/2 power law (Eq. (5.22)) than Eq. (5.24) for which the C_D from Kara et al. (2000) is used. This is mainly because the air-sea temperature difference plays a more important role in Eq. (5.15) than in Eq (5.14) which can be seen from Eq. (5.19) and (5.20).

$$\langle H_s \rangle = 0.062 C_D^{\frac{1}{4}} \langle T \rangle^{1.5} \tag{5.22}$$

$$\langle H_s \rangle = 0.0648 C_D^{\frac{1}{4}} \langle T \rangle^{1.564} \tag{5.23}$$

$$\langle H_s \rangle = 0.0494 C_D^{\frac{1}{4}} \langle T \rangle^{1.681} \tag{5.24}$$

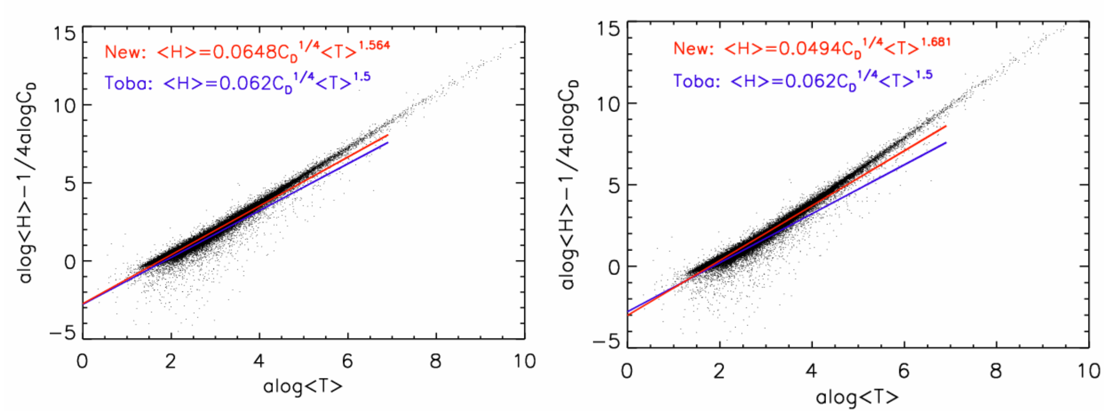

(a) (b)

Figure 5.2: New wind wave growth relation (red line) derived from SAR imagettes compared to Toba's 'three-half' power law (blue line) for different C_D formulae: (a) Eq. (5.14), (b) Eq. (5.15)

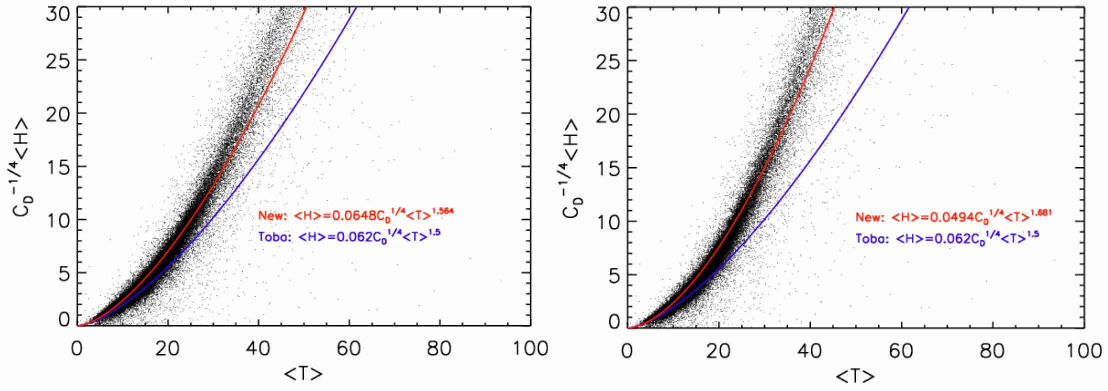

(a) (b)

Figure 5.3: $\langle H \rangle C_D^{-\frac{1}{4}}$ versus $\langle T \rangle$ for SAR imagettes different C_D formulae: (a) Eq. (5.14), (b) Eq. (5.15). The red and blue line are the same as in Fig. 5.2

Scatter plots of $\langle H \rangle C_D^{-\frac{1}{4}}$ versus $\langle T \rangle$ are given in Fig. 5.3. It can be seen that both of the new wind wave growth relations (red line) fit much better to the SAR measurements (points) than Toba's 3/2 power law (blue line). Toba's results tend to underestimate the $\langle H\rangle C_D^{-\frac{1}{4}}$ at the same $\langle T\rangle$ compared to the new wind wave growth relations and SAR measurements. This may be due to the inclusion of both wind wave and swell in the SAR measurements.

If we disregard the variation of the drag coefficient C_D with wind speed, in order to compare with former studies, Eq. (5.13) can be rewritten as

$$\langle H\rangle = B\langle T\rangle^{\alpha} \tag{5.25}$$

We then get Fig. 5.4 using the same fitting procedure as for Eq. (5.21) and the wind wave growth relation changes to

$$\langle H\rangle = 0.00860\langle T\rangle^{1.559} \tag{5.26}$$

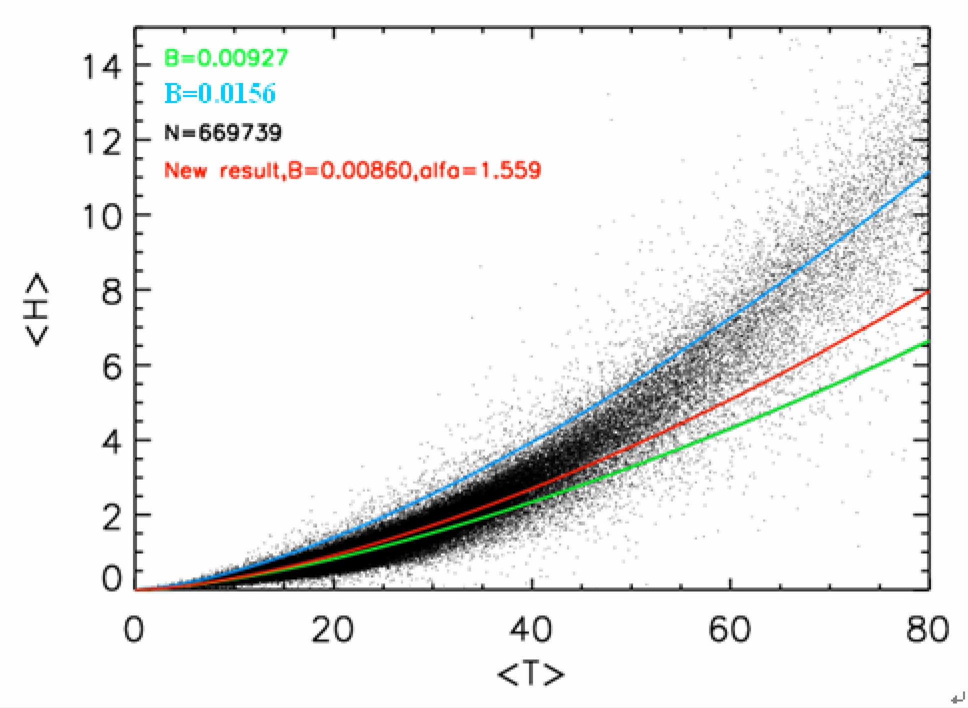

Figure 5.4: Scatter plot of $\langle H\rangle$ versus $\langle T\rangle$ for SAR data. The red line indicates the new Eq. 5.26 using the least square method for fitting. The green and blue line indicate Toba's 3/2 power law for low and high C_D corresponding to $B_1 = 0.927\times10^{-2}$ and $B_2 = 1.56\times10^{-2}$, respectively.

669,713 H_s, U_{10} and T_m values from SAR imagettes are used in Figure 5.4 to fit the new wind wave growth relation. All former studies on wind wave growth relation did not involve so many measurements. The fitted new line lies between two curves using Toba's relation for extreme C_D value (0.5×10^{-3} and 4×10^{-3}) leading to B=0.00860 and α=1.559. Former studies and our new results are listed in Table 5.1 after eliminating the dimensionless fetch. We assumed B constant in 'New result 2' and B as a function of wind speed in 'New result 1'. There is only a small variation of α, while B differs more strongly.

The value of B of our new result is smaller than other studies' result, if disregarding the variation of drag coefficient C_D with wind speed. This could be associated with the effect of swell on the wind sea. The SAR results contain wind wave as well as swell which can be seen from Fig. 5.1. Donelan (1987) has suggested that the well known reduction in the energy of laboratory wind waves when swell waves are added is due to the swell-induced detuning of the resonance conditions for non-linear wave-wave interactions. Similar effects have also been observed in Lake Ontario (Donelan et al., 1985) in the unusual circumstance of the coexistence of wind waves and swell. However, the SAR image has the potential to eliminate the swell effect by analyzing the SAR image spectrum.

The new results agree well with Toba's result, if the drag coefficient is considered as a function of wind speed (Eq. 5.14). This result is consistent with Young (1997) who found that the development of the atmospheric boundary layer with fetch has a significant influence on the observed wave growth.

Table 5.1: Comparison of wind wave growth relations from different authors.

Authors	$B \times 10^2$	α
Toba (1972)	1.35 or $6.2 C_D^{\frac{1}{4}}$	1.5
Hasselmann (1973)	1.232	1.515
Davidan (1980)	1.202	1.47
Kahma (1981)	1.569	1.5
Donelan (1985)	1.179	1.65
Dobson (1989)	1.048	1.65
Evans (1990)	1.144	1.453
Babanin (1998)	1.328	1.505
New result 1	$6.48 C_D^{\frac{1}{4}}$	1.564
New result 2	0.860	1.559

Next, the wind wave growth relations for different wind speed ranges and water depth are further investigated. Fig. 5.5 shows the scatter plot of $\langle H_s \rangle$ against $\langle T \rangle$. The results for $U_{10} \le 5$ m/s and $U_{10} \ge 5$ m/s are as follows,

$$\langle H_s \rangle = 0.00221 \langle T \rangle^{1.952} \tag{5.27}$$

$$\langle H_s \rangle = 0.00218 \langle T \rangle^{1.171} \tag{5.28}$$

It can be seen from Fig. 5.5 that the dimensionless significant wave height and significant wave period of SAR results vary greatly for different wind speed range. For $U_{10} \le 5\,\mathrm{m/s}$ $\langle H_s \rangle$ ranges from 0.2 to 6 and $\langle T \rangle$ varies from 15 to 60, however, for $U_{10} \ge 5\,\mathrm{m/s}$ $\langle H_s \rangle$ only ranges from 0.1 to 1.3 and $\langle T \rangle$ varies from 5 to 25. The result for high wind speed (Eq. 5.28) agrees better with Toba's 3/2 power law than for low wind speed. (Eq. 5.27).

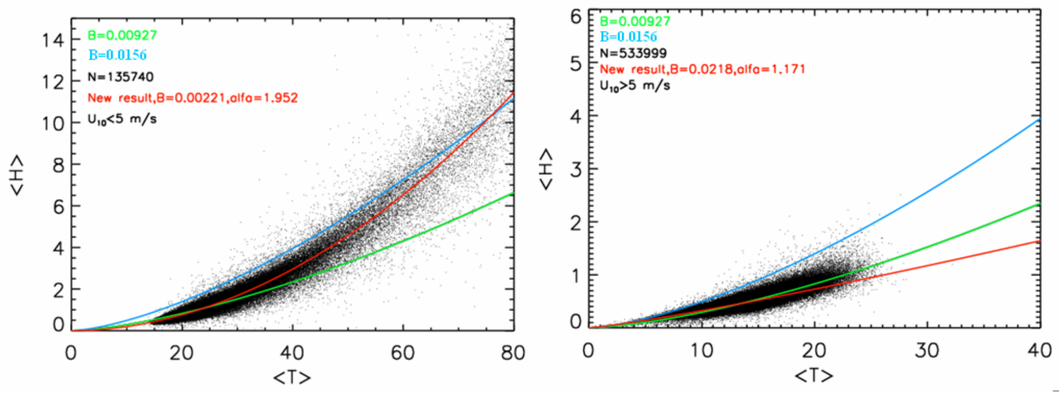

(a) (b)

Figure 5.5: Scatter plots of $\langle H_s \rangle$ against $\langle T \rangle$ for SAR imagettes for (a) low wind speeds, $U_{10} \le 5\,\mathrm{m/s}$ and (b) $U_{10} \ge 5\,\mathrm{m/s}$. The red line indicates our new results using the least square method. The green and blue line indicate Toba's 3/2 power law for very low and very high C_D corresponding to $B_1 = 0.927 \times 10^{-2}$ and $B_2 = 1.56 \times 10^{-2}$, respectively.

Two other effects become most pronounced in shallow water, especially close to the shore (Donelan et al., 1992):

Firstly, the variation in wind speed along fetch generally caused by the abrupt change in roughness from land to sea (Dobson et al., 1989);

Secondly, the differences in wave and wind propagation due to fetch geometry (Donelan et al., 1985). Therefore we also analyze the wind wave growth relations for different water depths.The resulting scatter plots of $\langle H_s \rangle$ against $\langle T \rangle$ are shown in Fig. 5.6. The red line indicates new results using the least square regression similar to above. The green and blue lines indicate Toba's 3/2 power law for low and high C_D corresponding to $B_1 = 0.927 \times 10^{-2}$ and $B_2 = 1.56 \times 10^{-2}$, respectively. More SAR results lie between two Toba's lines as the water depth becomes larger. There are very few points consistent with Toba's result for water depth $d \le 20\,\mathrm{m}$, $d \le 50\,\mathrm{m}$ and $d \le 100\,\mathrm{m}$. However, for $d \ge 1000\,\mathrm{m}$ most of our SAR results lie between both two lines with very different C_D. This indicates that the wind wave growth relations for shallow water and deep water are different, and need further analysis. For (a), (b), (c), (d) in Fig. 5.6, the SAR results are obviously wrong due to the effect of water depth, so the least square regressions are not given. However, for $d \geq 1000\,\text{m}$, the least square regression result is as follows,

$$\langle H_s \rangle = 0.00854 \langle T \rangle^{1.564} \tag{5.29}$$

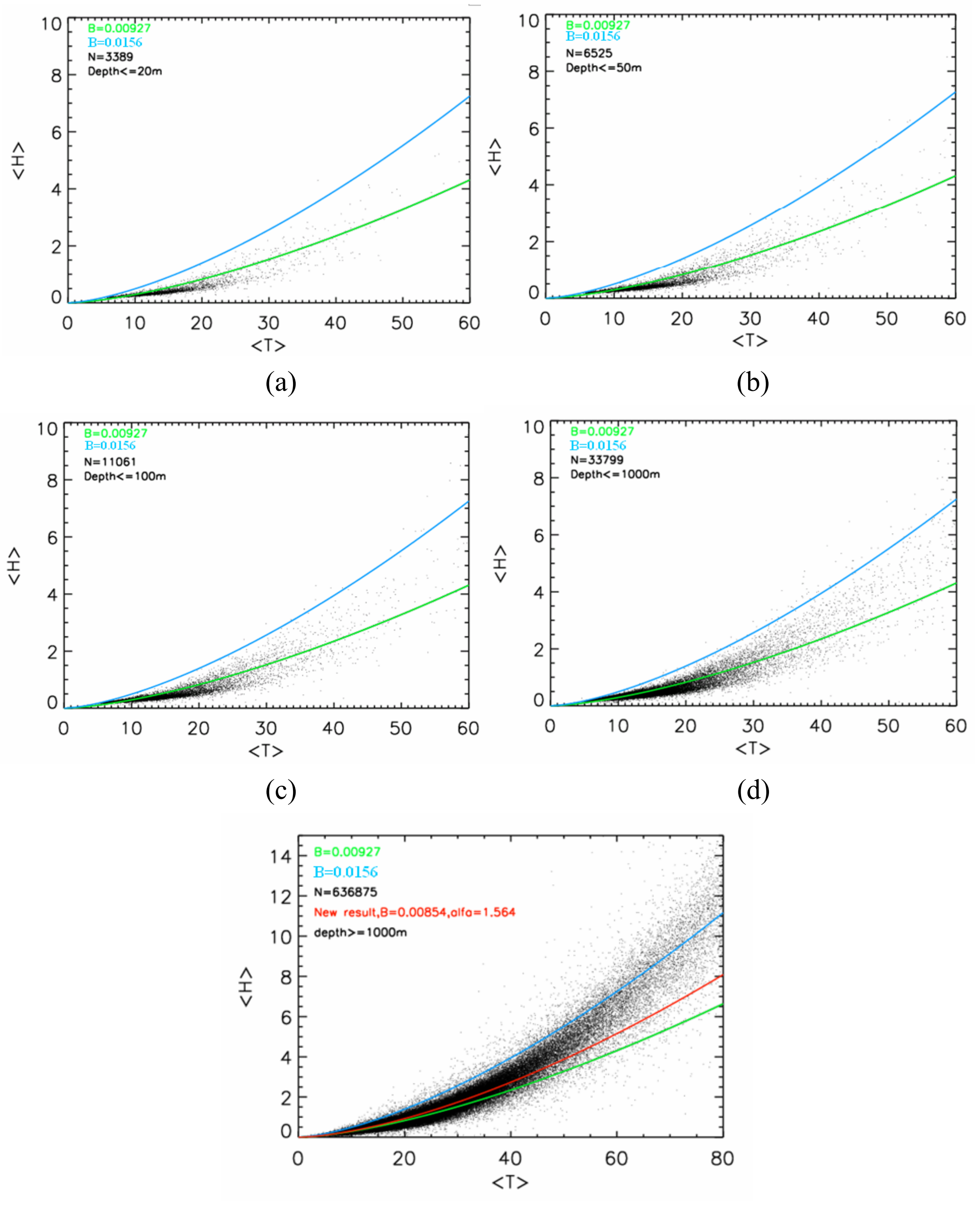

(a) (b)

(c) (d)

(e)

Figure 5.6: Scatter plots of $\langle H_s \rangle$ against $\langle T \rangle$ for SAR data at different water depth (d): (a) $d \leq 20\,\text{m}$; (b) $d \leq 50\,\text{m}$; (c) $d \leq 100\,\text{m}$; (d) $d \leq 1000\,\text{m}$; (e) $d \geq 1000\,\text{m}$. The red line indicates new results using the least square method. The green and blue line indicates Toba's 3/2 power law for low and high C_D corresponding to $B_1 = 0.927 \times 10^{-2}$ and $B_2 = 1.56 \times 10^{-2}$, respectively.

This result is consistent with the former studies (Table 5.1). This also indicates that the SAR measurements are more reliable at water depth above 1000.

5.2 Detecting a Storm Missed by ERA 40

The horizontal resolution of ERA 40 data used in this study is a 2.5°×2.5° regular latitude/longitude grid. The ERA 40 data may miss some storms due to such a coarse grid (Caires and Sterl, 2001). However, the SAR wave mode image covers 5 km × 10 km with high resolution which is about 5 m in azimuth direction and 10 m in range direction. Such high resolution image can detect detailed information about the surface waves.

Table 5.2: Comparison between SAR and ERA 40 for imagettes in Fig. 5.7

	SAR (CWAVE)	ERA 40
H_s (m)	7.17	2.19
U_{10} (m/s)	19.65	8.23

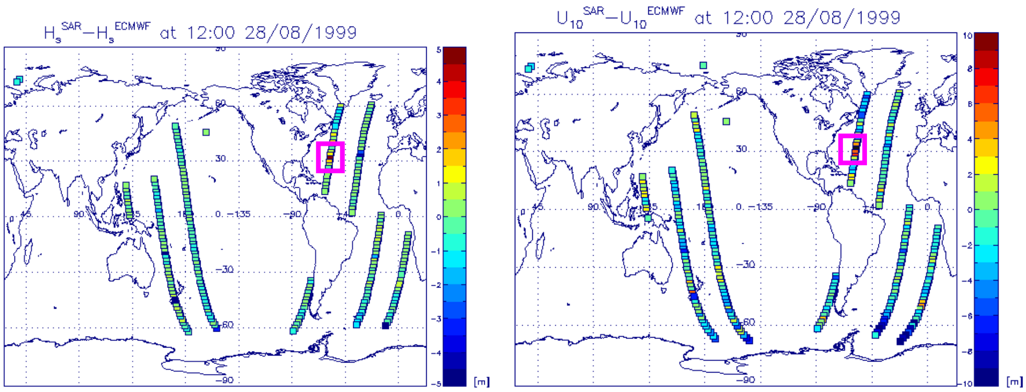

(a) (b)

Figure 5.7: Difference of significant wave height H_s (a) and wind speed U_{10} (b) for CWAVE and ERA-40 data on 28 August 1999 at 12 hours UTC.

Here we present an example of a storm missed by the ECMWF ERA 40 dataset, which was, however, detected by SAR. Fig. 4.29 shows a typical example of the comparison to the SAR results superimposed on the map of the ERA-40 results. Coloured squares represent the H_s, U_{10} and T_m derived from SAR data, the background map shows H_s, U_{10} and T_m from the ECMWF ERA 40 model. The time difference between SAR measurement and ERA 40 data is less than 3 hours. A storm is situated in the north Pacific at 33.98° N, 169.57° W. The SAR measurement gives H_s 9.35m and U_{10} 19.28 m/s while the ERA 40 result is only 7.70 m and 16.47 m/s.

All SAR images are tested for homogeneity. Images that show surface features which degrade the image spectrum are sorted out for later comparisons. But in Fig. 4.29 squares with a white frame mark these inhomogeneous imagettes, while squares with a black frame are homogeneous and are used for wind speed and sea state measurements.

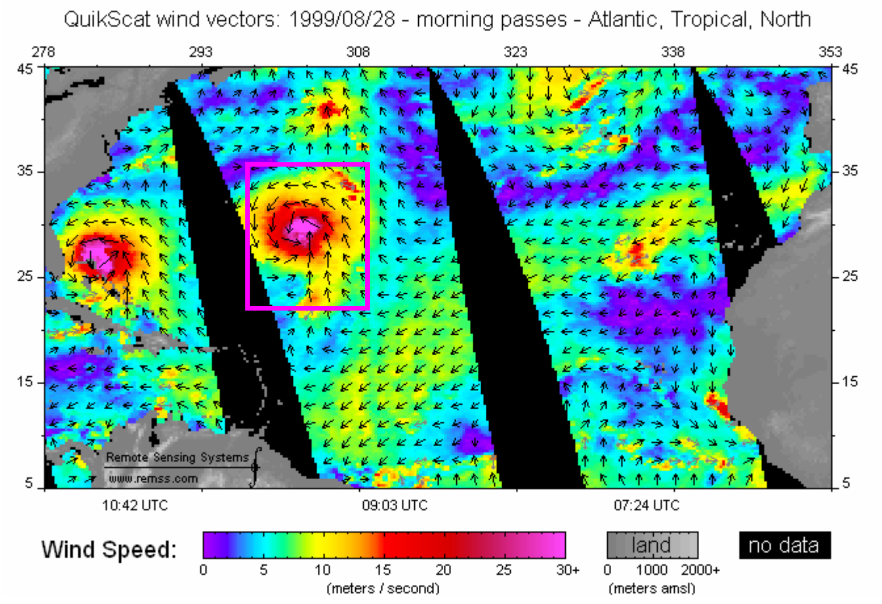

Figure 5.8: Wind vectors derived from QuikScat on 28 August 1999; taken from http://www.ssmi.com/

The example above shows that the SAR H_s and U_{10} measurements are typically above ERA 40 analyses. Also storms completely missed by ERA-40 dataset can be detected, using the CWAVE SAR algorithm. Fig. 5.7 shows one example of a storm missed by ERA 40 data. One can observe that SAR results of both H_s and U_{10} are much larger than those of ERA-40 at 58.10° W 31.35°N. Table 5.2 shows the H_s and U_{10} values of CWAVE and collocated ERA-40 data. From Quikscat data in Fig. 5.8 one also can see, that high wind speed exists in the same area. Hence, SAR has the ability to detect the storms missed by ERA 40 data.

5.3 Polar Low Detection

A polar low is a meso-scale, short-lived atmospheric low pressure system (depression) that is found over the ocean areas polarward of the main polar front in both the

Northern and Southern Hemisphere. The systems usually have a horizontal length scale of less than 1,000 km and exist for less than a couple of days. They are part of the larger class of mesoscale weather systems. Polar lows are often difficult to detect using conventional weather reports and are a hazard to high-latitude operations, such as shipping to and from gas and oil platforms.

Polar lows have been referred to by many other terms, such as comma cloud, mesocyclone, polar mesoscale vortex, Arctic hurricane, Arctic low, and cold air depression. Today the term is usually reserved for the more-vigorous systems that have near-surface winds of at least gale force (17 m/s).

Polar lows were first identified on the meteorological satellite imagery that became available in the 1960s, which revealed many meso-scale cloud vortices at high latitudes. The most active polar lows are found over certain ice-free maritime areas in or near the Arctic during the winter, such as the Norwegian Sea, Barents Sea, Sea of Japan, and Gulf of Alaska. Polar lows dissipate rapidly when they make landfall. Antarctic systems tend to be weaker than their northern counterparts since the air-sea temperature differences around the continent are generally smaller. However, vigorous polar lows can also be found over the Southern Ocean.

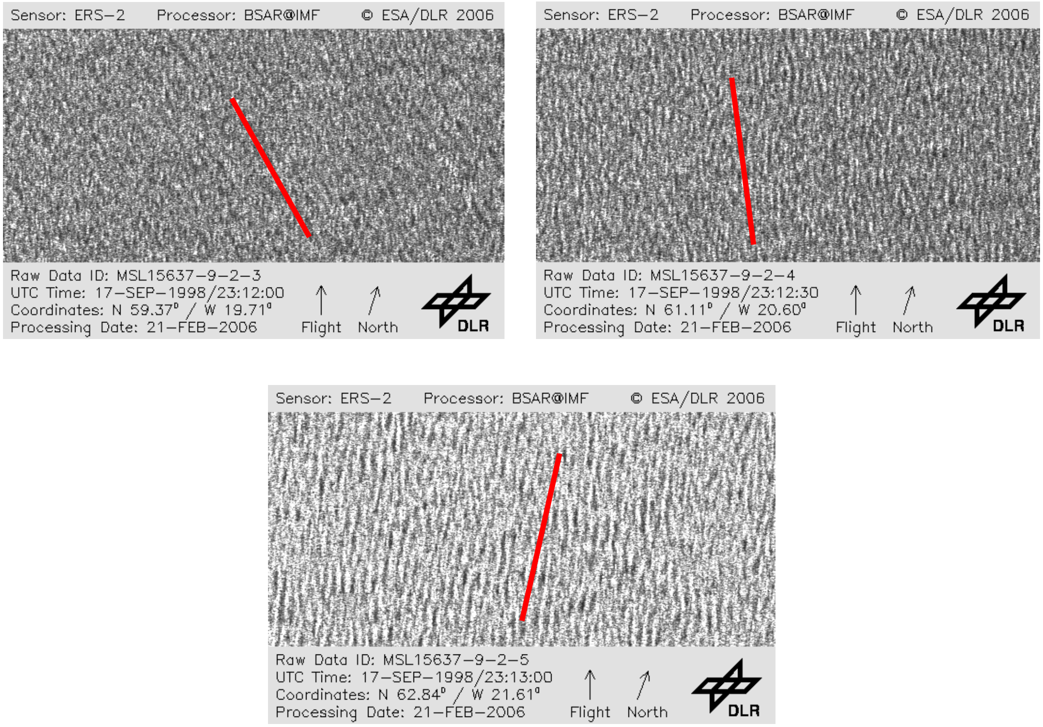

Figure 5.9: Three continuous wave mode imagettes as a time series, the red line represents the SAR streaks which are parallel to the mean wind direction

Polar lows can have a wide range of cloud signatures in satellite imagery, but two broad categories of cloud forms have been identified. The first is the ‘spiral’ signature consisting of a number of cloud bands wrapped around the centre of the low. Some polar lows have the appearance in satellite imagery of tropical cyclones, with deep thunderstorm clouds surrounding a cloud-free ‘eye’, which has given rise to the use of the term ‘Arctic hurricane’ to describe some of the more active lows. These systems are commonly deep within the polar air. The second is a ‘comma-shaped’ signature that is found more frequently with systems closer to the polar front.

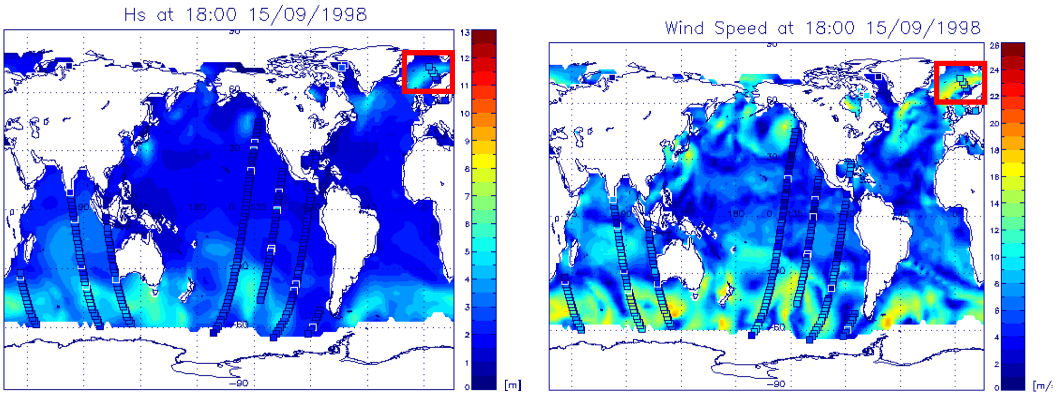

(a) (b)

Figure 5.10: The location (red square), significant wave height (a) and wind speed (b) maps from ERA 40 corresponding to the three imagettes from Fig. 5.9

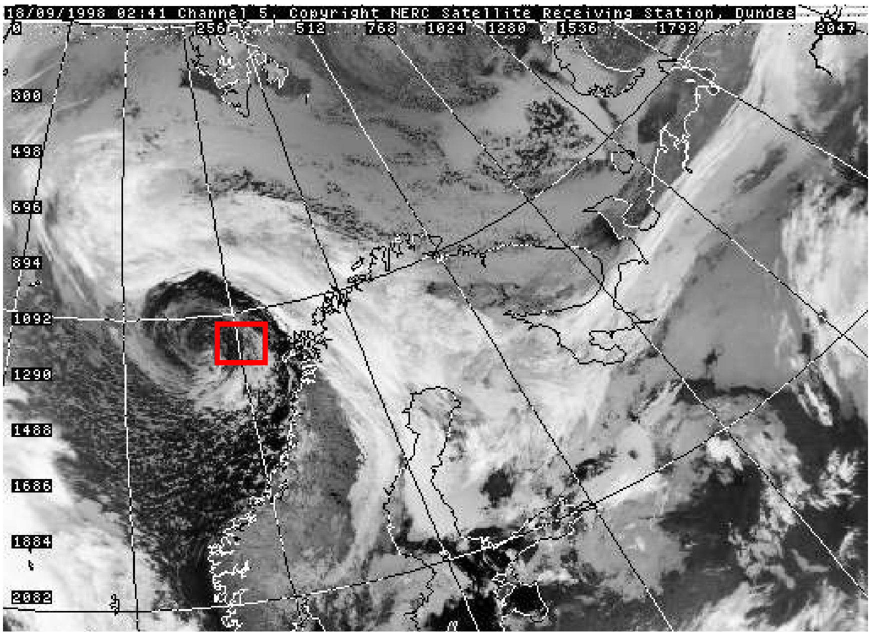

Figure 5.11: AVHRR image at 17:22 September 15, 1998. The red framed square is corresponding to the three wave imagettes of Fig. 5.9.

Next, we provide one example to detect a Polar Low using SAR wave mode imagettes with the help of AVHRR image. The criterion used in this study to detect Polar Low is that wind speed $U_{10} \geq 15$ m/s, significant wave height $H_s \geq 5$ m/s and the latitutinal position > 60°. A series of images on 17 September 1998 (Fig. 5.9) are found that correspond to these three conditions. The images have a time separation of 30 seconds which correspond to a horizontal distance of roughly 200 km. From the red line in the image, the wind direction rotation along the flight path can be easily seen. Figure 5.10 shows the location (red square), significant wave height and wind speed maps from ERA 40 corresponding to the three imagettes of Fig. 5.9. The average wind speed is 16.8 m/s and the average significant wave height is 5.6 m/s. Fig. 5.11 proves that detection of polar lows is possible with SAR imagettes, supported by the comma cloud in the AVHRR image.

Chapter 6

Summary, Conclusion and Outlook

In this thesis, the performance of the CWAVE algorithm was investigated using data sets from NOAA buoys, Polarstern research vessel, ERS-2 altimeter and scatterometer, HOAPS and ERA 40 reanalysis. This thesis contains both theoretical investigations as well as a statistical analysis of the data sets.

6.1 Summary and Conclusions

A global data set of slightly more than two years of processed ERS-2 SAR wave mode data enabled the application of CWAVE algorithm on a statistical basis for the first time. The data set comprises more than 1 million imagettes acquired from 1 September 1999 to 30 November 2000.

6.1.1 Detection of Inhomogeneous Imagettes

A new classification parameter based on the minimum normalized radar cross section (NRCS) of subimagettes compared to the mean NRCS of the whole imagette, was developed to detect inhomogeneities. The imagettes were divided into two classes: Firstly, inhomogeneous imagettes available for the analysis of image patterns associated with phenomena like small scale wind structure, rain cells, oil or natural films or sea ice; and secondly homogeneous imagettes suitable as input for the CWAVE algorithm. These homogeneous imagettes also can be used to extract wave parameter by other method.

The new classification parameter was applied to about 1 million SAR wave mode imagettes and the global distribution of the inhomogeneous imagettes was investigated and compared to the old parameter called Inhomo in this study. The largest inhomogeneous area except the polar sea-ice area is close to the equator in the West Pacific Ocean (90°E-150°E, 20°S-20°N), west of Central America

(135°W-90°W, 0°-30°N), the equatorial Indian Ocean (46°E-80°E, 3°S-10°N) and close to the West African coast (20°W-10°W, 3°N-15°N). The main reason of the strong inhomogeneity proportion in these areas is low wind speed favouring surface film development. The percentage of inhomogeneous imagettes for the new classification parameter is much higher in the Arctic area than for Inhomo pointing to the new classification being more rigorous. The new classification parameter also fit better with SSM/I sea-ice concentration data than for Inhomo.

6.1.2 SAR Algorithms Comparison

Two wind algorithms used for ENVISAT advanced synthetic aperture radar (ASAR) data, i. e. CMOD4 from the European Space Agency (ESA) and CMOD_IFR2 from Quilfen et al. (1998), are compared for only one case study. The wind direction is estimated from orientation of low and linear signatures in the ASAR imagery. The wind direction has inherently a 180° ambiguity since only a single ASAR image is used. The 180° ambiguity for the above algorithms is eliminated by using the buoy data from NOAA (National Oceanic and Atmospheric Administration) buoys moored in the Pacific. Wind speed is obtained with the two wind algorithms using both estimated wind direction and normalized radar cross section (NRCS). The retrieved wind results agree very well with the data from Quikscat. The root mean square error (RMSE) of wind direction is only 2.80°. The RMSEs of wind speed from CMOD4 model and CMOD_IFR2 model are 1.09 m/s and 0.60 m/s, respectively. The results indicate that the CMOD_IFR2 model is slightly better than CMOD4 model for high wind speed.

6.1.3 Wind Vector Retrieval from ASAR Using Dual Polarization

In this thesis, a new method to retrieve the wind vector using dual polarization advanced synthetic aperture radar (ASAR) image was developed. This method effectively eliminates 180º ambiguity which occurs when using a single ASAR imagery without dual polarization to retrieve wind vector. This method also solves the problem that the retrieval results are unreliable at very small spatial scales. The retrieved wind results agree well with the data from Quikscat. The root mean square error of wind direction and wind speed are reduced to 2.21º and 0.53 m/s, respectively. The results from the ASAR dual polarization image for wind speed and wind direction are also in agreement with a collocated buoy measurement.

6.1.4 Validation of the Retrieval Algorithm CWAVE

Validations of H_s and U_{10} using the CWAVE algorithm were carried out by comparison to in situ observations from NOAA buoy and Polarstern research vessel. Rather good agreement was found for validation with NOAA buoy data with RMSE of 0.61 m for H_s and 2.40 m/s for U_{10}. While it grew to 1.35 m and 3.19 m/s for the validation with Polarstern observation by eye, indicating that the H_s and U_{10} retrievals with CWAVE fit better with NOAA buoy observations. Because the Polarstern H_s observations are from visual inspection by weather observers they might be less accurate than NOAA buoy data. Furthermore, the Polarstern vessel seldom observed high wind speed, due to safety considerations of a ship.

The comparisons between CWAVE H_s and U_{10} and other satellite observations like from the ERS-2 altimeter for H_s, the ERS-2 Scatterometer for U_{10} and HOAPS for U_{10} led to better agreement, due to many more collocation pairs. RMSE for all collocated CWAVE and altimeter H_s is 0.56 m, it is 1.77 m/s for Scatterometer U_{10}, but increases to 2.87 m/s for HOAPS U_{10}. The CWAVE results retrieved from SAR image show better agreement with altimeter H_s and Scatterometer U_{10} than HOAPS U_{10}, because SAR, altimeter and Scatterometer operate in the same ERS-2 satellite, hence can obtain better collocation pairs both in time and in space than HOAPS.

A comprehensive comparison between CWAVE H_s, U_{10}, T_m and ERA 40 reanalysis results was performed for the period September 1, 1998 to November 30, 2000 for the global ocean. The comparisons of met-ocean parameter from CWAVE and ERA 40 show an overall agreement for low and medium sea state, however, an underestimation by CWAVE for high sea state.

6.1.5 Applications

Three applications of the CWAVE met-ocean parameter results are investigated. First, a satellite-based wind wave growth relation was developed for the first time from global data. The effects of water depth and wind speed were dissussed and slightly different wind wave growth relations were found. Second, a case study for the detecting of a strom missed by ERA 40 was presented. Third, the possibility of detecting Polar Lows was investigated by CWAVE retrievals for the first time. The criterion used in this thesis to detect a Polar Low is that wind speed $U_{10} \geq 15$ m/s, significant wave height $H_s \geq 5$ m/s and the latitutinal position > 60°.

6.2 Outlook

In the last decade, much effort has been put into the retrieval schemes for ocean surface parameters using SAR images. The CWAVE algorithm retrieves met-ocean parameters directly from SAR image without any a priori information for the first time, unlike other first-guess models (Hasselmann et al., 1996; Mastenbroek and de Valk, 2000; Krogstad et al., 1994). The CWAVE retrievals constitute a new assimilation source for numberic climate and wave models. This also has been underlined by Heimbach and Hasselmann (2000) that the assimilation of SAR results can be tested in operational wave forecasts.

All the validations and comparisons indicate that the CWAVE algorithm tends to underestimate at high sea state and thus needs improvement. First, the CWAVE algorithm could probably be improved by the selection of a more representive image distribution all over the world, especially including much more images from the Southern Hemisphere. Second, the new classification parameter is expected to improve the performance of CWAVE because it is more rigorous and can be more effective to remove inhomogeneous imagettes. Third, the CWAVE algorithm should perhaps be split into different algorithms for different sea state, thus better performance for high sea state can be expected.

Besides the met-ocean parameters retrieved from the homogeneous wave mode SAR imagettes, much more information for further investigation is contained in the SAR images. In the next step, four different types of imagettes: homogeneous ones, sea ice, slick and other undefined imagettes can be distinguished automatically.

The continuous acquisition of wave mode imagettes by ENVISAT and TerraSAR-X provide a good chance for long term statistical and seasonal analysis of met-ocean parameters, because 17 years of wave mode SAR image are available now since the launch of ERS-1 in 1991. The German radar satellite, TerraSAR-X, which is the first commercially available radar satellite to offer one meter horizontal resolution, went into operation on 7 January 2008. Four types of image products including StripMap, High Resolution SpotLight mode, Spotlight mode and ScanSAR mode provide new investigation opportunities like wide swath mode data, different polarization modes, and different incidence angles. Following the TerraSAR-X, a similar satellite mission called TanDEM-X is scheduled for launch in 2009. Together with the almost identical radar satellite TerraSAR-X, which was launched in June 2007, it will form a high-precision radar interferometer. Thus much more new parameters and processes such as ocean currents and more precise wave spetra could be investigated in the future.

Bibiliography

1. Alpers W., and Hasselmann K., The two-frequency microwave technique for measuring ocean-wave spectra from an airplane or satellite, Boundary-Layer Meteorology, 1978, 13, 215-230
2. Alpers W., Bruning C., and Richter K., Comparison of simulated and measured synthetic aperture radar image spectra with buoy-derived ocean wave spectra during the Shuttle Image Radar B mission, IEEE Trans. Geosci. Remote Sensing, 1986, GE-24, 559-566
3. Alpers W., Bruning C., On the relative importance of motion related contributions to the SAR imaging mechanism of ocean surface waves, IEEE Trans. Geosci. Remote Sensing, 1986, GE-24, 873-885
4. Alpers W., Monte Carlo simulations for studying the relationship between ocean wave and synthetic aperture radar image spectra, J. Geophys. Res., 1983, 88(3), 1745-1759
5. Alpers W. and B. Bruemmer, Atmospheric boundary layer rolls observed by the synthetic aperture radar aboard the ERS-1 satellite, J. Geophys. Res. 1994, 99, 12613-12621
6. Andersson, A., Bakan S., Fennig K., Grassl H., and Klepp C. The HOAPS-3 Climatology. In Proceedings of the 3rd Workshop of the International Precipitaiton Working Group (IPWG), Melbourne, 23-27 October, 2006.
7. Ardhuin F., Collard F., and Chapron B., Wave spectra from ENVISAT's synthetic aperture radar in coastal area, Proceedings of The Fourteenth (2004) International Offshore and Polar Engineering Conference, Toulon, France, 2004, 221-225
8. Askari F., and Keller W.C., Real aperture radar imaging of ocean wave during SAXON-FPN: A case of azimuth-traveling waves, J. Geophys. Res., 1994, 99(5), 9817-9833,
9. Babanin A V, Soloviev Y P. Field investigation of transformation of the wind wave

frequency spectrum with fetch and the stage of development, J. Phys. Oceanogr., 1998, 28:563

10. Banner M.L., and Fooks E.H., On the microwave reflectivity of small-scale breaking water waves, Proc. R. Soc. Lond., 1985, 399, 93-109
11. Bao M.Q., and Alpers W., On the cross spectrum between individual-look synthetic aperture radar images of ocean waves, IEEE Trans. Geosci. Remote Sensing 1998, 36(3), 922-932
12. Barner N.F., Finding the Direction of Travel of Sea Waves, Nature, 1954, 174, 1048-1050
13. Bass F.G., Fuks I.M., Kalmykov A.E., Ostrovsky I.E., and Rosenberg A.D., Very high frequency radiowave scattering by a disturbed sea surface, IEEE Trans. 1968, AP-16, 554-568
14. Beal R.C., Monaldo F.M., Tilley D.G., et. al., A comparison of SIR-B directional ocean wave spectra with aircraft scanning radar spectra, Science, 1986, 232, 1531-1535
15. Beal R.C., Spaceborne imaging radar ocean wave monitoring, Science, 1980, 208, 1373-1375
16. Beal R.C., Tilley D.G., Monaldo F.M., Large and small scale spatial evolution of digitally processed ocean wave spetctra from SEASAT synthetic aperture radar, J. Geophys. Res., 1983, 88, 1761-1778
17. Bentamy, A., Y. Quilfen, P. Queuffeulou and A. Cavanie, Calibration of the ERS-1 scatterometer C-band mode. Tech. Rep. RSMAS, 1994, 1-72
18. Bentamy, A., N. Grima, Y. Quilfen, H. V., C. Maroni, and S. Pouliquen, An Atlas of Surface Wind from ERS-1 Scatterometer Measurements, 229, IFREMER, Plouzané, 1996.
19. Breivik L.A., Reistad M., Schyberg H., Sunde J, Krogstad H.E., and Johnsen H., Assimilation of ERS-SAR wave spectra in an operational wave model, J. Geophys. Res., 1998, 103(4), 7887-7900
20. Bruning C., Alpers W., and Hasselmann K., Monte-Carlo simulation studies of the nonlinear image of a two-dimensional surface wave field by SAR, Int. J. Remote Sensing, 1990, 11(10), 1695-1727
21. Bruning C., Hasselmann S., Hasselmann K., Lehner S., Gerling T., A first evaluation of ERS-1 synthetic aperture radar wave mode data, The Glob. Atmos. And Ocean System, 1994, 2, 61-98

22. Bruning C., Schmidt R., Alpers W., Estimation of the ocean wave-radar modulation transfer function from synthetic aperture radar imagery, J. Geophys. Res., 1994, 99(5), 9803-9816
23. Bruning C.W., Alpers W., Zambresky L.F., and Tilley D.G., Validation of a synthetic aperture radar ocean wave imaging theory by the shuttle imaging radar-B experiment over the North Sea, J. Geophys. Res., 1988, 93, 15403-15425
24. Caires, S., Komen, G. and Sterl, A. Comparative assessment of ERA-40 ocean wave product. Global Change Open Science Conference (p. Poster P.4.0.098). Amsterdam, 10-13 July 2001.
25. Caudal G. and Hauser D., Directional spreading function of the dea wave spectrum at short scale, inferred from multifrequency radar observations, J. Geophys. Res., 1996, 101(7), 16601-16613
26. Cheney R., Satellite altimetry, Academic Press, 2001
27. Chubb S.R., Cooper A.L., Jansen R.M., Fusina R.A., and Lee J.S., Radar backscatter from breaking waves in gulf stream current convergence front, IEEE Trans. Geosci. Remote Sensing, 1999, 37, 1951-1965
28. Crombie D.D., Doppler spectrum of sea echo at 13.56 Mc/s, Nature, 1955, 175, 681-682
29. Cox A. T. and Swail V. R., A global wave hindcast over the period 1958-1997: validation and climate assessment. J. Geophys. Res., 2001, 106(2), 2313-2329
30. Davidan L. N., Investigation of wave probability structure on field data, Trudi, GOIN, 1980, 151, 8-26 (in Russian)
31. Davis T. Special Sensor Microwave/Imager (SSM/I). User's interpretation guide fourth edition, 1999, Raytheon Systems Company.
32. Dobson F., Perreie W. and Toulany B., On the deep-water fetch law for wind-generated surface gravity waves, Atmos.–Ocean, 1989, 27(1), 210–236
33. Donbson E, Monaldo F, Goldhirsh J, Wilkerson J., Validation of Geosat altimeter-derived wind speeds and significant wave heights using buoy data, Johns Hopkins APL Technical Digest, 1987
34. Donelan M. A., Hamilton J, Hui W H. Directional spectra of wind-generated waves, Philos.Trans.Roy.Soc.London, 1985, A315: 509
35. Donelan M. A., and Pierson W. J., Radar scattering and equilibrium ranges in wind-generated waves with application to scatterometry, J. Geophys. Res., 1987, 92, 4971-5029

36. Donelan M. A., Skafel M., Graber H., Liu P., Schwab D. and Venkatesh S., On the growth rate of wind-generated waves, Atmoshperic-Ocean, 1992, 30(3), 457-478
37. Duncan J.R., Keller W.C., and Wright J.W., Fetch and wind speed dependence of Doppler spectra, Radio Sci., 1974, 9, 809-819
38. Engen G. and Johnsen H., SAR-ocean wave inversion using image cross spectra, IEEE Trans. Geosci. Remote Sensing, 1995, 33(4), 1047-1056
39. Ericson E.A., Lyzenga D.R., and Walker D.T., Radar backscatter from stationary breaking waves, J. Geophys. Res., 104(12), 29679-29695, 1999
40. Evans K C, Kibblewhite A C. An examination of fetch-limited wave growth off the west coast of New Zealand by a comparison with the JONSWAP results, J.Phys.Oceanogr., 1990,20:1278
41. Feindt F., Schroter J., Alpers W., Measurement of the ocean wave-radar modulation transfer function at 35GHz from a sea based platform in the North Sea, J. Geophys. Res., 1986, 91(8), 9701-9708
42. Fetterer F, Gineris D, and Wackerman C C, Validation a scatterometer wind alogorithm for ERS-1 SAR, IEEE Trans. Geo. And remote sensing, 1998, 36(2), 479-493
43. Forristall G Z. On the statistical distribution of wave heights in a storm. J. Geophys. Res., 1978, 83(5), 2353-2358
44. Fouques S., Krogstad H., A numerical study of the nonlinear ocean-SAR spectrum transform, Proc. Of the IGARSS 2003 conference in Toulouse, 2003
45. Fu L.-L., D. B. Chelton and V. Zlotnicki, Satellite altimetry: observing ocean variability from space, Oceanog. Mag., 1988, 1(2), 4-11
46. Fung A.K., and Chan H., Backscattering of waves by composite rough surface, IEEE Trans., 1969, AP-17, 590-597
47. Furevik B. R. and Korsbakken E., Comparison of ERS Tandem phase scatterometer and SAR derived wind speed, IEEE, 1999, (5), 1634-1636,
48. Geernaert G. L., Bulk parameterizations for the wind stress and heat fluxes in surface in surface waves and fluxes, Vol 1, Kluwer Academic Publishers, 1990, 91-172
49. Gerling, T. W., Structure of the surface wind field from the Seasat SAR. J. Geophys. Res. 1986, 91(2): 2308-2320
50. Gilhousen, D. B., A field evaluation of NDBC moored buoy winds, J. Atmos. and Oceanic Technology, 1987, 4, 94-104
51. Giovanna D. C., R. Crapolicchio and P. lecomte, ERS-1/2 Scatterometer new

products: mission reprocessing and data quality improvement, the Second Space for Hydrology Workshop, 2007, Geneve

52. Gonzalez F.I., Beal R.C., Brown W.E., Gower J.F., Lichy D., Ross D.B., Rufenach C.L., and Shuchman R.A., SEASAT synthetic aperture radar: ocean wave detection capabilities, Science, 1979, 204, 1418-1421
53. Guan, C.L., Sun, Q., Analytically derived wind wave growth relationships, China Ocean Engineering, 2002, 16(3): 359-368
54. Hara T. and Plant W.J., Hydrodynamic modulation of short wind-wave spectra by long waves and its measurement using microwave backscatter, J. Geophys. Res., 1994, 99(5), 9767-9784
55. Hasselmann D.E., Dunckel M., and Ewing J.A., Directional wave spectra observed during JONSWAP 1973, J. Phys. Oceanogr., 1980, 10, 1264-1280
56. Hasselmann K. and Hasselmann S., On the nonlinear mapping of an ocean wave spectrum into a synthetic aperture radar image spectrum and its inversion, J. Geophys. Res., 1991, 96(6), 10713-10729
57. Hasselmann K., Raney R. K., Plant W.J., Alpers W., Shuchman R.A., Lyzenga D.R., Rufenach C.L., and Tucker M.J., Theory of synthetic aperture radar ocean imaging: a MARSEN view, J. Geophys. Res., 1985, 90(3), 4659-4686
58. Hasselmann K., Barnett T. P., Bouns E., Carlson H.,Cartwright D. E., Enke K., Ewing J. A., Gienapp H., Hasselmann D.E., Kruseman P., Meerburg A., Müller P., Olbers D.J., Richte K.r, Sell W. and Walden H., Measurements of wind-wave growth and swell decay during the Joint North Sea Wave Project (JONSWAP). Ergänzungsheft zur Dt. Hydro. Z., Reihe A, 1973, 12, 1–95.
59. Hasselmann S., Bruning C., and Lionello P., Towards a generalized optimal interpolation method for the assimilation of ERS-1 SAR retrieved wave spectra in a wave model, Proceedings of the Second ERS-1 symposium, Hamburg, Germany, Oct, 1993, ESA Spec. Publ., ESA SP-361, 21-25,1994
60. Hasselmann S., Bruning C., Hasselmann K. and Heimbach P., An improved algorithm for the retrieval of ocean wave spectra from synthetic aperture radar image spectra, J. Geophys. Res., 1996, 101(7), 16615-16629
61. He Y.J., Ocean wave imaging mechanism by imaging radar, Science in China (series D), 2000, 43(6), 587-595
62. Heimbach P., Hasselmann S., Hasselmann K., Statistical analysis and intercomparison with WAM model data of three years of global ERS-1 SAR wave

mode spectral retrievals over 3 years, J. Geophys. Res., 1998, 103, 79311-7977

63. Henderson, F.M., and A.J. Lewis, Principles and applications of imaging radar, Manual of remote sensing, edited by R.A. Ryerson, pp. 868, John Wiley and Sons, Inc., New York, Chicester, Weinheim, Brisbane, Singapore, Toronto,1998
64. Hollinger, J. P., Peirce, J. L. and Poe, G. A. SSM/I instrument evaluation. IEEE Trans. Geosci. Remote Sens., 1990, 28(5), 781-790.
65. Holt B., Liu A.K., Wang D.W., Gnanadesikan A., and Chen H.S., Tracking storm-generated waves in the northeast Pacific Ocean with ERS-1 synthetic aperture radar imagery and buoy, J. Geophys. Res., 1998, 103(4), 7917-7929
66. Horstmann J., Koch W., Lehner S. et al. Wind retrieval over the ocean using synthetic aperture radar with C-band HH polarization. IEEE Trans. Geosci. Remote Sensing, 2000, 38(9), 2122-2131
67. Horstmann J., Koch W., Lehner S. et al. Ocean winds from RADARSAT-1 scanSAR. Can. J. Remote Sens., 2002, 28(3), 524-533
68. Horstmann, J., Schiller, H., Schulz-Stellenfleth, J. and Lehner, S., Global wind speed retrieval from SAR, IEEE Trans. Geosci. Remote Sens. 2003, 41, 2277-2286
69. Jao J.K., Theory of synthetic aperture radar imaging of a moving target, IEEE Trans. Geosci. Remote Sensing, 2001, 39(9), 1984-1992
70. Jessup A.T., Melville W.K., and Keller W.C., Breaking waves affecting microwave backscatter 1. Detection and Verification. J. Geophys. Res., 1991, 96, 20547-20559
71. Jocobsen S., and Hogda K.A., Estimation of the real aperture radar modulation transfer function directly from synthetic aperture radar ocean wave image spectra without a priori knowledge of the ocean wave height spectrum, J. Geophys. Res., 1994, 99(5), 14291-14302
72. Johannessen, J. A., P. W. Vachon and O. M. Johannessen, ERS-1 SAR imaging of marine boundary layer processes. ESA EOQ 46, Eur. Space Agency, 1994, 1-256, Paris, France
73. Kahma K. K., A study fo the growth of the wave spectrum with fetch, J. Phys. Oceanogr., 1981, 11, 1503-1515
74. Kara A. B., Rochford A. P., and Hurlburt E. H., Efficient and accurate bulk parameterizations of air-sea fluxes for use in general circulation models, Journal of Atmospheric and Oceanic Technology, 2000, 17, 1421-1438
75. Kasischke E.S., Chuchman D.R., Lyzenga D.R., Meadows G.A., Detection of bottom features on SEASAT synthetic aperture radar imagery, Photogram. Eng. Remote

Sens., 1983, 49, 1341-1353

76. Kazuo Ochi, Shoji Maedoi and Hisashi Mitsuyasu, Determination of ocean wave propagation direction by split-look processing using JERS-1 SAR data, IEEE Trans. Geosci. Remote Sensing, 1999, 37(2), 849-855
77. Keller W.C., and Wright J.W., Microwave scattering and the straining of wind-generated waves, Radio Sci., 1975, 10, 139-147
78. Kent, E.C., Taylor, P.K. and Challenor, P.G., A comparison of ship- and scatterometer-derived wind speed data in open ocean and coastal areas. International Journal of Remote Sensing, 1998, 19, (17), 3361-3381.
79. Kerbaol V., Chapron B., and Vachon P.M., A global analysis of ERS-1/2 SAR wave mode imagettes, J. Geophys. Res., 1998, 103, 7833-7846
80. Kinsman, B., Wind waves. Prentice-Hall, Englewood Cliffs. 1965, 1-676.
81. Komen, G.J., L. Cavaleri, M. Donelan, K. Hasselmann, S. Hasselmann, and P.A.E.M. Janssen, Dynamics and Modelling of Ocean Waves, 554, Cambridge University Press, Cambridge, 1996.
82. Krogstad H.E., A simple derivation of Hasselmann's nonlinear ocean –synthetic aperture radar transform, J. Geophys. Res., 1992, 97(2), 2421-2425
83. Krogstad H.E., and Barstow S.F., Directional Distributions in ocean wave spectra, Proceedings of the Ninth(1999) International Offshore and Polar Engineering conference, 79-86
84. Krogstad H.E., Barstow S.F., Satellite wave measurement for coastal engineering applications, Coastal Engineering, 1999, 37, 283-307
85. Krogstad H.E., Samset O. and Vachon P.M., Generalizations of the non-linear ocean-SAR transform and a simplified SAR inversion algorithm, Atmosphere-Ocean, 1994, 32(1), 62-82
86. Krasnopolsky V M, Gemmill W H and Breaker L C, A neural network multiparameter algorithm for SSM/I ocean retrievals: Comparisons and validations. Remote Sensing Environment, 73(2), 133-142, 2000
87. Kudriatsev V., Hauser D., Caudal G., Chapron B., A semiempirical model of the normalized radar cross-section of the sea surface, part 1: background model, J. Geophys. Res., 2003, Vol.108, No. C3, 8054, doi:10.1029/2001JC001003
88. Kudriatsev V., Hauser D., Caudal G., Chapron B., A semiempirical model of the normalized radar cross-section of the sea surface, part 2: radar modulation transfer function, J. Geophys. Res., 2003, 108(3), 8055, doi:10.1029/2001JC001004

89. Kuo Y.Y., Leu L.G. and Kao I.L., Directional spectrum analysis and statistics obtained from ERS-1 SAR wave images, Ocean Engineering, 1999, 26, 1125-1144
90. Laur H., Bally P., Meadows P., Sanches J., Schattler B., and Lopinto E., ERS SAR calibration: Derivation of the backscattering coefficient σ_0 in ESA ERS SAR PRI products, ESA doc. ES-TN-RS-PM-HL09, Eur. Space Res. And Technol. Cent., 2002
91. Lee P.H., and Coauthors, X band microwave backscatter from ocean wave, J. Geophys. Res., 1995,100, 2591-2611
92. Lecomte P., The ERS scatterometer instrument a nd the on-ground processing of its data, wind product specifications**,** 1998
93. Lehner S., Horstmann J., Koch W. et al. Mesoscale wind measurements using recalibrated ERS SAR images. J. Geophys. Res., 1991, 103(4), 7847-7856.
94. Lehner S., J. Schulz-Stellenfleth, B. Schättler, H. Breit and J. Horstmann, Wind and Wave Measurements Using Complex ERS-2 SAR Wave Mode Data, IEEE Transactions on Geoscience and Remote Sensing, 2000, 38(5), 2246-2257.
95. Li X.F., Pichel W.G., He M.X., Wu S.Y., friedman K.S., Clenmente-Colon P. and zhao C.F., Observation of hurricane generated ocean swell refraction at Gulf Stream North Wall with the RADARSAT-1 synthetic aperture radar, IEEE Trans. Geosci. Remote Sensing, 2002, 40(10), 2131-2142
96. Longuet-Higgins M S. On the joint distribution of the period and amplitudes of sea waves. J. Geophys. Res., 1975, 80, 2688-2694
97. Longuet-Higgins M S. The effect of nonlinearities on statistical distributions in the theory of sea waves. J. Fluid Mech., 1963, 17, 459-480
98. Longuet-Higgins M S. The statistical analysis of a random moving surface. Phil. Trans. Roy. Soc., 1957, 249, 321-387
99. Longuet-Higgins M.S., Fox J.H., Theory of the almost-highest wave: the inner solution, J. Fluid Mech., 1977, 80, 721-741
100. Lyzenga D.R., and Shuchman R.A., Analysis of scatterer motion effects in Marsen X band SAR imagery, J. Geophys. Res., 88(14), 9769-9775, 1983
101. Lyzenga D.R., Numerical simulation of synthetic aperture radar image spectra for ocean waves, IEEE Trans. Geosci. Remote Sensing, 1986, GE-24, 6, 863-872
102. Mastenbroek C. and C.F. de Valk, A semiparametric algorithm to retrieve ocean wave spectra from synthetic aperture radar, J. Geophys. Res., 2000, 105, 3497-3516
103. McLeish W., Ross D., Shuchman R.A., Teleki P.G., Hsiao S.V., Shemdin O.H., and

Brown W.E., Synthetic aperture radar imaging of ocean waves: comparison with wave measurements, J. Geophys. Res., 1980, 58, 5003-5011

104. Melsheimer C., Bao M. and Alpers W., Imaging of ocean wave on both sides of an atmospheric front by the SIRC/X-SAR multifrequency SAR, J. Geophys. Res., 1998, 103, 18839-18849
105. Mitsuyasu H. et al., Observations of the Directional Spectrum of Ocean Wave using a Cloverleaf Buoy, J. Phys. Oceanogr. 1975, 5(4), 750-760
106. Mitsuyasu H., Tasai F., Suhara T., Mozuno S., Ohkusu M., Honda T., and Rikiishi K., Observation of the power spectrum of the ocean waves using cloverleaf buoy, J. Phys. Oceanogr., 1979, 10, 286-296
107. Mitzner K.M., Effect of small irregularities on electromagnetic scattering from an interface of arbitrary shape, J. Math. Phys., 1964, 5, 1776-1786
108. Monaldo F.M., and Beal R.C., Comparison of SIR-C SAR wavenumber spectra with WAM model predictions, J. Geophys. Res., 1998, 103, (9), 18815-18825
109. Monaldo F.M., and Lyzenga D.R., Comparison of SIR-B ocean wave spectra with linear model predictions based on aircraft measurements, J. Geophys. Res., 1988, 92, 15374-15388
110. Monaldo F.M., Gerling T.G. and Tilley D.G., Comparison of SIR-B SAR wave image spectra with wave model predictions : implications on the SAR modulation transfer function, IEEE Trans. Geosci. Remote Sensing, 1993, 31, 6, 1199-1209
111. Monaldo F., Thompson D., Beal R. et al. Comparison of SAR-derived wind speed with model predictions and ocean buoy measurements. IEEE Trans. Geosci. Remote Sensing, 2002, 40(12), 2587-2600
112. Neumann G., On ocean wave spectra and new way of forecasting wind generated sea, U.S. Army Corps Eng. Tech. Mem., 1958, 43, 1-42.
113. Nghiem S. V., Yueh S.H., Kwok R. et al. Symmetry properties in polarimetric remote sensing. Radio Sci., 1992, 27(5), 693-711
114. Ouchi K., Synthetic aperture radar imagery of range traveling ocean waves, IEEE Trans. Geosci. Remote Sensing, 1988, GE-26, 30-37
115. Pawka S.S., Hsiao V., Shemdin O.H., and Inman D.L., Comparison between wave directional spectra from SAR and pressure sensor arrays, J. Geophys. Res., 1980, 85, 4987-4995
116. Peixoto, J.P., and A.H. Oort, Physics of Climate, American Institute of Physics, Woodbury, NY, 1992.

117. Phillips O.M., Radar returns from the sea surface—Bragg scattering and breaking waves, J. Phys. Oceanogr., 1988, 18, 1063-1074
118. Phillips O.M., Spectral and statistical properties of the equilibrium range in wind-generated gravity waves, J. Fluid Mech., 1985, 156, 505-531
119. Pierson W.J., Comment on "Effect of sea maturity on satellite altimeter measurement" by Roman E.Glazman.and Stuart H. Pilorz, J. Geophys. Res., 1991, 96(3), 4973-4977
120. Plant W.J. and Keller W.C., Parametric dependence of ocean wave-radar modulation transfer functions, J. Geophys. Res., 1983, 88(14), 9747-9756
121. Plant W.J. and Keller W.C., The two-scale radar wave probe and SAR imagery of the ocean, J. Geophys. Res., 1983, 88(14), 9776-9784
122. Plant W.J. and Zurk L.M., Dominant wave directions and significant wave heights from synthetic aperture radar, J. Geophys. Res., 1997, 102(2), 3473-3482
123. Plant W.J., A two-scale model of short wind-generated waves and scatterometry, J. Geophys. Res., 1986, 91(9), 10735-10749
124. Plant W.J., and Alpers W., An introduction to SAXON-FPN, J. Geophys. Res., 1994, VOL.99, 9699-9703
125. Plant W.J., Keller W.C., Hesany V., Hara T., Bock E., and Donelan M., Bound waves and Bragg scattering in a wind-wave tank, J. Geophys. Res., 1999, 104, 3243-3263
126. Podgorski K., Rychlik I., Ryden J., and Sjo E., How big are the big waves, Proceedings of the Ninth(1999) International Offshore and Polar Engineering conference, 53-60
127. Quilfen, Y. and A. Bentamy, Calibration/validation of ERS-1 scatterometer precision products. Proceedings of IGARSS'94. IEEE press, Piscataway, USA, 1994, 945-947
128. Quilfen Y., ERS-1 off-line wind scatterometer products (Brest: IFREMER/CERSAT), 1995
129. Quilfen Y., Chapron B., Elfouhaily T. et al. Observation of tropical cyclones by high-resolution scatterometry. J. Geophys. Res., 1998, 103(4), 7767-7786
130. Rayleigh L., On periodic irrotational waves at the surface of deep water. Phil. Mag., 1917, 33, 381-389
131. Robinson, I.S., Measuring the oceans from space: the principles and methods of satellite oceanography, Berlin, Germany, Springer/Praxis Publishing, 2004, pp.669
132. Romeiser R., Schmidt A., and Alpers A., A three scale composite surface model for

the ocean wave-radar modulation transfer function, J. Geophys. Res., 1994, 99(5), 9785-9801

133. Romerser R. and Alpers W., An improved composite surface model for the radar backscattering cross section of the ocean surface: Model response to surface roughness variations and the radar imagery of underwater bottom topography, J. Geophys. Res., 1997, 102, 25251-25267
134. Rousseau S. and Forget P., Ocean wave mapping from ERS SAR images in the presence of swell and wind waves, Scientia Marina, 68(1), 1-5
135. Rufenach C.L., and Alpers W.R., Imaging ocean waves by synthetic aperture radars with long integration times, IEEE Trans. Geosci. Remote Sensing, 1981, AP-29, 3, 422-428
136. Schmidt A., Wismann V., Romeiser R. and Alpers, Simultaneous measurements of the ocean wave-radar modulation transfer function at L, C, and X bands from the research platform Nordsee, J. Geophys. Res., 1995, 100, 8815-8827
137. Schroter J., Feindt F., Alpers W. and Keller W.C., Measurement of the ocean wave-radar modulation transfer function at 4.3 GHz, J. Geophys. Res., 1986, 91(1), 923-932
138. Schulz-Stellenfleth J. and Lehner S., Spaceborne synthetic aperture radar observations of ocean waves traveling in sea ice, J. Geophys. Res., 107(8), 10.1029/2001, 20-1—20-19, 2002
139. Schulz-Stellenfleth J. and Lehner S., Measurement of 2-d sea surface elevation fields using complex synthetic aperture radar data, IEEE Trans. Geosci. Remote Sens., 2004, 42, 1149-1160
140. Schulz-Stellenfleth, J., Koenig, T. and Lehner, S., An empirical approach for the retrieval of integral ocean wave parameters from synthetic aperture radar data. J. Geophys. Res. 2007, 112, 3019-3033
141. Scoon A., Robinson I. S. and Meadows P. Demonstration of an improved calibration scheme for ERS-1 SAR imagery using a scatterometer wind model. Int. J. Remote. Sens., 1995, 17(2):413-418
142. Song G.., S. Lehner, J. Schulz-Stellenfleth , H. Grassl, Statistical analysis of ocean wave and wind parameters retrieved with an empirical SAR algorithm, ENVISAT Symposium, April, 2007, Switzerland.
143. Stoffelen, A., and Anderson, D. L. T., 1992, ERS-1 scatterometer calibration and validation activities at ECMWF: A. the quality and characteristics of the radar

backscatter measurements. ERS-1 Geophysical Validation Workshop Proceedings, 27-30, April 1992, Penhors, France (Paris: ESA), 83-88

144. Stoffelen, A., and D. Anderson, Scatterometer Data Interpretation: Estimation and Validation of the Transfer Function CMOD4, Journal of Geophysical Research, 1997, 102 (5), 5767-5780
145. Tayfun M A. Narrow-band nonlinear sea waves. J. Geophys. Res., 1980, 85, 1548-1552
146. Taylor P. K., Validation of ERS-1 wind data using observations from research and voluntary observing ships. Proceedings of a Workshop on ERS-1 Wind and Wave Calivration, September 1986, Schlirsee, Germany, ESA, SP-262, 69-75
147. Taylor P. K., Kent E. C., Yelland M. J. and Moat B. I., The accuracy of wind observations from ships, Proceedings of International COADS Wind Workshop, Kiel Germany, 31 May-2 June 1994, 132-155
148. Tilley D.G., and Beal R.C., ERS-1 and Almaz estimates of directional wave spectra conditioned by simultaneous aircraft SAR and buoy measurements, Atmos. Ocean, 1994, 32(1), 113-142
149. Toba, Y., Local balance of in the air-sea boundary processes, Ⅲ. On the spectrum of wind waves, J.Oceanogr.Soc.Japan, 1973, 29, 209
150. Toba, Y., Local balance of in the air-sea boundary processes. Ⅰ,On the growth process of wind waves, J.Oceanogr.Soc.Japan, 1972, 28(3), 109-121
151. Tsai W.-Y., Nghiem S.V., Huddleston J. N. Polarimetric scatterometry: A promising technique for improving ocean surface wind measurements from space. IEEE Trans. Geophys. Remote Sensing, 2000, 38(4), 1903-1921.
152. Vachon P.W., Krogstad H.E., and Paterson J.S., Airborne and spaceborne synthetic aperture radar observations of ocean waves, Atmosphere-Ocean, 1994, 32(1), 83-102
153. Vachon P. W. and Dobson F. Validation of wind vector retrieval from ERS-1 SAR images over the ocean. Global Atmos. Ocean Syst., 1996, 5, 177-187
154. Valenzuela G.R., Laing M.B., and Daley J.C., Ocean spectra for the high-frequency waves as determined from airborne radar measurement, Journal of Marine Research, 1971, 29(2), 69-84
155. Valenzuela G.R., Scattering of electromagnetic waves from a tilted slightly rough surface, Radio Sci., 1968, 3, 1057-1066
156. Valenzuela G.R., Theories for the interaction of electromagnetic and oceanic

waves--a review, Boundary—Layer Meteorology, 1978, 13, 61-85

157. Valwnzuela, G. R., Theories for interaction of electromagnetic and oceanic waves: A review Boundary Layer Meteorol. 1978, 13, 61-85
158. Vesecky J.F., and Steward R.H., The observation of ocean surface phenomena using imagery from the SEASAT synthetic aperture radar: an assessment, J. Geophys. Res., 87(5), 3397-3430
159. Voilante-Carvalho N. and Robinson I. S., Comparison of the two-dimensional directional wave spectra retrieved from spaceborne synthetic aperture radar images using the MPI scheme against directional buoy measurements, Scientia Marina, 2004，68(3), 317-330
160. Voorrips A.C., Mastenbroek C., Hansen B., Validation of two algorithms to retrieve ocean wave spectra from ERS synthetic aperture radar, J. Geophys. Res., 2001, 106, (8), 16825-16840
161. Wadhams P., Parmiggiani F., Carolis G. de., The use of SAR to measure ocean wave dispersion in Frazil-Pancake icefield, Journal of Physical Oceanography, 2002, 32, 1721-1746
162. Wang, B. X., An investigation on the $\alpha-\beta$ relationship of ocean waves. J. Ocean Univ. Qingdao. 1990, 20(3), 1-9. (in Chinese)
163. Wen, S. C., Ocean Wave Theory. Shandong People's Press, Jinan, China, 1962, 224-265.
164. Wen, S. C. and Z. W. Yu, Ocean Wave Theory and Computation Principle, Science Press, Beijing, 1984. (in Chinese)
165. Wen, S.C., Zhang, D.C., Guo, P.F. et al., Parameters in wind-wave frequency spectra and their bearing on spectrum forms and growth, Acta Oceanol.Sinica, 1989, 8(1), 15
166. Wentz F. J., Peteherych S. and Thomas L. A. A model function for ocean radar cross sections at 14.6 GHz. J. Geophys. Res., 1984, 89(3), 3689-3704
167. Wentz F. J. and Smith D. K. A model function for the ocean normalized cross section at 14 GHz derived from NSCAT observations. J. Geophys. Res., 1999, 104(5), 11499-11507
168. Winterfeldt J. and Weisse R., Comparison of measured and simulated wind speed data in the North Atlantic, Geophysical Research Abstracts, 2008, 10, EGU2008-A-09566

169. Wright J.M., A new model for sea clutter, IEEE Trans., 1968, AP-16, 217-223,

170. Wright J.W., Backscattering from capillary waves with application to sea clutter, IEEE Trans. Antennas Propagat. 1966, AP-14, 749-754

171. Wright J.W., Detection of ocean waves by microwave radar; The modulation of short gravity-capillary waves, Boundary-Layer Meteorology, 1978, 13, 87-105

172. Wright J.W., Plant W.J., Keller W.c., and Jones W.L., Ocean wave-radar modulation transfer function from the West Coast Experiment, J. Geophys. Res., 1980, 85(9), 4957-4966

173. Wu, S. P., Y. J. Hou, B. S. Yin, J. B. Song and X. X. Zhao, Relationship between wave steepness and wave. age in the course of wind wave growth, Chinese Journal of Oceanology and Limnology, 2004, 22(1), 1-4

174. Yang J. S., Huang W. G., Zhou C. B. et al. Coastal ocean surface wind retrieval from SAR imagery. J. Remote Sensing (in Chinese), 2001, 5(1), 13-16

175. Young I. R., The growth rate of finite depth wind-generated waves, Coastal Engineering, 1997, 32, 181-195

176. Yueh S. H., Kwok R. and Nghiem S. V. Polarimetric scattering and emission properties of targets with reflection symmetry. Radio Sci., 1994, 29(6), 1409-1420

177. Zurk L.M., and Plant W.J., Comparison of actual and simulated SAR imagery of ocean waves using SAXON-FPN measurements, J. Geophys. Res., 1996, 101, 8913-8931

Acknowledgement

I would like to thank all those who gave me the possibility to complete this thesis:

- My supervisor Prof. Dr. Hartmut Graßl and Co-Advisor Dr. Stephan Bakan. Their encouragement made me confident to continue my thesis work; their suggestions and ideas inspired and motivated me to obtain a better scientific result. ’One day’s teacher, the whole life’s father’, this Chinese proverb teaches me that special gratitude and respect to them should be kept in my mind for my whole life.
- Dr. Susanne Lehner, Dr. Johannes Schulz-Stellenfleth, and Thomas König for the provision of the ERS-2 SAR and Altimeter data, access to all computer codes and all the help and discussions. Their valuable suggestions and ideas and the close guidance helped me to limit my pool of ideas to what is possible within the time frame agreed upon and necessary for a sound thesis layout.
- Christine Fluche for all her service which reduced communication inconvenience for a foreign Ph.D student.
- S. Brusch, A. Reppucci, X. Li and the whole Marine Remote Sensing group in German Aerospace Centre (DLR) for all the help and discussions.
- A. Andersson, A. Blechschmidt, C. Klepp and K. Fennig from the HOAPS team for their help with obtaining and using HOAPS data.
- ECMWF for provision of ERA 40 reanalyses data.
- Gert König-Langlo from AWI for the important comments on Polarstern data.
- NOAA for supplying the buoy data.
- The Centre for Satellite Exploitation and Research (CERSAT) of the French Institute of Research for the Exploitation of the Sea (IFREMER) for the delivery of the Scatterometer wind vector data.
- The Physical Oceanography Distributed Active Archive Center at the NASA Jet Propulsion Laboratory for the free provision of QuikSCAT’s sea Winds data.

- The China Remote Sensing Satellite Ground Station (RSSG) for the provision of the ENVISAR ASAR data.
- The National Marine Environmental Foreasting Center for supplying the Chinese coastal buoy wind vector data.
- Hui Wan and Wei Shen for their assistance.
- Anyone I forgot.

Especially, I would like to give my special thanks to my wife Yanhui whose patient love enabled me to complete this work. Your love, support and constant patience and encouragement have taught me so much about sacrifice, discipline and compromise.